Development of a reinforcing fibre light-guide for use as a damage sensor within composite structures

A thesis submitted for the degree of Doctor of Philosophy

by

Simon Antony Hayes

Department of Materials Engineering, Brunel University

June 1998

Acknowledgements

Firstly I would like to thank my supervisors, Dr G. Fernando and Prof B. Ralph, for their invaluable help and support in the preparation of this thesis. I also gratefully acknowledge the financial support that I recieved from Mr D. Coward at Royal Mail Securities and also from the EPSRC.

My thanks are also extended to all of the technical staff in the Materials Engineering Department and in ETC for their help.

Many thanks are also due to all of my fellow research students, too numerous to name individually, for their support and friendship.

Lastly I must thank my wife and sons, Michelle, Antony and Aaron, for their love, encouragement and patience during my studies.

Abstract

This study presents the results of an investigation to develop a novel sensor which would give a direct indication of the extent of impact damage in a composite. This was achieved by using glass reinforcing fibres to produce a light-guide, which was embedded within a composite laminate. The laminate was then subjected to impact events or bending stresses of sufficient magnitude to cause damage. The impact energies used in this study varied between 2 and 10 Joules, and the indentation depths varied between 0.125 and 1 mm, allowing damage propagation to be monitored. The fall-off in the transmitted light was used to monitor the level of damage, along with C-scanning and sectioning to provide reference data. The use of reinforcing fibres to produce the sensor meant that the strains required to cause failure in the fibres was realistically close to those of the composite constituents. Changes in the transmission characteristics of the sensor were found to correspond to real failure events occurring during impact.

Contents

Figures

Tables

Chapter 1. Introduction

1.1. Rationale

Fibre reinforced composite materials offer a number of advantages over conventional engineering materials. This is due to their exceptional specific properties, enabling the production of strong and light components leading to their extensive use in aerospace, automotive and high technology sporting goods. However, such composites can easily be damaged, particularly by impacts, even at low energies. This damage can be impossible to visually detect.

Due to the susceptibility of fibre reinforced composites to this so called barely visible impact damage (BVID), examination techniques for inspecting composite parts have been developed. These can be comparatively well known techniques such as ultrasonic C-scanning and X-ray radiography. The damage can also be imaged using less common techniques such as surface interferometric techniques and thermography. All of these methods are generally laboratory based techniques, which require the component to be removed from the structure before examination can be carried out. Therefore, techniques which allow the component to be examined in-situ have also been sought.

Damage detection in-situ has been approached from a number of directions. Embedded or surface mounted

piezo-electric sensors have been used to monitor the strain-waves associated with impact damage. This enables the damage location to be found by triangulation between multiple sensors. Another approach has been to include optical fibre sensors within the structure of the composite. These sensors can be of a number of different types, with varying degrees of sophistication. Looking at the extremes of sophistication, some sensors can monitor the precise strain in the composite, allowing the detection and quantification of impact events. These use various interferometric systems, the most common being the Fabry-Perot interferometer. Alternatively, they can be simple crack interceptors which act merely as an on/off switch when a crack propagates through the optical fibre.

The inclusion of an optical fibre, typically having a diameter of 125 μm, in a material reinforced with fibres having a typical fibre diameter of 10 μm, requires some careful consideration. The inclusion of the optical fibre distorts the expected reinforcing fibre arrangement, introducing distortions in the structure of the composite. The amount of distortion depends on the angle between the direction of the optical fibre and the direction of the reinforcing fibres. If the reinforcing fibres lie perpendicular to the optical fibre, the distortion is high, whereas if they lie parallel, the distortion is low. This distortion leads to the development of a resin rich region, the size of which varies with angular mismatch in the fibres. A number of authors have carried out studies on the effect of

embedded optical fibres on composites, with most saying there is little negative effect. Others, however, report degradation particularly in compressive properties.

In order to overcome the problems associated with the inclusion of an optical fibre into a composite component, an alternative form of optical sensor was sought. The use of reinforcing fibres to produce an optical sensor would allow the properties of the sensor to more closely mirror that of the composite. The failure of the reinforcing fibres would also be closely related to those of the reinforcing fibres within the composite. It was, therefore, expected that such a sensor would allow the failure of the composite to be directly monitored, with changes in sensor performance being closely related to specific failure events in the composite. Thus it was proposed that the possibility of utilising glass reinforcing fibres as an optical damage sensor should be investigated.

1.2. Aims of this Study

The aim of this study is to examine the possibility of using glass reinforcing fibres as an optical damage detection system, for use within composite structures. All aspects pertinent to the use of reinforcing fibres to produce an optical light-guide will be examined in the first instance. Subsequent to the production of an operational light-guide, the suitability of this for use as an optical damage detection sensor will be

investigated. The effect of this damage detection sensor on the impact damage performance of the composite will also be examined. Having developed a damage detection sensor utilising glass reinforcing fibres as the sensing element, any problems associated with the use of this sensor will be addressed.

1.3. Structure of this Thesis

In order to address the project discussed above, this thesis will be structured in the following manner:

i) Introduction

ii) Literature survey
The specific areas discussed will include the statistical failure processes of reinforcing fibres and also aspects relevant to fragmentation of reinforcing fibres when embedded. Damage development under impact and damage detection within composites will also be thoroughly investigated.

iii) Examination of the raw materials
This chapter will discuss the experimental examination of the raw materials considered for use in this study. Suitable materials will be selected and considered for further utilisation.

iv) Production of a reinforcing fibre light-guide

This chapter will discuss the the methods used to produce the reinforcing fibre light-guide (RFLG) from the selected raw materials.

v) Loss mechanisms associated with the reinforcing fibre light-guide

This chapter will include a discussion of loss mechanisms commonly associated with optical fibres and their particular application to the unique geometry of the reinforcing fibre light-guide. Some experimental investigations into the operative loss mechanisms will also be presented.

vi) Examination of damage development in composite containing reinforcing fibre light-guides

This chapter will present detailed examination of the damage observed within panels containing RFLG's and also reference panels, allowing the effect of the embedded RFLG to be established.

vii) Examination of the performance of the reinforcing fibre light-guide as a damage sensor

This chapter will include a discussion of the sensing mechanisms of the fibre and also modelling of the sensor performance. Experimental results which show the performance of the sensor under impact will be presented.

vii) Conclusions and further work

Chapter 2. Literature Review

Readers who are unfamiliar with the operation of optical fibres or composite materials are refered to some of the many books dealing with them. Recommended reading in the field of optical fibres and sensors include Moller (1988), Ghatak and Thygajan (1989), Yariv (1991) and Udd (1991). Recommended reading in the field of composite materials include Tsai and Hahn (1980), Hull (1981) and Harris (1986).

2.1. Factors pertinent to sensor performance

Due to the nature of glass or carbon fibre composite materials, when a load is applied, fibres within the composite will break as they attain their failure strain. The load at which the fibres fail depends on the fibre strength distribution and the level of adhesion between the fibres and the matrix. The determination of fibre strength will be the subject of section 2.1.2, while section 2.1.1 will focus on the determination of the adhesive strength of the fibre/matrix bond.

2.1.1. Fibre/matrix adhesion testing

This section will examine three methods of adhesion testing in composites, fibre fragmentation, fibre pull-out and micro-indentation. Following a brief description of each method, their advantages and disadvantages will be presented.

In the fibre fragmentation test, a single fibre is mounted axially in a resin coupon. The coupon is then strained, causing stress to be transferred from the matrix into the fibre. In this way, a tensile stress is observed in the fibre (Herrera-Franco and Drzal (1992), Aslown et al. (1989)). The strength of the interface between the reinforcing fibre and matrix resin alters the rate at which the stress builds up to the maximum value. The fibre will break as the tensile stress in the fibre increases to its break strength. Once a break occurs, the stress redistributes, building up from the broken fibre ends. The fibre will continue to break and the stresses will redistribute each time a fracture occurs. The nature of the build up has been described mathematically by a number of researchers, notably Cox (1952) and Kelly and Tyson (1965) who proposed the most commonly used models.

Kelly and Tyson (1965) proposed that the build-up of tensile stress in the fibre could be approximated to a linear build-up to a plateau at the fibre break stress. This meant that the fibre would continue to break until all of the fragments had a single critical length. This length would be dependent on the rate of stress build-up within the fibre and, thus, the strength of the adhesive bond (see figure 2.1). They stated the formula for the build-up as

$$\tau = \sigma_f/2 * (d/l_c) \qquad 2.1$$

where τ is the interfacial shear stress at failure, σ_f is the measured failure stress, d is the diameter of the fibre

and l_c is the critical length below which no further fibre fracture can occur.

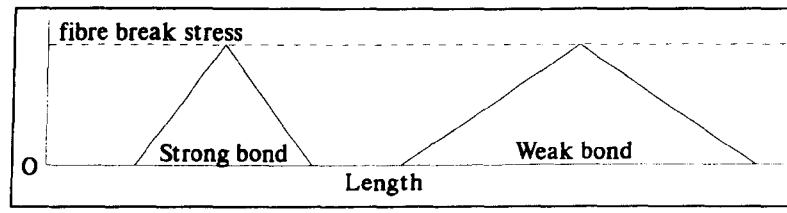

Figure 2.1. Illustrating the difference in fragment lengths developing when a weak and strong interface are compared.

The above model assumes that a single failure stress exists for the fibre. In the case of polymeric and ceramic reinforcing fibres, this assumption is not valid, due to the inherent flaw distribution. Thus, a length distribution varying between $l_c/2$ and a value somewhat greater than l_c will be obtained, as there are in fact different values of σ_f for each break location. The assumption of a single average value of the failure stress makes the calculation possible; however, the assumption is not strictly correct in the case of polymeric or ceramic reinforcing fibres. The model was originally proposed for tungsten fibres in a metal matrix, for which the single stress assumption would be nearly correct.

In order to compensate for this invalid assumption, modifying constants have been proposed. The most commonly used of these (Netravali et al. (1989)) states that

$$\tfrac{4}{3} l_a = l_c \qquad 2.2$$

where l_a is the average fragment length.

Fibre pull-out testing (Herrera-Franco and Drzal (1992)) is carried out using a resin block from which a fibre protrudes. The embedded length of the fibre within the block is kept short so that the fibre will pull out of the block without fracturing. The level of adhesion can then be calculated from the embedded surface area of the fibre and the load required to pull the fibre out.

The micro-indentation test (Herrera-Franco and Drzal (1992)) involves preparation of a thin section of a real composite. A blunt indenter is then positioned above one fibre and load is applied until the adhesion between fibre and matrix fails and the fibre is pushed out of the composite. The level of adhesion can then be calculated in the same way as for fibre pull-out testing.

The advantages and disadvantages of each approach are shown in table 2.1.

Technique	Advantages	Disadvantages
Fibre fragmentation	One sample gives lots of data points. Simple preparation of samples Easy observation of failures	Flexible resin required. Average fibre strength must be measured. Debonding not considered.
Fibre pull-out	Real resin systems used. Fibre failure strength need not be known.	Only one data point obtained per sample. Difficult to interpret data properly.
Micro-indentation	Real composite specimens can be analysed.	Preparation may degrade the adhesion properties. Complex measurement systems required.

Table 2.1. Comparison of the advantages and disadvantages of fibre/matrix adhesion test methods.

Due to the relatively complex geometries of the micro-indentation and fibre pull-out tests, fibre fragmentation testing was chosen for this study.

2.1.2. Statistical strength of reinforcing fibres

2.1.2.1. Theoretical considerations

As stated previously, non-metallic composite reinforcing fibres generally do not have a single failure strength. This strength distribution is caused by flaws of varying severity within the reinforcing fibres (Weibull (1951), Wagner et al. (1984), Hagege and Bunsell (1988), Baxevanakis et al. (1993)). Flaws can be due to various reasons, such as the inclusion of microscopic particles during the production stage, minuscule cracks in the fibre surface or cracks and crystallographic defects within the fibre itself. Flaws can also be introduced by external influences such as mishandling and environmental conditions. The flaws are unlikely to be systematically introduced and will therefore be random in size and position. As the flaw distribution is unlikely to be uniform, different pieces of fibre will have different strengths. Also, the longer the piece of fibre, the more chance there is that a large flaw will be present within that length. In this way, a length effect is observed, with the fibre strength increasing as the fibre length decreases. This length effect is easily observed in practice, by carrying out tensile tests on various lengths of fibre.

To describe this strength distribution, a commonly used formula is the Weibull distribution (Weibull (1951)), shown in equation 2.3.

$$f(x) = 1 - e^{-\frac{(x - x_u)^m}{x_o}} \qquad 2.3$$

where χ is the parameter of interest, χ_u is the lower limit of χ, m is termed the Weibull shape parameter and χ_o is termed the Weibull scale parameter. This was developed as a generally applicable theory that could be used in many circumstances in which random effects were involved. Weibull (1951) applied this equation to the fatigue life of steel, the yield strength of steel, the break strength of cotton fibres and the size of adult men born in the British Isles, among other things. To analyse the data, $ln(ln(1/(1-f(\chi))))$ is plotted against $ln(\chi)$. If the Weibull function applies, the data forms a straight line with a gradient of m and an intercept at Y=0 of $\chi=\chi_o$.

Some of the examples used by Weibull (1951) follow the basic form of equation 2.3. These give a single straight line when the Weibull distribution curve is plotted. Others take the form of a two parameter distribution, with two straight line sections of different gradients. Weibull (1951) proposed that this may be due to real effects, such as a change in the mode of operation of the examined process. This may, for example, take the form of a change from surface flaws to bulk flaws in a reinforcing fibre, as the length changes.

Weibull (1951) notes that, although there is no theoretical basis for his expression, it is found empirically to fit many situations. It is also an easy expression to use. The power law function used by Weibull (1951) in the equation is the simplest expression which he found to give a good fit to his data, and suggested that this expression should only be used while the fit was good.

When used to analyse reinforcing fibres, the equation proposed by Weibull takes the form

$$P_f = 1 - e^{-V\left(\frac{\sigma - \sigma_u}{\sigma_o}\right)^m} \qquad 2.4$$

where P_f is the probability of fibre failure, σ is the applied stress, σ_u is the stress below which no fibres fracture (commonly assumed to be equal to 0), V is the fibre volume, m takes the meaning indicated in equation 2.3 and σ_o is equivalent to χ_o. In the case of reinforcing fibres, as the flaw distribution depends on the volume of the fibre (increased volume increases the likelyhood of a large flaw being present), a volume correction term is necessary. This is taken into account by the inclusion of the volume term in equation 2.4. If the flaw distribution was assumed to be active only at the surface of the fibre, for example, being due to scratches present at the surface, then V in equation 2.4 would be taken as the surface area of the fibre. Thus, this equation is only strictly applicable for fibres with constant volume or surface area. If this is not taken into account scatter will be introduced in the results. It is,

however, commonly assumed that reinforcing fibres have a single diameter, with only their length being varied.

Despite the number of alternative distributions which have been proposed (Baxevanakis et al. (1993), Gurvich et al. (1997)a, Zhu et al. (1997)), the power function proposed by Weibull (1951) seems to be the most widely adopted expression (Gurvich et al. (1997)b, Chi and Chou (1983), Favre and Jaques (1990)).

2.1.2.2. Testing of fibres to determine the statistical parameters

In order to establish the statistical failure parameters individual fibres, bundles of fibres or embedded single fibres can be tested. All of these approaches have been used successfully by various researchers. The advantages and disadvantages of each method are shown in table 2.2, along with the authors who have adopted each approach.

Sample type	Advantages	Disadvantages	Users
Single fibres	Easy diameter measurements. Easy to monitor number of fibres tested.	Sensitive testing machines needed ((Marsh (1959) and (1961), Biddulph et al. (1994)). Fibres selected, possibly rejecting the weakest fibres.	Wagner et al. (1984) Chi and Chou (1983) Favres and Jaques (1990) Varelas et al. (1997) Wilson (1997) Pan et al. (1997) Mili et al. (1996)
Fibre bundles	No prior selection of fibres. Can give data on fibre interactions. One test gives lots of data points.	Impossible to measure the diameters of individual fibres. Difficult to monitor fibre fracture.	Cowking et al. (1991)a and (1991)b Hill and Okoroafor (1984) Mili et al. (1996) Chi et al. (1984)
Embedded fibres	Can give Weibull data and adhesion data in one test. Reduces handling problems. One fibre gives multiple data points. Gives Weibull data for fibres in their service environments.	Fibres selected, possibly rejecting the weakest fibres. Not a direct measure of the fibre strength, the analysis methods infer the Weibull values from the data.	Netravali et al. (1989) Wagner and Eitan (1990) Anderson and Tamuzs (1993) Shioya and Takaku (1995)

Table 2.2. Comparison of three methods used to obtain data on the statistical flaw distribution within reinforcing fibres.

Due to problems associated with fibre handling and also the fact that one test would provide both Weibull data and adhesion data, embedded fibres were selected for use in this study.

2.1.3. Stress concentrations in multi-fibre composites

The single fibre fragmentation test provides information on the adhesion between a reinforcing fibre and the matrix resin and can also give data on the fibre strength distribution. However, it gives no information on the interaction between fibres in the vicinity of a fibre break. The presence of a fibre break will cause a stress concentration in the resin around the break. This will affect any reinforcing fibres close to the break, increasing the likelihood of failure. The existence of these stress concentrations has been clearly demonstrated by Fiedler and Shulte (1997)a, who carried out a photoelastic study on single-fibre model composites. Their results showed the stress concentration spreading through the resin in the region of a broken fibre.

A number of authors have attempted to predict the failure stress of composite materials. Early work was carried out by Daniels (1945) who examined an unembedded bundle of fibres. He analysed the problem by assuming that the excess load, upon breakage of a fibre, was equally shared among the remaining fibres. This approach was adopted by Rosen (1964) in his model to predict the tensile stress at which a composite would fail. However, the assumption of load sharing is not thought to be applicable to composites and, hence, would present a limitation of this model. No consideration of a stress concentration was given in this study and was noted by the author as a limitation of the approach. Zweben (1968) extended Rosen's model to overcome some of the limitations in the earlier work. This included the introduction of a stress concentration factor. The

approach used to define the stress concentration factor was that of Hedgepeth and van Dyke (1967) presented shortly.

More recently, Wisnom and Green (1995) modelled the failure of composites, by examining the interaction between fibre breaks. They included no stress concentration factors in their analysis, using only the statistical failure properties of the fibres. They predicted that, once there were sufficient broken fibres in a small area, the breaks would interact. When the breaks interacted, that volume of composite would pull out of the rest of the composite. This would clearly be a catastrophic failure event. Their predictions were found to compare well with experimental data, despite no stress concentration being considered.

Measurements and predictions concerning the level of the stress concentration resulting from a fibre fracture have been made by a number of authors. The values predicted by various authors, and the method used to derive this value are shown in table 2.3.

Authors	Method used	Value predicted for the nearest neighbour	Value predicted for the next nearest neighbour
Hedgepeth and van Dyke (1967)	Mathematical analysis	1.33 (2D case)	---
Nedele and Wisnom (1994)a and (1994)b	Finite element analysis	Not significant	---
Feidler and Schulte (1997)b	Finite element analysis	1.46 (3D case)	1.15 (3D case)
van den Heuvel et al. (1997)	Laser Raman spectroscopy	1.26 (2D case)	---
Chohan and Galiotis (1997)	Laser Raman spectroscopy	1.36 (2D case) 1.24 (3D case)	---

Table 2.3. Various predictions of the level of stress concentration caused by a fibre fracture.

Fukuda and Kawata (1976) found that the properties of the composite significantly affected the stress concentration, although their predicted values were similar to those of Hedgepeth and van Dyke (1967). Ochiai et al. (1991) also found that the matrix properties were significant. They found that the maximum stress concentration occurred when a crack ran into the matrix resin, from the fibre. Wagner and Eitan (1993) and Wagner et al. (1996) found that the overall stress concentration was much lower than that predicted by Hedgepeth and van Dyke (1967). However, in similarity with most other authors, they found that the number of broken fibres in an area, and also the volume fraction of fibres, both significantly altered the stress concentration.

It can be seen from table 2.3 that there is no consensus at the present stage as to the size of the stress concentrations operative in composite systems. However, there is consensus upon the fact that high volume fraction and the presence of other broken fibres both increase the level of the stress concentration. Due to this lack of consensus, for the purposes of this study the levels of stress concentrations to be used are the 1.33 predicted for a 2D composite by Hedgepeth and van Dyke (1967) and also the 1.15 predicted by Fiedler and Schulte (1997)b for the next-nearest neighbouring fibres. The first value has been chosen, as the 1.33 predicted by Hedgepeth and van Dyke is similar to the limiting value, when close contact occurs between the fibres, for most of the studies. The second has been chosen as it is one of very few, if not the only, published value for the

stress concentration factor in the next-nearest neighbouring fibres.

2.2. Damage Mechanisms in Composites

An understanding of the damage mechanisms in composite materials has long been recognised as vital for them to be widely adopted in critical applications. Studies on the failure of long fibre reinforced polymers were being carried out in the early 1960's. Broutmann (1965) studied delamination in glass fibre reinforced composite tubes, finding that compressive failure and delaminations occurred significantly before the expected failure strain was reached. Throckmorton et al. (1963) studied the effect of coupling agents on the failure characteristics, again in glass reinforced polymers.

The nature of failure depends on the loading regime experienced by the composite. Therefore, for the purposes of this study it has been decided to limit the area studied to impact damage.

2.2.1. Impact Damage

It is observed that impacted composites can sustain property degradation, while showing little visible sign of damage at the surface. Thus, damage due to impact is very important and an understanding of impact damage is critical to the use

of composites. Two types of impact are generally considered, these being low velocity impact and high velocity, or ballistic, impact. These have very different damage characteristics and this study will concentrate on low velocity impact damage. The study will also be limited to sub-perforation impacts, because the key aim is to locate and quantify barely visible damage.

2.2.1.1. Methods of impact testing

A number of ways of inducing controlled impact damage are available, including Charpy and Izod test methods as well as drop-weight and dropped-dart impact testing and static indentation. A number of authors have examined each of these methods, with their findings being summarised in table 2.4.

Test method	Advantages	Disadvantages	References
Charpy and Izod testing	Ready availability of test equipment	Loading not characteristic of impact damage.	Cantwell and Morton (1991) Owen (1981)
Drop-weight and dropped-dart testing	Good modelling of impact damage situations	---	Cantwell and Morton (1991) Owen (1981) Kaczmarek and Maison (1994)
Static indentation	Progressive deformations can be easily produced Equipment is readily available.	Results need extrapolation to impact situations.	Owen (1981) Kaczmarek and Maison (1994) Sjoblom et al. (1988)

Table 2.4. Comparison of test methods available to induce impact damage.

After studying the above works it can be concluded that, as long as care is taken in the analysis, both static loading

and drop-weight impact testers can be used to study impact induced damage in composites. However, such test methodologies as Charpy and Izod testing are unsuitable.

2.2.1.2. Damage morphology

Impact damage can only consist of fibre fracture, delamination and matrix cracking. The exact nature of the induced damage will depend on the properties of the composite, the lay-up sequence and the laminate thickness (Hitchen and Kemp (1995)). External factors including the impacter geometry, the weight of the impacter and the speed of impact also affect the damage build up in the composite (Cantwell and Morton (1991), Chaturvedi and Sierakowski (1985), Woo and Chen (1995)).

The observation of damage caused by low velocity impact is difficult, as by its very nature it is internal. Thus, novel techniques are required to observe the damage, such as X-ray techniques which can be used to study delamination and matrix cracking (Hitchen and Kemp (1995)). Modifications to the standard techniques have also been proposed, which allow the inspection of fibre fracture (Highsmith and Keshav (1997)). The alternative technique of ultrasonic C-scanning generally shows only delamination (Ashbee (1989)). Both of these techniques tend to give plan views with no depth information, although this can be obtained in some cases. These and other techniques which have been used to examine damage in composites will be discussed in greater detail in section 2.2.2.

The early stages of damage development in panels subjected to low velocity impacts can be summarised in the following manner:

i). Initiation of damage occurs in the form of matrix cracks, either on the opposite side of the panel to the impact event in thin panels, or on both sides in thick plates (Ambur et al. (1995), Joshi and Sun (1985), Liu and Malvern (1987)).

ii). Where matrix cracks intersect, delaminations can form (Joshi and Sun (1985), Lammerant and Verpoest (1996)). However, not all matrix cracks will lead to delaminations (Liu and Malvern (1987)).

iii). Delaminations propagate as the impact progresses, frequently forming a characteristic 'peanut' shape, consisting of a wasted rectangle (Hitchen and Kemp (1995), Joshi and Sun (1985), Liu (1988), Wu and Springer (1988)). This shape has been found to occur due to bending mismatches between the plies (Liu (1988)). The mismatch in bending stiffness has also been found to relate to the total delamination area (Hong and Liu (1989), Hitchen and Kemp (1995)). Methods by which the location and extent of delaminations can be predicted have also been developed (Hitchen and Kemp (1995), Clark (1989)). Delamination is also generally found to increase in size towards the non-impacted face of the composite.

The final mode of failure is fibre fracture. This occurs as the panel bends, with fibre failure occurring due to tensile or compressive stresses (Richardson and Wisheart (1996)). The failure of fibres occurs in the later stages of impact damage and leads to ply splitting and ultimately to penetration.

Delamination due to impact causes little degradation in the tensile properties, which are only significantly degraded due to damage induced in the fibres (Ashbee (1989), Richardson and Wisheart (1996)). In compression, however, the delaminated areas buckle, leading to failure and a gross reduction in the properties. Pavier and Clarke (1995) investigated this failure by replicating damage in a controlled fashion using PTFE film and cut plies to model delamination and fibre damage. They found that their replication method was valid, as the trends followed by their test pieces were correct.

The observations made in the above works have all been made on model composites consisting of thin plates. It has been suggested by other authors that results from real composite structures indicate that failure processes may differ in more complex situations (Wiggenraad et al. (1996), Greenhalgh et al. (1996), Ireman et al. (1996)).

2.2.1.3. Methods of improving impact performance

A number of authors have examined the effect of the matrix resin on the impact performance, with a view to improving

impact resistance. Boll et al. (1986) studied the effect of different resins on the damage process. They found that a low fracture energy resin gave much more extensive delamination than a high fracture energy resin. They also found that fibre fracture was more extensive in the high fracture energy resin, while transverse cracking occurred in both specimens. Lesser (1997) examined the effect of crosslink density on impact damage. His results showed that a decrease in crosslink density gave an increase in the impact damage resistance within the composite. Xian and Choy (1994) examined the use of a modified bismaleimide resin to toughen the composite. They found that there were two critical energies under impact, one to initiate damage and one leading to critical damage. They also found that the nature of the matrix was very significant in determining the impact performance of the composite.

Studies on environmental changes can also be used to infer the effect of altering the matrix resin, by studying the resin both above and below the glass transition temperature (T_g). Such studies have indicated that the energy at perforation of the composite did not depend on the resin. However, at energies below perforation, the resin flexibility was found to be critical in determining the extent of damage (Bibo et al. (1994) and (1995)). Karasek et al. (1995)a and (1995)b found that moisture did not affect the damage at temperatures below the resin T_g, but above the T_g the damage increased dramatically in a moist environment. It was also found that the initiation of damage occurred at higher energies with more flexible resin, but once the damage had initiated its extent was greater. Cantwell (1996) backed up

this data, indicating that at temperatures below the T_g the impact performance was constant.

An alternative approach, by which the impact resistance can be altered, is modification of the fibres. This is achieved by using a mix of fibres, to form a hybrid fibre composite. Hitchen and Kemp (1996) presented results for a cost effective hybrid composite under impact. The system they developed consisted of high performance carbon fibres in the principal directions, with standard carbon fibres in the secondary directions. By optimising the lay-up sequence, the properties of the composite could be made to approach those of the high performance fibres, while reducing the cost. Impact performance was maximised by careful choice of the lay-up sequence. Khatri and Koczak (1996) used E-glass fibres to increase the resistance of carbon fibre/polyphenylinesulphide composite to flexural loading. Their results showed that careful placement of the hybridising fibres gave a distinct enhancement in the flexural properties of the composite. Their results also showed that failure of the carbon fibre sections was delayed, due to the support provided by the E-glass reinforced regions. This led to an overall increase in the load to failure of the composite.

Other ways in which the impact performance of composites can be adapted involve the use of a third dimensional element to link the plies together. These can consist of a woven composite, stitching to hold the fibre bundles together and also the inclusion of short fibres randomly oriented, to bridge the interface between plies. Authors who have

examined the effect of these materials on the impact performance include Bibo and Hogg (1996), Lagace and Wolf (1995) and Wu and Liau (1994).

2.2.2. Sensing of Impact Damage

2.2.2.1. Remote sensing techniques

The technique of C-scanning involves directing pulses of ultrasonic waves through the sample and detecting the time taken for the pulses to reach a sensor (Mallick (1988), Ashbee (1989)). A contact fluid, commonly water, is generally required to ensure good transfer of the ultrasonic waves between the transducer and sensor via the sample, although Cawley (1994) presented a system which used a laser beam to replace the contact medium. The sensor can either be placed opposite the source, on the other side of the specimen, or on the same side as the source, using reflected waves for condition monitoring. Any damage present within the composite will lead to different transmission characteristics in these regions, when compared with undamaged regions. This results in time of flight changes between source and detector, thus, enabling damage to be detected. The basic technique gives defect size data but little else, so efforts have been made to obtain more information, either through more accurate measurement of the plan view (Smith (1994)) or through implementation of 3D viewing.

Authors who have presented ways of modifying standard C-scanning equipment to give 3D data include Scarponi and Briotti (1997) and Kaczmarek (1995). Their results allow information on the extent of delamination between individual pairs of plies and also on the location of matrix cracking in the composite to be obtained.

An alternative approach to the classic C-scanning arrangement was presented by Wooh and Daniel (1994), using ultrasonic A-scanning. This was done because A-scanning has the potential to provide more information than either B-scanning or the more common C-scanning. They describe a testing system and also archival and processing techniques. The problems with such a system include the amount of data generated from a single a-scan prior to processing. To overcome this, an efficient waveform compression program was proposed. The final system was then capable of detailed 3D imaging of damage within the composite.

Another approach which is based on the modification of sound waves by damage is the use of Lamb waves (Cawley (1994)). In this technique, sound waves are induced in a specimen and allowed to propagate through it. The presence of damage will modify the propagating waves and can, thus, be detected using a sensor to monitor the waves in the composite.

As well as X-ray radiography and the use of sound waves, a number of other techniques exist for the remote observation of composite panels. These include thermographic techniques, electrical techniques and also various optical approaches (Scott and Scala (1982)).

The heat flow differences between damaged and undamaged regions can be used to detect the presence of damage, in a technique called thermography. A panel is heated, commonly using an infra-red heat source, and then imaged using a thermal imaging camera. Defects within the panel show up as areas of inhomogeneous heating (Vavilov et al. (1993), Scott and Scala (1982), Cawley (1994)). This generally requires the heat source to be turned off before the thermal imaging camera is turned on, otherwise the camera, which images in infra-red, will be dazzled by the heater. Kaiser (1993) presented a thermographic imaging arrangement which overcame this problem by using millimeter-waves to heat the panel.

Optical techniques can also be used to monitor surface or bulk inhomogeneities. Surface inhomogeneities will be present after an impact, in the form of deformation and distortion due to cracking and delamination within the structure. These distortions have been examined using various interferometric techniques. Interferometry provides very sensitive methods of measuring the distortion and, thus, allows the damage to be precisely located and measured. Authors who have presented such techniques include Komorowski et al. (1990), Scott and Scala (1982) and Cawley (1994).

Electro-magnetic examination can be employed to locate the inhomogenious material resulting from an impact. The technique of eddy-current examination can, however, only be applied to composites containing electrically conductive fibres, such as carbon fibres (Scott and Scala (1982), Gros and Lowden (1995), Shelley (1996)). This technique relies on

the electrical conductivity of the fibres, which is affected by the presence of impact damage. Measurement of the panel is carried out in a point to point manner, allowing a 2D image of the damage to be obtained. The level of the response from the panel gives an indication of the extent of impact damage.

An unusual approach was proposed by Haque and Raju (1995) which looked at the stiffness degradation in the region of impact damage. This technique involved light, instrumented, tapping of the sample. The response of the panel was detected by the instrumentation within the tapping probe and was found to vary when damage was encountered. In this way, the presence of damage could be monitored and its size detected using a pulse width or force amplitude measurement.

2.2.2.2. In-situ sensing techniques

Techniques for sensing the damage development in real time, in-situ, are also important. The methods discussed previously are generally only applicable for use with the panel removed from any structure. For the location of impact damage when the panel is contained in a structure, alternative techniques have been developed.

A variety of piezo-electric based sensors have been used to locate impacts impinging on composite materials. These sensors have been used to monitor the acoustic waves associated with an impact event, the deformation associated with an impact event or changes in the sample resulting from

an impact event. Among the authors who have used the acoustic waves propagating as a result of an impact event or panel distortions are Campbell et al. (1993), Okafor et al. (1996), Joshi and Munir (1996) and Jenq and Chang (1995). Campbell et al. (1993) used polyvinylidenefluoride (PVDF) film as the piezo-electric element used to monitor both strains in the panel and also the transient waves associated with impact. Okafor et al. (1996) used three sensors to allow impact location to be established by triangulation. Joshi and Munir (1996) used a more complex panel with stiffeners attached, in order to mimic a real structure. They found that using a neural network enabled them to locate the impact events, despite the presence of the stiffeners. In contrast to the above works, Jenq and Chang (1995) used PVDF film to allow them to follow the distortion of the panel during an impact event.

Authors who have used changes in the panel, as a result of an impact event, to monitor the presence of impact damage include Okafor et al (1995), Neary et al. (1996) Tan et al. (1995) and Smith and Hoa (1994). Neary et al. (1996) and Tan et al. (1995) used fixed piezo-electric elements to monitor Lamb waves. The damage was detected in the manner described in section 2.2.2.1. Smith and Hoa (1994) used PVDF film to monitor both Lamb waves and surface acoustic waves, again allowing damage detection. An alternative approach was used by Okafor et al. (1995), who used changes in the modal frequency response of the sample to monitor delamination size. The data was processed using a neural network which had been trained using standard samples.

The use of optical fibre sensors as a method of monitoring the occurrence of impact on a composite panel has also been demonstrated by a number of authors. Early work on the use of optical sensors was published by Hale et al. (1980), in which optical fibres were used to monitor strain levels in a specimen of steel. They discussed a method of reducing the strength of an optical fibre to a controllable level, so that its failure strain was precisely known. At fracture of the fibre, this meant that the strain in the specimen was known. Hofer (1987) used this crack detecting system as the basis of a damage detection method for use in aerospace applications. His proposal was that the fibres could be used either embedded, or surface mounted on to the sample. Measures et al. (1989) presented a detailed examination of a similar system to that used by Hofer. However, their results included an examination of the effect of fibre embedment on the properties of the composite. Their paper suggested that the inclusion of optical fibres had a negligible effect on the properties of the composite, both in tensile and compressive loading.

Grace et al. (1996) used a similar system to those discussed above but extended it to provide an impact location method. The embedded optical fibres were arranged in a grid or spiral within the panel so that a large proportion of the panel was covered. The use of optical time domain reflectometry (OTDR) allowed the location of impact induced breaks within this grid to be ascertained.

Dry (1995), (1996) and Dry and McMillan (1997) used hollow glass fibres filled with a liquid resin to form a system

which was capable of detecting cracks in a similar way to the above works. However, upon fracture the resin contained in the fibre flowed from the core and effected a repair. Preliminary results have been obtained, which show the system to be capable of performing both functions.

A variety of more complex non-interferometric sensors have also been employed in impact damage detection. Jianliang et al. (1996) etched castelations into an optical fibre so that it acted as a microbend strain sensor. They proposed that this arrangement, along with a neural network, would enable the detection of impact events. The work of Noharet et al. (1995) used polarisation maintaining fibres with a hole either side of the core to monitor impact events within a sandwich composite panel. Modelling as to the effect of the sensor were carried out with particular interest in its performance under multiple impact events.

Various types of interferometric sensor have been proposed, to give a more sensitive sensor than the non-interferometric types. The most common of these is the Fabry-Perot interferometer. Greene et al. (1995) used a composite panel containing four embedded Fabry-Perot interferometers. Comparison of the time delay between the signal arriving at each sensor was used to calculate where the panel had been impacted, allowing the impact location to be found with a high degree of accuracy. A paper by Chang and Sirkis (1995) used both the Fabry-Perot interferometer and also a path matched differential interferometer to study impact events. Both types of interferometer were found to be capable of detecting impact on composite materials. Schindler et al.

(1995) also used surface mounted and embedded Fabry-Perot sensors. In this case, however, the impact location was predicted using a neural network.

Akhavan et al. (1995) compared the performance of the Fabry-Perot sensor with both PVDF piezo-electric sensors and also standard electrical resistance strain gauges. The performance of the optical sensor was found to be superior to that of the electrical resistance gauge, particularly in responding to the transient shock waves experienced in impact.

Other interferometric sensing systems have also been employed. Malki et al. (1996) used intermodal interference in multimode optical fibres to examine both vibration and impact detection within composites. Again a grid of fibres was used and time delay between the wavefront arriving at each sensor allowed accurate position location. Pierce et al. (1996)a and (1996)b used an optical fibre as an acoustic wave sensor in a damage detection system. In their arrangement, an ultrasound transmitter was used to launch Lamb waves into the composite. The waves were reflected from holes or damage within the composite. To detect these reflected waves, an optical fibre, which made up one arm of a Mach-Zhender interferometer, was surface mounted on the composite. It was found that larger defects gave a larger signal reflection and, thus, damage could, to an extent, be quantified.

2.2.2.3. Neural networks for damage characterisation

The use of neural networks to locate impacts has generated a significant amount of interest. A number of authors have proposed neural network designs specifically for damage location. These have not been tested using optical sensors and composites, but the network structures should be applicable. Shaw et al. (1995) developed a mathematical model to describe the deformation of a fully clamped homogeneous isotropic rectangular plate. Having developed this analytical description they proposed a neural network methodology which could be used to give impact location. Simulated sensor data was generated using a mathematical model, and used to assess the accuracy of the neural network. The precise results would depend on the sensor type employed and experimental processes among other factors, so full assessment was not possible. The process did, however, show itself to be capable of locating impact events with a good degree of accuracy, using resistance strain gauges, with no post processing. Jones et al. (1995) proposed a further two neural networks which could be used to monitor impact location on a plate. Their networks were tested using an aluminium specimen with four strain gauge sensors mounted on the corners of the plate.

2.2.2.4. Effect of embedded optical fibres on the composite

The use of optical fibres within a composite structure raises a few questions. Optical fibres distort the composite in such a way that a resin rich region exists around the fibre.

The size of this varies with the exact geometry of the composite specimen. A number of studies have been made to discover the effect of the embedded optical fibre on the properties of the composite.

Sirkis et al. (1994) and Sirkis and Chang (1994) have written papers looking at the effect of embedded fibres specifically on the impact performance of composites. They first examined the macro-scale failure processes, such as delamination. They concluded that no effect was observed to suggest that the embedded fibres affected delamination formation within the specimens. This was consistent among a number of different lay-up sequences. The same lay-up sequences were examined in the second paper, which looked at micro-scale fracture within the composite. Their conclusion from this study was that small optical fibres (80-125 μm) had no influence on the fracture pattern. Larger optical fibres (>200 μm) were found to influence it.

Sirkis and Lu (1995) used modelling to examine the effect of a polyimide coated optical fibre on a composite. Their results for this arrangement indicated that the optical fibre gave no degradation to the longitudinal tensile properties. However, transverse tensile and compressive strength was found to be significantly degraded.

Sirkis and Singh (1994) used Moiré analysis to examine whether the embedded optical fibre gave a stress concentration within the composite. It was found that no stress concentration existed, using the precise geometry considered in this study. Goldrein et al. (1996) also used

Moiré fringes to study the effect of strain on an embedded optical fibre. Their specimen consisted of an embedded optical fibre embedded within a carbon fibre composite, with the fibres running parallel to the optical fibre. This specimen was loaded perpendicularly to the fibre in tension and the resultant strain was monitored. It was found that the bulk composite was strained to a much higher level than that experienced by the optical fibre.

Seo and Lee (1995) studied the effect of embedded optical fibres on transverse crack spacing within the composite. They also examined the effect of coatings on the crack spacing. Their findings showed that there was a very slight reduction in transverse crack spacing in composites containing embedded fibres, regardless of whether the fibres were embedded in the loading direction or purpendicular to it.

Levin and Jarlås (1997) carried out a study to establish the effect of impact damage on the performance of embedded optical sensors, specifically Fabry-Perot interferometry. Their findings showed that the sensor was less vulnerable when embedded within the centre of the composite. The sensor was found to increase damage when embedded within some areas of the composite and debonding was found to be the most detrimental damage mode, as far as sensor performance was concerned.

2.2.3. Conclusions

It can be seen that both remote and in-situ sensing techniques are readily available. However, the only well developed techniques are C-scanning and x-ray radiography. In particular, the use of optical sensors raises problems with the properties of the composite, although their precise effect is not known. The in-situ approach seems to offer significant advantages over remote techniques in as much as the data can be obtained in in-service conditions. However, both have a role to play in damage detection in composites.

Chapter 3. Results 1: Examination of the Raw Materials

This chapter examines the constituent materials required to produce a light-guide from reinforcing fibres. The optical characteristics of the raw materials are examined and necessary pre-treatments of the fibres are discussed.

3.1. Examination of the Constituent Materials

3.1.1. Quartzel Glass

The glass reinforcing fibres selected for use in this study were 99.99% pure silica fibres produced by Quartz et Silice, under the trade name Quartzel glass fibres.

3.1.1.1. Experimental procedure

Rods of Quartzel glass with a diameter of 5 mm were obtained and ten sections of 10 mm length were cut from random positions. These were examined for voids and solid contaminants, using a stereo microscope, with light being transmitted through them in order to silhouette any contained faults. Photographs of the observed sections were taken.

The density of the glass was measured, to ensure that the amount of voiding within the sample was not excessive, using a Hubbard pyknometer. The apparent density of each glass rod was measured according to BS 733 parts 1 and 2 using a standard temperature of 23°C +/-0.2.

3.1.1.2. Results and Discussion

The glass used to produce the reinforcing fibres was 99.99% pure silica, with a chemical composition of impurities shown in table 3.1, as quoted in Quartz et Silice product literature.

Trace Element	PPM by weight
Al	17.7
B	0.09
Ca	0.5
Cr	0.08
Cu	0.05
Fe	0.6
K	0.6
Li	0.7
Mg	0.06
Na	0.8
Ti	1.5

Table 3.1. Typical analysis of the major impurities within Quartzel glass.

The presence of voiding within the glass rods is shown in figure 3.1. It was observed that the majority of the voids were elongated along the length of the rod. This is thought to be due to the extrusion of the rod from the molten glass.

The average density measurement and standard deviation is given in table 3.2, along with the theoretical value of density for high purity silica. It was found that the percentage of voiding was very low. No direct evidence of the presence of voids, within the reinforcing fibres themselves, was found. However, the existence of voids could not be disproved. The presence of voiding within the raw material may lead to microfine voids in the fibre centres (Loewenstein (1983)). If these voids were present, then the light transmission characteristics of the fibres would be compromised and, thus, the possibility of their presence cannot be ignored. This study was carried out using readily available raw materials and, thus, no action to eliminate the voiding could be taken. The observed problems could be overcome with specially produced fibres.

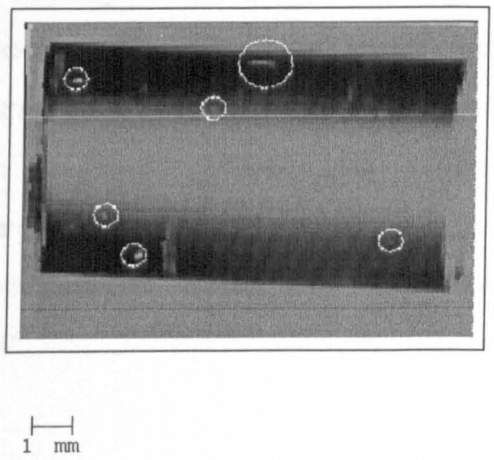

Figure 3.1. Picture of voiding within rods of Quartzel glass.

	Density kg/m³	Standard deviation
Average density of Quartzel rods	2.16	0.08
Theoretical density of silica	2.20	---

Table 3.2. Showing the comparison of the average density of the rods with the theoretical density of silica.

3.1.2. Cladding Materials

3.1.2.1 Experimental procedure

A number of potential cladding materials were obtained and the refractive index of each was measured. This was carried out using an Abbe refractometer with a sodium 'D' line light-source, having an emission wavelength of 489 nm. Thin specimens of each potential cladding material were prepared and examined. Bromonapthalene was used as a contact fluid, to ensure that good transmission was obtained between the prisms of the refractometer and the sample. This was chosen as it had a much higher refractive index than the silica glass. Three refractive index measurements were carried out for each of the potential cladding materials, at a standard temperature of 25°C.

3.1.2.2. Results and Discussion

The measured refractive indices of each of the potential cladding materials is plotted on a graph, shown in figure 3.2. A line is plotted on the graph marking the refractive index of the silica glass. There is also a line showing the

refractive index of the contact fluid. Any potential cladding materials were required to have a refractive index which fell below that of the silica glass, to satisfy physical requirements for light-guide operation.

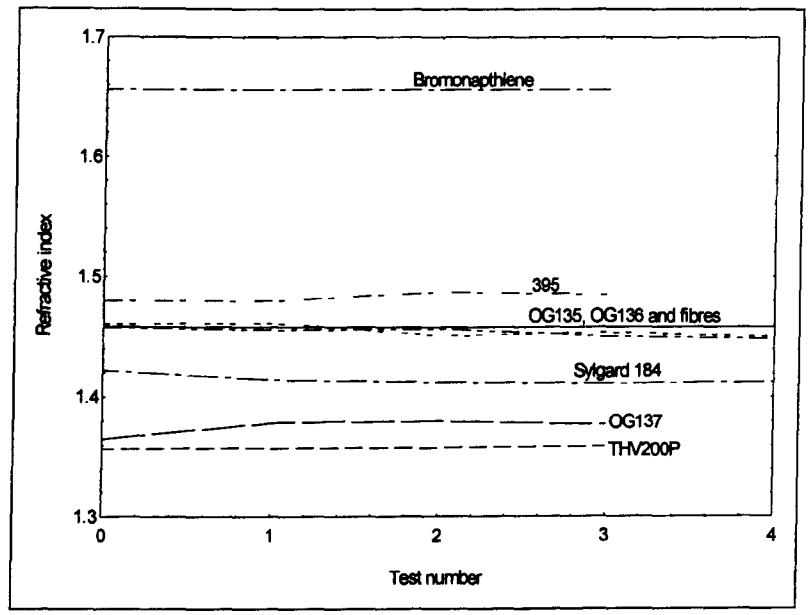

Figure 3.2. Graph showing the refractive indices of potential cladding materials.

It can be seen, therefore, that the cladding materials which were suitable for use were:

i). 3M THV 200P

ii). Dow Corning Sylgard 184

iii). Epoxy Technologies OG 137.

Epoxy technologies OG 135 and OG 136 both had refractive indices very similar to that of the silica glass. The

measured values indicate that these materials may be suitable, but the refractive index is too close to that of the fibres for good light-guiding characteristics (see chapter 5).

Dow Corning Sylgard 184 was found to give good coatings due to its liquid mix and relatively long cure time of 1 hour at 100°C, ensuring that bubbles were eliminated. Epoxy Technologies OG 137 was processed from a solvent, but this proved to give a bubble-filled coating. The coating was also very brittle making the light-guides difficult to handle. Bubbling was found to limit the efficacy of the 3M THV 200P too, as it was also processed using a solvent. Hence, both of these products were rejected for initial study purposes, with a view to reconsideration once the technology had been proven using Sylgard 184.

3.1.3. Transmission Characteristics of the Glass and Cladding

3.1.3.1. Experimental Procedure

A Perkin Elmer Lambda 19 UV-Vis-NIR Spectrometer was used to measure the absorption of the silica glass and the cladding materials, between the wavelengths of 200 and 850 nm. This encompassed the visible region of the spectrum, which was of the greatest interest for this study. Samples of Sylgard 184 silicone resin and OG 137 resin were analysed as

potential cladding polymers. Sections of Quartzel glass rod were also examined.

The Sylgard 184 silicone resin was cast, to give a specimen with a thickness of approximately 2 mm, which was then mounted in a standard specimen mounting card. The OG 137 resin was cast into a thin film on a glass microscope slide, to which the resin remained attatched. The thickness of this resin film was approximately 0.25 mm. The slide, including resin film, was then mounted in a standard specimen mounting card.

To measure the transmission of the silica glass, sections of the raw material, with a diameter of 5 mm, were polished to a 1 μm diamond finish, to give an overall specimen thickness of approximately 4 mm. These were then mounted within the standard specimen mounting card.

3.1.3.2. Results and Discussion

Typical absorption spectra for silica glass, Sylgard 184 and OG 137 are shown in figure 3.3. It can be seen that none of the materials absorb light to any great extent within the visible region of the spectrum. Silicone resin can be seen to have an absorption peak starting at around 200 nm, in the ultraviolet region. Silica starts to absorb at around 300 nm, again in the ultraviolet region. The cut-off point of the OG 137 is also seen to be approximately 300 nm, but this is due to the cut-off point of the glass microscope slide

substrate, rather than an inherent cut-off point of the resin. The spectra show that all of these materials have good optical transmission properties within the visible region, making them suitable for use in this study.

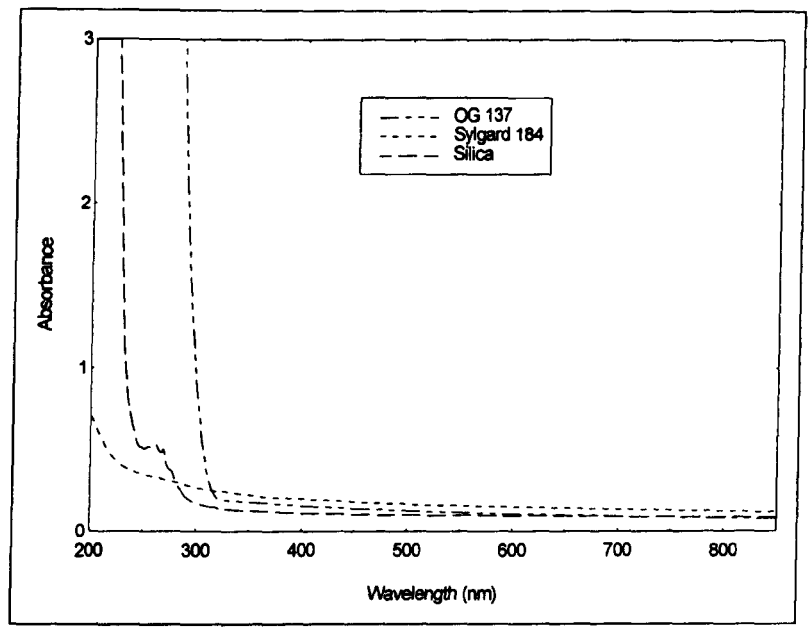

Figure 3.3. Graph showing the transmission characteristics of silica glass, OG 137 and Sylgard 184.

3.2. Light-guide Production

3.2.1. Fibre Cleaning

3.2.1.1. Experimental Procedure

The fibres, as received from the manufacturer, were coated with a protective 'size'. This was applied to protect the fibres during handling and also to improve the bonding between the fibres and an epoxy resin matrix system. For

the purposes of this study, the size had to be removed to maximise the light-guiding characteristics.

To study the effectivness of fibre cleaning and to optimise the cleaning proceedure, X-ray photoelectron spectroscopy (XPS) was used. The technique of XPS is surface specific, with a maximum depth of 10 nm being examined. Given that the fibre bundle consisted of high purity silica fibres surrounded by a polymeric size, it was decided to monitor the amount of carbon present, less carbon indicating cleaner fibres.

Two types of fibre were considered for use as the raw material, from which the reinforcing fibre light-guide (RFLG) would be produced. These will be known in this study as type 1 and type 2. Type 1 fibres consisted of a bundle of about 600 fibres, with a small amount of twist and a size coating applied at the point of manufacture. Type 2 fibres consisted of a bundle of about 200 fibres, to which neither twist nor size had been applied.

The processes used to clean the type 1 fibres were as follows:

i). Ramp at 10°C per minute to 700°C, hold at 700°C for 1 hour

ii). Instantaneous heating from ambient to 700°C, hold at 700°C for 1 hour

iii). Instantaneous heating from ambient to 700°C, hold at 700°C for 15 minutes

iv). Drawn through a tubular furnace of length 30 cm, with a nominal temperature of 700°C and a dwell in the furnace of 1.5 hours, air being passed through the furnace to remove any effluent gasses

v). Drawn through a tubular furnace of length 30 cm, with a nominal temperature of 850°C and a dwell in the furnace of 1.5 hours, air being passed through the furnace to remove any effluent gasses

fibres were also tested in the as-received condition.

Type 2 fibres were tested in the as-received condition and also cleaned using method v). This was done to confirm that both types of fibre could be cleaned in the same manner.

Cleaning methods i) to iii) were used to determine the best approach by which to accomplish size removal from the fibre surface. Once this had been established, the cleaning method was mimicked using a tubular furnace, allowing greater lengths of fibre to be cleaned. The thermal profile through the tubular furnace was measured, to monitor how well the tubular furnace mimicked the more highly controllable furnace used for methods i) to iii).

Samples were produced the day before analysis and stored over night in an evacuated dessicator. All handling was

carried out using tweezers and scissors which were cleaned with acetone and allowed to dry prior to use. Storage trays were non-plastic although the dessicator was plastic.

The samples cleaned using processes i) to iii) were cooled to approximately 50°C prior to being placed in the dessicator; this took around 30 minutes after removal from the furnace. Samples produced in the tubular furnace were exposed to the atmosphere for up to 5 hours before being placed in the dessicator, as a result of the production process. Following cleaning the surfaces were susceptible to deposition of contaminants, so, storage under vacuum was employed to limit the contact between the samples and the air. The level of contamination would be expected to be dependent on the length of time the samples were exposed to the contaminants.

The XPS test specimens were around 5 mm square, this being achieved by laying fibre bundles side by side, on a small square of double-sided tape. Care was necessary to ensure that the coverage of the adhesive tape was complete, ensuring that it was the fibre and not the tape which was examined. The prepared sample was then placed in the XPS analyser, a Vacuum Generators ESCALAB 210. Examination of the samples was carried out using a survey scan between the binding energies of 0 to 1300 eV, allowing the elements in the sample to be identified. Detailed scans were also carried out over a 20 eV range around the elements observed in the survey scan, chiefly carbon, oxygen and silicon. Peak areas were determined using the integral data

manipulation software of the system. This allowed the atomic percentages (at%) of each element to be calculated.

A perfectly clean silica surface was also tested, in order to determine the level of contamination expected to be deposited during sample storage and handling procedures. The clean surface was achieved by fracturing a silica rod into sections of suitable size for analysis. These sections were treated in two ways; three were left alongside the fibre production process for a period of 5 hours, and stored in exactly the same way as the fibre samples. Three further samples were fractured immediately prior to being placed in the analysis chamber, being exposed to the air for a maximum of 5 minutes.

3.2.1.2. Results and Discussion

Prior to discussing specific results of the XPS examination on the reinforcing fibre cleaning processes, it is critical to consider some of the limitations of XPS analysis. XPS relies on electrons being emitted from the sample due to impinging X-rays. These electrons are emitted from the sample up to a depth of between 1 to 10 nm, depending on the chemical composition of the material. Thus, XPS gives results which are very specific to the surface of the material. Hence, the results are only strictly applicable to homogeneous materials. Where a surface layer is present, it will interfere with the results, as elements only present in the surface layer will appear to be present in larger

quantities than is actually the case (Smith (1991)). The reasons for this are shown in figure 3.4. The overall tendency is, therefore, for XPS to give a distorted analysis if a surface layer is present. In order to overcome this limitation a number of alternative approaches are available. However, in this case they were not used, as precise information on the thickness of the layer was not required.

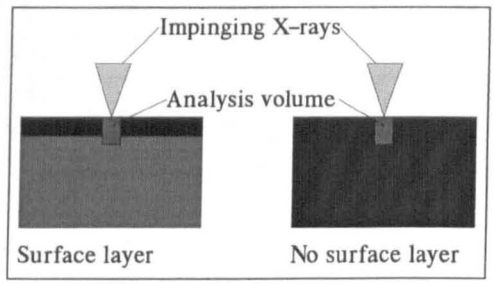

Figure 3.4. Schematic illustration of the manner in which a surface layer gives a distorted analysis of the sample composition using XPS.

The samples under consideration in this study, consisted of pure silica fibres which had been coated with a polymeric size. The cleaning temperatures used would not affect the glass, as they were significantly below its softening temperature. The carbonaceous residue would, therefore, be expected to be present as a layer on the surface.

As the material was known to be inhomogeneous at the surface, due allowance was made in the interpretation of the results. The measured percentage of carbon in the specimen was, thus, expected to be greater than would be anticipated. It was also expected that the ratio of silicon to oxygen would be roughly 1 to 2, with slightly more oxygen present due to hydration of the surface, and the presence of other

contaminants. This was found to be the case in the majority of the results.

The results from XPS analysis for the type 1 fibres in the as-received condition are shown in table 3.3. Results from XPS for cleaning processes i), ii) and iii) are shown in tables 3.4, 3.5 and 3.6 respectively.

element	C 1s	O 1s	Si 2p	N 1s
Test 1	63.9	23.3	9.4	3.4
Test 2	50.0	30.6	13.2	6.2
Test 3	57.9	27.8	10.2	4.2

Table 3.3. Atomic percentages of the elements observed in the as-received fibres.

element	C 1s	O 1s	Si 2p	N 1s
Test 1	8.8	61.4	29.8	--
Test 2	9.0	61.0	30.0	--
Test 3	13.1	60.9	26.1	--

Table 3.4. Atomic percentages of the elements observed in fibres cleaned using method i.

element	C 1s	O 1s	Si 2p	N 1s
Test 1	12.7	62.1	25.2	--
Test 2	5.7	62.2	32.1	--
Test 3	13.6	61.5	24.9	--

Table 3.5. Atomic percentages of the elements observed in fibres cleaned using method ii.

element	C 1s	O 1s	Si 2p	N 1s
Test 1	13.9	59.4	26.7	--
Test 2	21.2	53.4	25.4	--
Test 3	16.1	57.5	26.5	--

Table 3.6. Atomic percentages of the elements observed in fibres cleaned using method iii.

These results show that nitrogen, which was present in the as-received fibres, was eliminated in all the cleaning procedures. This is thought to be due to the decomposition of nitrogen-containing polymers, present in the size. It can be seen that the fibres which were held at temperature for 1 hour were significantly cleaner than those which were held for 15 minutes. However, the level of environmental contamination had not been considered at this stage. The discovery of the amount of environmental contamination was critical in this case, as the chief contaminant was carbon, an ever present contaminant.

The results from freshly cleaved silica rods are shown in table 3.7. The results from the environmentally exposed silica rods are shown in table 3.8.

element	C 1s	O 1s	Si 2p	N 1s
Test 1	7.5	64.0	28.5	--
Test 2	9.8	62.0	28.2	--
Test 3	8.0	63.3	28.7	--

Table 3.7. Atomic percentages of the elements observed in the freshly cleaved silica rod specimens.

element	C 1s	O 1s	Si 2p	N 1s
Test 1	11.4	61.0	27.6	--
Test 2	11.7	61.0	27.3	--
Test 3	10.6	61.7	27.7	--

Table 3.8. Atomic percentages of the elements observed in environmentally exposed silica rod specimens.

It can be seen that the freshly prepared samples displayed about 8 at% carbon contamination and that the exposed samples displayed about 11 at% carbon contamination. This

showed that the production and storage conditions did indeed lead to some contamination of the fibres.

Statistical analysis was used to compare the mean value of the cleaning methods, with the mean value of the standard for contamination given in table 3.8. This was done, using the ANOVA test to determine whether the mean values were statistically identical, and was carried out in the following manner:

The test statistic is

$$H_0: \mu_1=\mu_2 \qquad 3.1$$

$$H_1: \mu_1 \neq \mu_2 \qquad 3.2$$

where H_0 is the hypothesis, μ_1 and μ_2 are the means under comparison and H_1 is the alternative hypothesis, which will be accepted if H_0 is found not to apply. The hypothesis H_0 is accepted if $f<F$, where f is the value calculated and F is the value determined from the statistical F-tables.

The value F is determined in the following manner

$$F_{\alpha, I-1, I(J-1)} \qquad 3.3$$

where α is the level of significance, chosen in this case to be 5%, giving 95% confidence in the statistic. I is the number of test methods under comparison, always 2 in this study, as each cleaning method was only compared to the standard silica surface. The value J is the number of

repeats of each test, 3 in this study. Expression 3.3 then provides the coordinate position in the F-table from which F can be read.

The value f is calculated using table 3.9.

Source of variation	Sum of square	Degrees of freedom	Mean square	f
Treatments	SSTr	I-1	MSTr=SSTr/(I-1)	MSTr/MSE
Error	SSE	I(J-1)	MSE=SSE/(I(J-1))	
Total	SST	IJ-1		

Table 3.9. Table for calculating the value of f

where I and J have that same meaning as before and the other values are calculated as follows

$$SST=\sum_{i=1}^{I}\sum_{j=1}^{J}x_{ij}^2-\frac{1}{IJ}x_{..}^2 \qquad 3.4$$

$$SSTr=\frac{1}{J}\sum_{i=1}^{I}x_{i.}^2-\frac{1}{IJ}x_{..}^2 \qquad 3.5$$

$$SSE=\sum_{i=1}^{I}\sum_{j=1}^{J}(x_{ij}-\overline{x}_{i.})^2 \qquad 3.6$$

the value of x_{ij} is determined from the position of the data in table 3.10 arranged in the following manner

Sample	x_{11}	x_{12}	x_{13}
Standard	x_{21}	x_{22}	x_{23}

Table 3.10. The arrangement of data for calculating the value of f.

The other values are calculated in the following manner

$$x_{i.} = \sum_{j=1}^{J} x_{ij} \qquad 3.7$$

$$x.. = \sum_{i=1}^{I} \sum_{j=1}^{J} x_{ij} \qquad 3.8$$

and

$$\overline{x_{i.}} = \frac{\sum_{j=1}^{J}(x_{1j}) + \sum_{j=1}^{J}(x_{2j})}{J} \qquad 3.9$$

These are then entered into table 3.9, enabling the value of f to be determined and compared with the value of F from the table, to see if the conditions for H_0 are satisfied. If they are, the hypothesis is accepted and the means are considered statistically equal. If the conditions are not satisfied then the hypothesis H_1 is accepted and the means are not considered equal.

The process of comparing the data is illustrated in the following examples. Here, the data for the standard silica rods is first compared to the data for cleaning method i. The calculation is then repeated for cleaning method iii.

Tables 3.11 and 3.12 below show the data and calculation as arranged for cleaning method i.

Cleaned method i	8.8	9.0	13.1
Standard	11.4	11.7	10.6

Table 3.11. Data for the calculation.

Source of variation	Sum of square	Degrees of freedom	Mean square	f
Treatments	1.3	1	1.3	0.4
Error	11.9	4	3.0	
Total	13.2	5		

Table 3.12. Table showing the calculation of f for cleaning method i.

From the F-table, F was determined as 7.71. Comparing f with F, it can be seen that f<F and, hence, hypothesis H_0 is readily accepted.

Examining the calculation for cleaning method iii, the data for this calculation is shown in tables 3.13 and 3.14.

Cleaned method iii	13.9	16.1	21.2
Standard	11.4	11.7	10.6

Table 3.13. Data for the calculation.

Source of variation	Sum of square	Degrees of freedom	Mean square	f
Treatments	50.9	1	50.9	7.0
Error	29.1	4	7.3	
Total	80.1	5		

Table 3.14. Table showing the calculation of f for cleaning method iii.

Again it can be seen that f<F and hence H_0 is accepted. However, in this case f is much closer to the value of F and, hence, the equality of the means is more tentatively acceptable.

Given that cleaning method iii was conducted in ideal conditions in an enclosed furnace it was decided to reject the 15 minute hold of this method, in favour of a 1 hour

hold at 700°C, as studied in cleaning method i. Method i was therefore mimicked using a tubular furnace.

Upon measuring the furnace temperature it was found that the temperature barely rose above 700°C (see figure 3.5), suggesting that the cleaning process would not be as effective as method i. Results for type 1 fibres cleaned in this manner are shown in table 3.15.

element	C 1s	O 1s	Si 2p	N 1s
Test 1	21.4	54.4	24.2	--
Test 2	24.4	50.8	24.7	--
Test 3	21.1	53.4	25.6	--

Table 3.15. Atomic percentages of the elements observed in fibres cleaned using method iv.

It can be seen that cleaning was not as good as would have been expected, given the nominal temperature and length of hold. This was backed up by statistical analysis which revealed that the mean value was not comparable to that of the standard silica surface.

To overcome this problem, the nominal temperature of the furnace was increased to 850°C. Measurement of the temperature showed that in this case the temperature rose above 700°C for a total length of 20 cm (see figure 3.5). As the furnace was 30 cm long and the total dwell time in the furnace was 1.5 hours, the fibres experienced a dwell time, at greater than 700°C, of 1 hour, as required by cleaning method i. The results of this cleaning process are shown in table 3.16.

element	C 1s	O 1s	Si 2p	N 1s
Test 1	8.9	63.9	27.2	--
Test 2	11.5	59.8	28.7	--
Test 3	13.3	58.6	28.1	--

Table 3.16. Atomic percentages of the elements observed in fibres cleaned using method v.

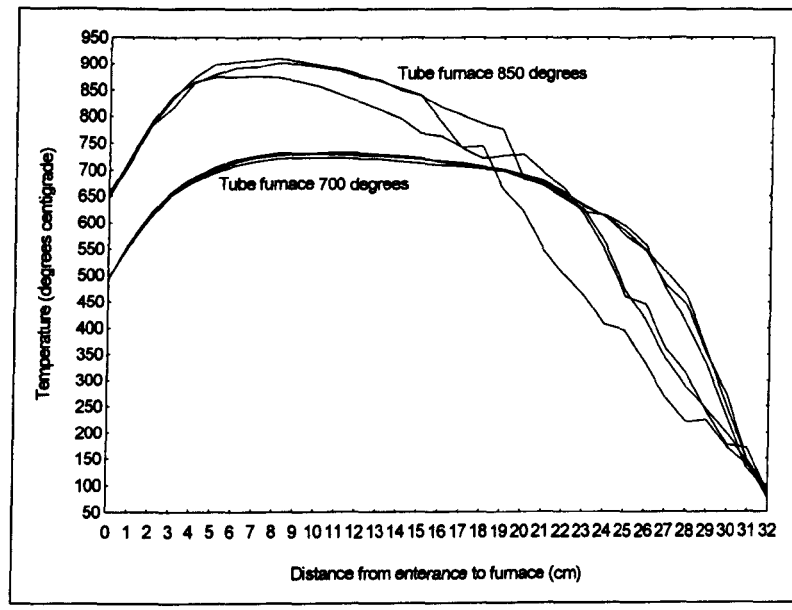

Figure 3.5. Graph showing the temperature profile through the tubular furnace at nominal temperatures of 700 and 850°C.

Here, again it can be seen that the cleaning was as expected and statistical analysis revealed the fibres to be no more contaminated than the standard. Thus, this method provided a suitable cleaning process, and became the selected method of cleaning the fibres.

Type 2 fibres were then analysed to see if the same approach to cleaning was successful. Table 3.17 shows the results of testing on the as-received fibres. The fibres were also cleaned using method v, the results being shown in table 3.18.

element	C 1s	O 1s	Si 2p	N 1s
Test 1	41.7	38.3	16.9	3.2
Test 2	51.1	32.16	13.8	3.0
Test 3	61.3	23.5	13.2	2.1

Table 3.17. Fibres of the second type in the as-received condition.

element	C 1s	O 1s	Si 2p	N 1s
Test 1	15.0	59.5	25.6	--
Test 2	13.9	58.1	28.0	--
Test 3	7.2	65.5	27.3	--

Table 3.18. Atomic percentages of the elements observed in fibres of the second type cleaned using method v.

Statistical analysis revealed that cleaning was indeed comparable to the standard and, thus, type 2 fibres could be cleaned in the same way as type 1 fibres.

3.3. Summary

The properties of Quartzel glass fibres and various potential cladding materials have been determined, to establish their suitability for use in this study. The glass used to produce the fibres was demonstrated to have suitable transmission characteristics, as were three of the potential cladding materials, Dow Corning Sylgard 184, Epoxy Technologies OG137 and 3M THV 200P. Dow Corning Sylgard 184 was selected for initial studies, with the other two being set aside for study at a later stage. The most suitable method of cleaning the Quartzel glass fibres was also established, in order to prepare them for conversion to an RFLG.

Chapter 4. Results 2: Production of a Reinforcing Fibre Light-Guide

This chapter discusses the production of an RFLG using the raw materials selected in the previous chapter. The methods used to produce the RFLG are examined and the transmission characteristics are measured

4.1. Application of the Cladding Material

4.1.1. Experimental Procedure

Application of the Sylgard 184 silicone resin to the cleaned fibre bundles was undertaken in the following manners:

i) Applying the resin drop by drop to the cleaned fibre bundle and drawing the fibre bundle between two glass rods with a gap of 70 μm between them

ii) Spray coating of cleaned fibre bundles with a solution of 10 wt% of silicone resin in cyclohexane

iii) Dip coating of the cleaned fibre bundles in a 10 wt% solution of silicone resin in cyclohexane.

Once coated, the RFLG's were embedded within carbon fibre composites and their ability to guide light was examined. Sections of the composite were then embedded within bakelite

and polished to a 1 μm diamond finish on both sides of the sample, facilitating microscopic examiation of the coating using both reflected and transmitted light.

The practicality of diluting the silicone resin with cyclohexane was studied by monitoring the viscosity of the resin during cure, once the cyclohexane had evaporated. Testing was carried out using a Rheometrics ARES parallel plate rheometer at 100°C.

4.1.2. Results and Discussion

Coating method i) proved to be unsuccessful as it was found that some areas of the fibre were well coated, while the resin failed to penetrate other areas. The coating quality is shown in figure 4.1a and 4.1b. This method of coating was therefore abandoned after initial sensing studies had been undertaken (chapter 6).

It was found that cyclohexane diluted the silicone resin and, once evaporated, did not affect it's curing. The viscosity change during cure is shown in figure 4.2. It can be seen that there is no significant difference between the two, differently treated, resin systems during cure.

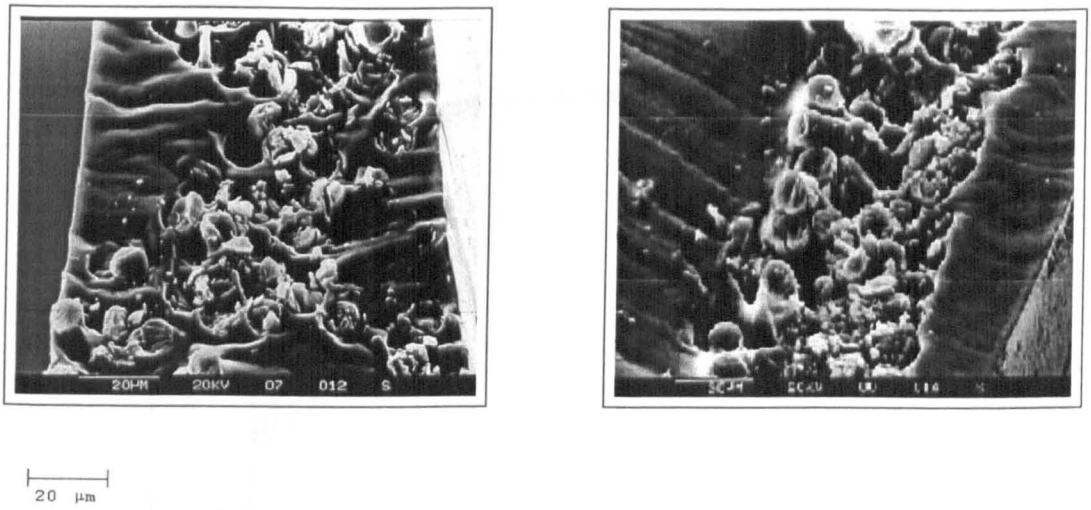

(a) (b)

Figure 4.1 a and b. Showing a well coated section of the fibre bundle and a poorly coated section of the fibre bundle respectively.

Having established that the dilution process did not affect the resin cure profile, coating processes ii) and iii) were examined. The critical requirement was that the reinforcing fibres would continue to guide light once embedded. It was discovered that spray coated fibres, once embedded, would not guide light over the required sample size of 20 cm, when only one coat had been applied. Microscopy revealed that the reason for this failure was due to areas in which the applied coating had allowed the epoxy resin to come into contact with the guiding cores. This meant that the requirements for operation of an optical fibre were contravened.

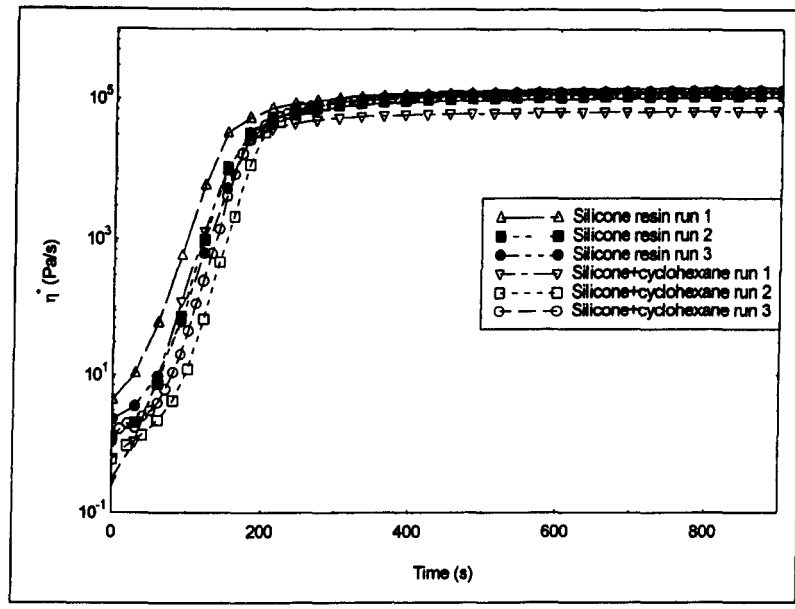

Figure 4.2. Graph showing the change in viscosity with time, of curing silicone resin.

Microscopic examination also revealed the areas in which the light guiding characteristics were best and worst. It was found that in regions where the coating was thin, the reinforcing fibres failed to guide light. However, in regions where the reinforcing fibre bundle remained closely packed and well coated, the fibres were seen to guide light well. This is shown for a spray-coated RFLG in figure 4.3a and 4.3b.

The results from dip-coated fibres showed that an even thinner layer of polymer had been deposited, preventing them from guiding light over the required length.

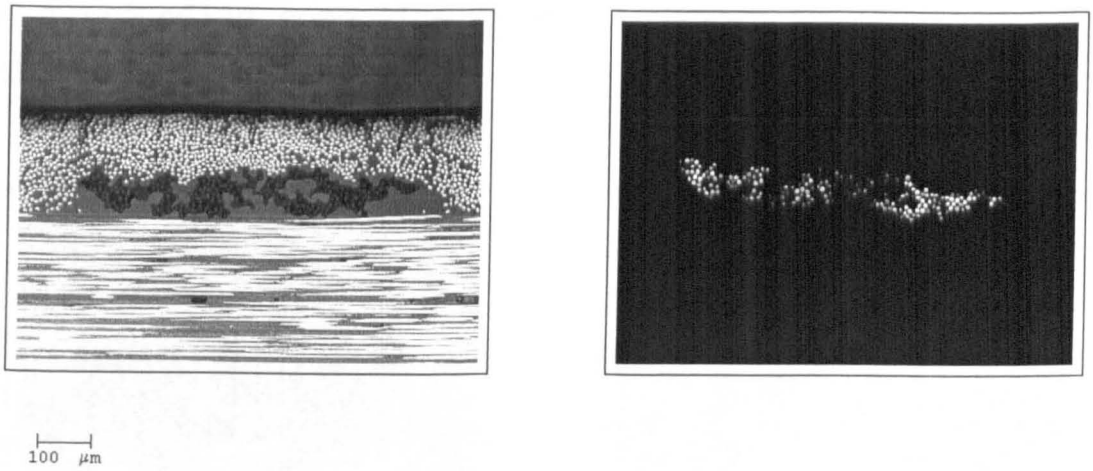

(a) (b)

Figure 4.3 a and b. Reflected and transmitted light through a spray-coated RFLG which was only coated once.

To overcome this a thicker coating had to be applied, ensuring that all areas were coated sufficiently. It was found that for spray-coated RFLG's to guide routinely over 20 cm, four coatings were required, with each being cured prior to application of the next coat. The result was that some areas of the RFLG had far too much resin present, to ensure that other areas had sufficient (see figure 4.4a). Figure 4.4b shows that the RFLG performs much more uniformly than that shown in figure 4.3b.

In the case of the dip-coated RFLG, it was discovered that 25 coatings were required with the resin being gelled after every fifth coat had been applied. The dip-coated fibres were found to have less excess resin present. This was because the resin could contact the fibre bundle from all directions, whereas spray-coating gave uneven exposure over the fibre bundle length. The low level of excess resin present in the dip-coated RFLG's, gave less distortion to

the surrounding composite. This is shown in figure 4.5a and 4.5b.

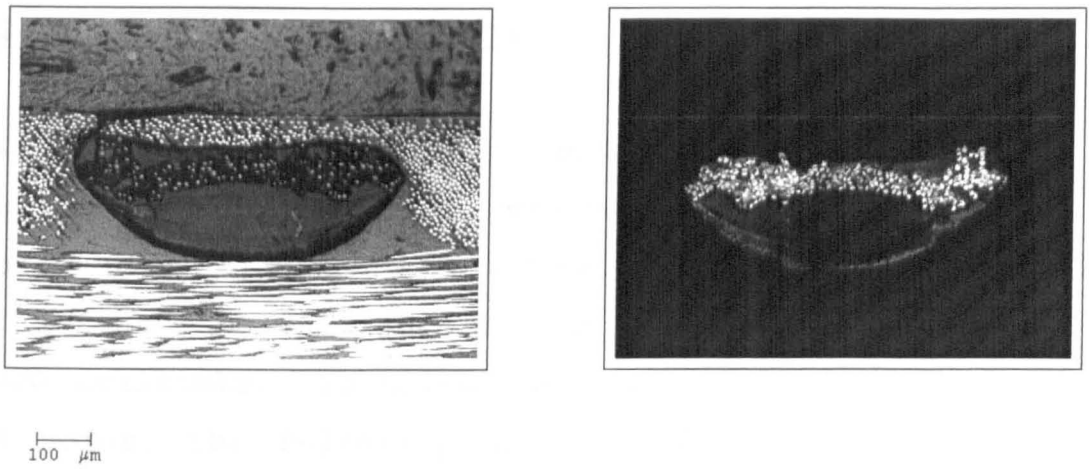

(a) (b)

Figure 4.4 a and b. Showing a spray-coated RFLG with four applied coats.

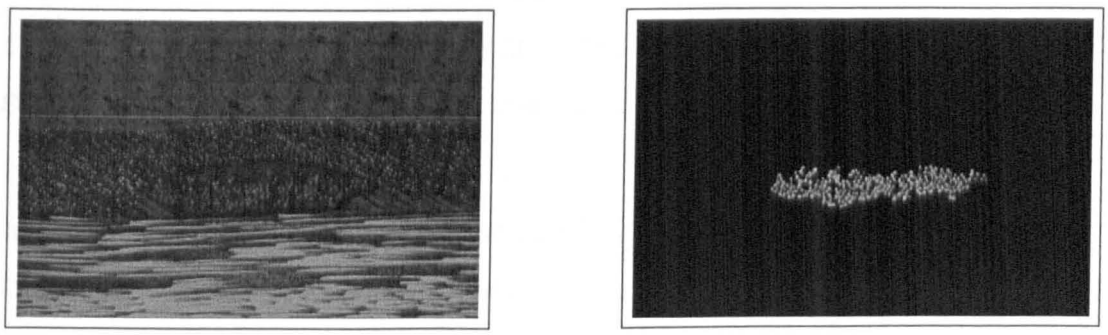

(a) (b)

Figure 4.5 a and b. Showing a dip-coated RFLG with 25 applied coats.

As a result of this study it was decided that the standard preparation of the RFLG would be to apply 25 dipped coats of a 10 wt% solution of Sylgard 184.

4.2. Volume Fraction and Void Content of the Reinforcing Fibre Light-Guide

4.2.1. Experimental Procedure

Having established the most appropriate method of applying the coating material, the resultant volume fraction (V_f) of fibres and of voids was measured. This was carried out using image analysis, due to the small quantities of coated fibre available. To allow the analysis of the V_f of fibres and voids, the following approximation was used. In the case of continuous fibre reinforced composites, the area fraction of both fibres and voids can be taken to be equal to their respective V_f's. For the purposes of testing, ten separate RFLG's were prepared and embedded within carbon fibre composite to simplify subsequent preparations. Sections of the composite were mounted in bakelite and polished to a 1 μm finish. Both optical and electron microscopy were then carried out and photographs of the RFLG's were taken. These were scanned into a personal computer and analysed using Data Translation Global-Lab Image image analysis software. It was found that the SEM photographs were low in contrast between the fibres and cladding material, making analysis difficult. However, the optical microscope images could be analysed.

Having digitised the images, particle size analysis was carried out by applying thresholding to select only the regions of the image required. In this manner, the area of the RFLG was first measured, followed by the total area of

the glass fibres and finally the total area of voids. The volume fractions of fibres and voids were then calculated for each section.

4.2.2. Results and Discussion

Results of the image analysis on the RFLG's are listed in table 4.1, with the mean and standard deviation values being shown in table 4.2.

Section number	Volume fraction of fibres	Volume fraction of voids
1	0.26	0.01
2	0.30	0.06
3	0.22	0.04
4	0.19	0.07
5	0.22	0.11
6	0.26	0.01
7	0.22	0.06
8	0.33	0.00
9	0.26	0.03
10	0.19	0.01

Table 4.1. Void content and volume fraction of fibre within the dip coated RFLG.

	Fibres	Voids
Mean	0.25	0.04
Standard deviation	0.04	0.03

Table 4.2. Mean and standard deviation values for the fibre volume fraction and void content in the dip-coated RFLG.

It can be seen that the V_f of the fibres is reasonably consistent at around 0.25, with only one section being significantly above this level. The V_f of voids is quite high in some of the sections, and insignificant in others.

Errors in this analysis are likely to be low, as there was good contrast between the different constituents of the RFLG (shown in figure 4.6a and 4.6b). Thus, measurement of the area of the RFLG's, the reinforcing fibres and the voids would be accurate, leading to low errors in the calculated values of V_f. The measurement of voids would experience the highest errors, as they will be irregular and comparitively small. It is also possible that the measured values of voiding will be inaccurate, as voids may be created during the polishing process.

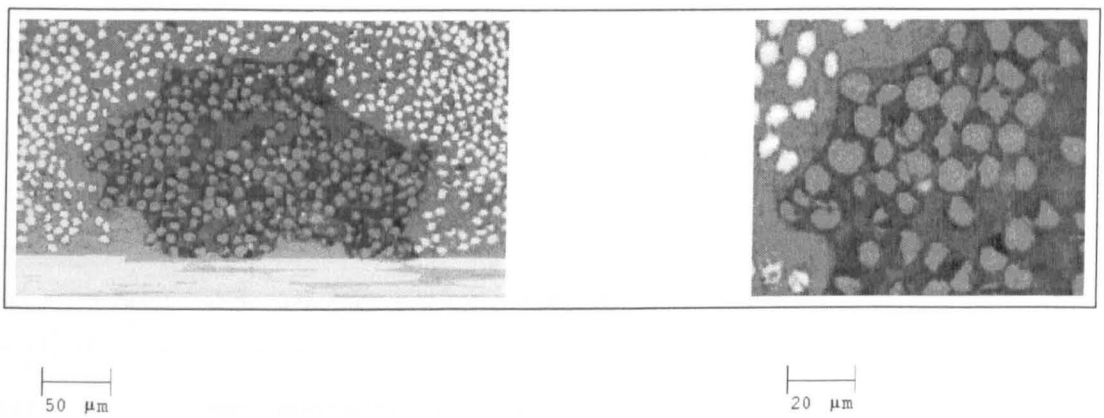

(a) (b)

Figure 4.6a and b. Photographs showing fibres and voids within a dip-coated RFLG and an enlarged section respectively.

Examination of the photographs revealed that the RFLG's with the largest fraction of voids contained a single large void within the centre. The RFLG's with volume fraction of voids of approximately 0.04 to 0.05, contained a number of small voids within the fibre bundle (see figure 4.6). It is apparent from the results in table 4.1, that some larger voids do exist and other areas of the RFLG contain no voids at all.

4.3. Transmission Characteristics

4.3.1. Experimental Procedure

In order to understand the potential and operation of the RFLG, it was necessary to test the inherent ability of the fibre bundle to guide light. As the fibres were fragile and difficult to handle, a robust method of mounting the fibres was necessary. The test specimen developed is shown in figure 4.7.

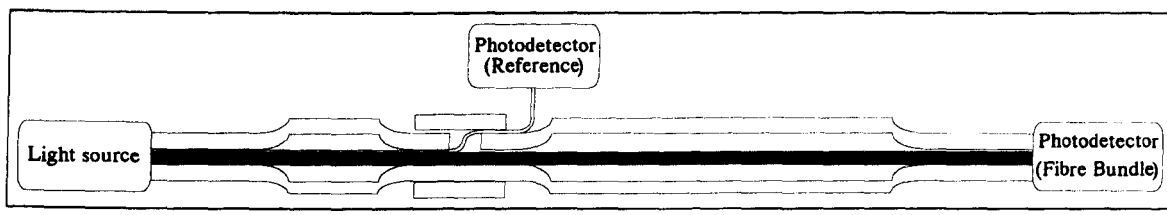

Figure 4.7. Test specimen design for use in the determination of the inherent light guiding ability of the reinforcing fibres.

The specimen used heat shrinkable tubing (HST) to encase the fibre bundle. The HST was shrunk at both ends, entrapping the fibre bundle and allowing it to be connected to a light source and photodetector. This was achieved using SMA fibre-optic connectors, which had been suitably modified to accommodate the HST within the ferrule. The shrunk length at each end of the specimen was approximately 2 cm. A cut was introduced into the HST 4 cm from the light source, allowing a conventional multimode optical fibre to be introduced. This enabled a reference signal to be used to

monitor the variation in intensity of the light source. The area around the cut was supported using a larger section of HST. Total shrunk length of the HST was kept below 6 cm, to minimise contact between the fibre and the HST. During testing, the total shrunk length of HST remained constant and, thus, losses caused by contact between the fibres and the HST could be ignored. The end of the sample into which light was launched, was not disturbed once positioned, ensuring that launching losses were constant throughout the experiment and could also be ignored. The tension on the sample at the launch end was maintained by clamping the sample at the point from which the reference optical fibre emerged.

Testing of the RFLG's was carried out by connecting the launch end of each sample to a white light source and the exit end and reference fibre to photodetectors. The light intensities measured on each photodetector were recorded. The exit end of the sample was then disconnected from the photodetector and a further 1 cm of the HST was shrunk. Once the HST had cooled, 1 cm was cut from the end of the sample and it was reconnected to the photodetector. The light intensities from both photodetectors were then recorded again. The process was repeated until the total length of RFLG remaining dropped to 20 cm, at which point it became very difficult to handle the sample without disturbing the reference fibre, or the launch end.

To remove any effect of changes in the intensity of the light source, each measured value of intensity through the

RFLG was divided by its corresponding reference signal. This normalised the intensity to variations of transmitted light. The data was then plotted and curves fitted to establish the loss rate in the light guides.

The cutback data was expected to follow an exponential scale, as the loss was expected to be a fixed percentage of the light entering a given length of RFLG. Hence, recorded data was plotted and an exponential curve was fitted to the data. The equation that was fitted took the form:

$$Y=a*EXP(b*X) \qquad 4.1$$

The variable b was of interest for the purposes of this study, as this defined the shape of the exponential, or in this instance the proportion of light lost per centimetre. This was converted to percentage of light lost per cm by multiplying b by 100.

Testing was carried out on fibres with the surface conditions shown below:

i). Type 1 fibre bundles in the as-received condition

ii). Type 2 fibre bundles in the as-received condition

iii). Type 2 fibre bundles coated while in the as-received condition

iv). Type 1 fibre bundles cleaned

v). Type 2 fibre bundles cleaned

vi). Type 1 fibre bundles cleaned and coated to produce an RFLG

vii). Type 2 fibre bundles cleaned and coated to produce an RFLG.

A minimum of 5 samples of each type were tested, and the results were statistically analysed to establish 95% confidence intervals of the mean. The statistical method used was the student t-test, as the sample size was small.

4.3.2. Results and Discussion

A typical cutback curve is shown in figure 4.8, along with the calculated best fit curve. The results of cutback testing for each sample type are shown in table 4.3.

Condition	Test 1	Test 2	Test 3	Test 4	Test 5	Test 6	Test 7
ii	92.1	21.6	16.7	74.8	21.4	114.0	46.5
iii	32.0	18.9	23.3	19.0	27.7	37.3	---
iv	9.4	10.5	15.1	7.0	10.5	---	---
v	6.2	6.8	4.6	5.2	5.5	---	---
vi	23.7	23.1	24.5	33.8	23.6	---	---
vii	23.0	15.4	21.3	14.0	15.4	---	---

Table 4.3. Table of results for the transmission characterisation of the fibre bundles and light-guides.

No data is presented for condition i as the fibres did not guide light well enough for a measurement to be made.

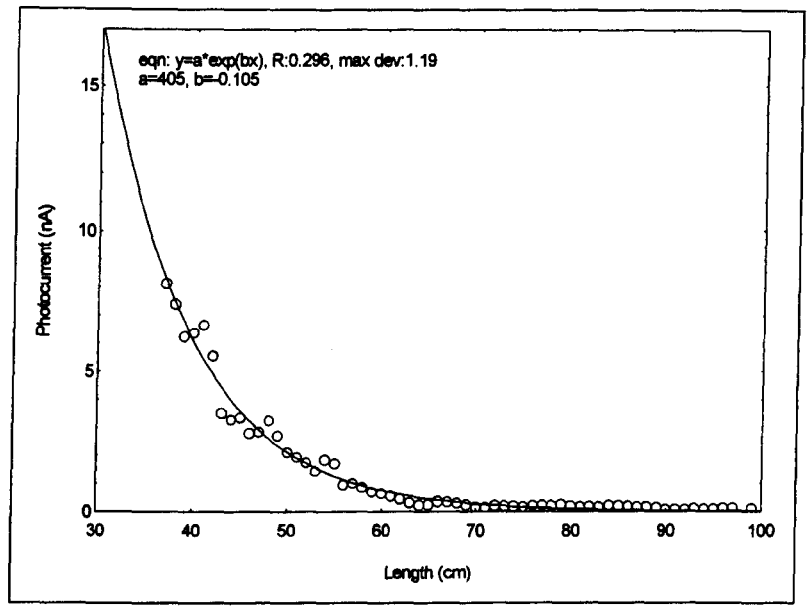

Figure 4.8. Typical results from cutback testing of a fibre bundle. This example shows a fibre bundle that has been cleaned but not coated.

In order to compare the values for each sample type shown in table 4.3, 95% confidence intervals for the position of the mean values were calculated. This was carried out in the manner of a confidence interval, using equations 4.2 to 4.4.

$$\overline{x} \pm t_v \frac{s}{\sqrt{n}} \qquad 4.2$$

where $\overline{x}$ is the mean of the data for each test method, n is the number of observations, s is the standard deviation and t_v is the value observed from the table. The correct value of v for the table observation is calculated from

$$v = n - 1 \qquad 4.3$$

The standard deviation can then be calculated using equation 4.4.

$$S = \sqrt{\frac{\sum x^2}{n} - \left(\frac{\sum x}{n}\right)^2} \qquad 4.4$$

Table 4.4 shows the mean value from each sample type and the calculated mean variance.

Condition	Mean value	Mean variance
ii	55.3	(28.9 81.7)
iii	26.4	(20.8 31.9)
iv	10.5	(8.0 13.0)
v	5.7	(4.9 6.4)
vi	25.8	(21.9 29.6)
vii	17.9	(14.4 21.3)

Table 4.4. 95% confidence interval of the mean for each type of fibre bundle and RFLG.

This data is represented graphically in figure 4.9.

It can be seen from the results in table 4.4 and the graph in figure 4.9, that type 2 fibres bundles in the as-received condition were very variable in their performance. This was to be expected as no attempt had been made to clean the fibres. Once coated, their performance was found to be less variable, suggesting that the coating process had affected the surface contamination.

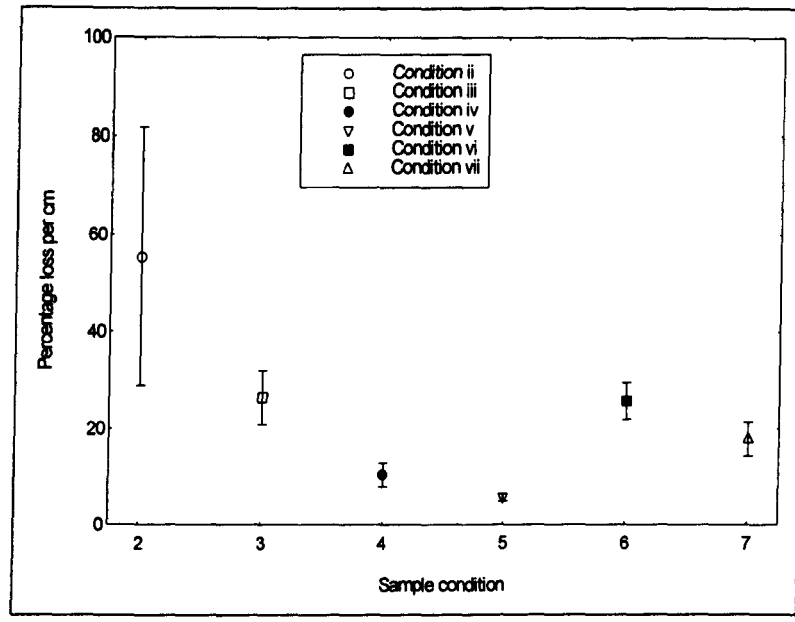

Figure 4.9. Results from the cutback testing of the uncoated fibre bundles and the RFLG's.

After cleaning, the performance of both types of fibre bundles was significantly improved, with the type 2 fibres being better than the type 1 fibres. This can be explained by the small amount of twist applied to the type 1 fibres during manufacture, which was not present in the type 2 fibres. This will lead to increased bending losses in the type 1 fibres.

After coating, RFLG's produced using both types of fibre bundle guided less well than when merely cleaned. However, RFLG's produced from the type 2 fibres were still better than the type 1 fibres. The reason for the increase in the loss upon coating, will be examined in chapter 5.

4.4. Summary

The optimum method of coating the fibres have been determined, in order to maximise their light-guiding characteristics once embedded. Significant faults in the coating process were identified allowing them to be avoided. The quality of the applied coating was studied to enable its uniformity to be determined.

Having applied the coating successfully, the transmission characteristics of the fibres were measured. This included the determination of the level of loss experienced for a variety of fibre conditions.

Chapter 5. Results 3: Loss Mechanisms Associated with the Reinforcing Fibre Light-Guide

This chapter examines the mechanisms by which light can be lost from the RFLG. A number of these loss mechanisms are dependent on the raw materials and, while considered, they will not be numerically modelled as the factors affecting these are production related and, thus, beyond the limits of control available in this study. Areas such as bending and evanescent coupling are considered numerically, as these will significantly affect the performance of the embedded RFLG.

5.1. Rationale

The rationale behind this chapter is that the fibres were clearly seen to lose light when connected to a light source. Figure 5.1 was taken using a bundle of fibres mounted on the viewing platform of a microscope and connected to a white-light source. The light source was carefully shrouded to prevent stray light affecting the quality of the image. The only light used for this photograph was that which emanated from the fibres. It can be seen that there is a steady loss throughout the bundle, seen as a background glow making all of the fibres visible; a large number of bright points of light can also be seen. It would, thus, seem that

the light is lost from the fibres by more than one mechanism.

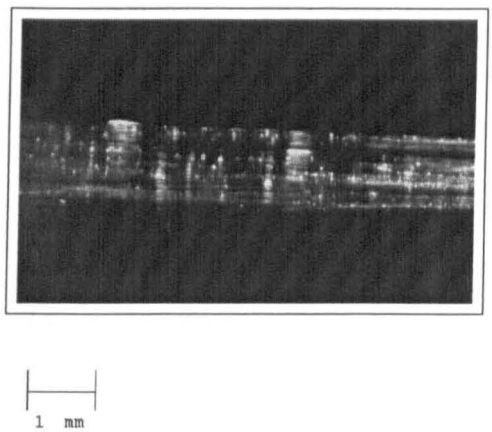

Figure 5.1. Photograph of a fibre bundle guiding light, showing loss of light in two distinct ways: a). As distinct points of light; b). As a steady loss right across the fibres.

Methods by which the light can be lost are presented in the following sections, accounting for both of the loss types observed in the specimen. One loss mechanism which is not discussed is the possibility of a completely broken fibre. This would clearly lead to a total loss of light at the break point, giving a bright spot on the photograph. Clearly in a bundle of fibres, some breaks are likely to exist, however, no way of establishing the exact number could be found. It should also be noted that no broken fibres were seen in the examined specimens, despite the fact that a large number of bright spots were observed. Broken fibres are not totally discounted as a loss mechanism, indeed they will be discussed in chapter 7, as they form the basis for the operation of the RFLG as a damage detection sensor.

5.2. Bending losses associated with the nature of the RFLG

During manufacture, the fibres were drawn from the molten glass, gathered together into a tight bundle and wound on to a drum. The fibres will be approximately aligned, although they will tend to twist around each other and a significant amount of bending will be observed (see figure 5.2). While the angular offset is low, it can be easily seen.

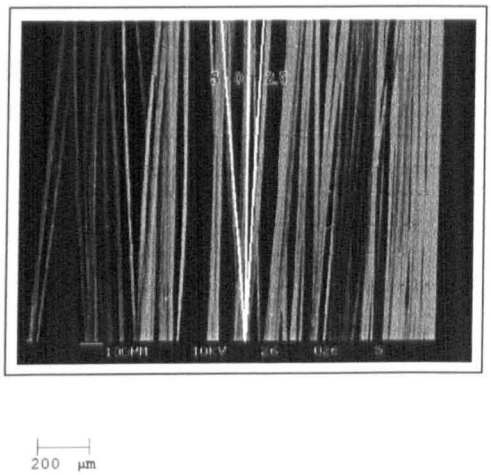

Figure 5.2. SEM image of the fibre bundle showing the angular spread in the fibres. Lines with an offset of 0, 2.5 and 5 degrees have also been superimposed to show the level of disarray in the fibre bundle.

In order to model the bending and establish possible radii of curvature caused by this interaction between fibres, certain assumptions were required. Firstly, only two fibres were considered. It was assumed that one of these fibres crossed the other fibre at a clearly defined angle and that it deformed around the other fibre to form an arc of a circle. It was assumed that the other fibre was totally

undeformed by this process. The geometry of the situation is shown in figure 5.3.

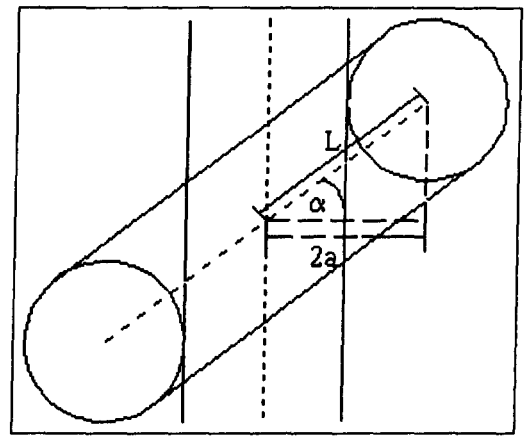

Figure 5.3. Showing the geometrical calculation of the interaction length of the bent fibre.

It can be seen that the length over which interaction takes place can be simply calculated using trigonometry to give

$$L = 2a/\cos \alpha \qquad 5.1$$

where a is the radius of the fibre and α is the angle of interaction between the two fibres. Having calculated the length of interaction, the radius of curvature (ROC) was calculated using the geometric construction shown in figure 5.4. It can be seen that the ROC is then calculated using the expression:

$$R^2 = L^2 + (R-a)^2 \qquad 5.2$$

Expanding this gives:

$$R = (L^2 + a^2)/2a \qquad 5.3$$

where R is the ROC.

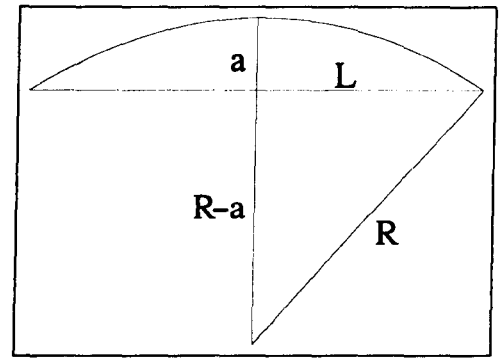

Figure 5.4. Geometrical construction used to calculate the radius of curvature of the deformed fibre.

Having calculated the ROC, the losses associated with the bend were considered. A number of authors (Gloge (1972), Synder and Mitchell (1973) (1974), Love and Winckler (1978), Bader et al. (1989), Bader et al. (1991), Bader and Maclean (1991)) have developed models which consider the losses associated with circular bends in an optical fibre. In the case of the RFLG, a multi-mode optical fibre would be produced and, thus, that by Bader and Maclean (1991) was adopted as most of the others considered single-mode fibres. In this approach, the losses were calculated using ray-tracing techniques, to model the paths of rays around the bend. Having calculated the loss for each ray, the losses were combined to give an overall value of the power output as a proportion of the power input.

To achieve this it was first assumed that each ray possessed unit power, at the point of entry to the curved section of the fibre. Another assumption of the model was that the

fibre possessed an infinite cladding, meaning that no light could re-enter the core of the fibre after reflection at the cladding/air boundary. In order to model the situation mathematically, the geometry of the situation and nomenclature used, are shown in figure 5.5.

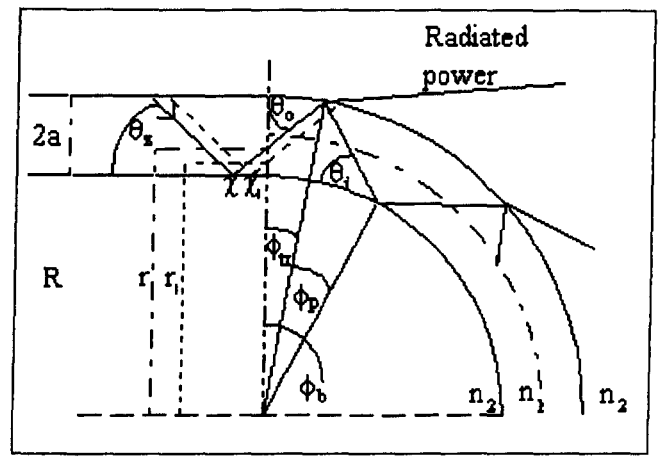

Figure 5.5. Schematic illustration of the geometry of the waveguide and an entering ray.

To calculate the number of mode groups transmitted through the fibre, Bader and Maclean (1991) gave the formula:

$$\sin \theta_z = p*\pi/(2*n_1*k*a) \qquad 5.4$$

where n_1 is the refractive index of the core material, k is $2\pi/\lambda$ (λ being the wavelength of light) and p is the number of the mode group currently under consideration. The term p is an integer and is calculated such that:

$$p_{max} * \theta_{z(p=1)} < \theta_c \qquad 5.5$$

The term p_{max} is the number of modes carried in the fibre. θ_c is defined as the critical angle for guiding to occur and can be calculated using equation 5.6.

$$\cos \theta_c = n_2 / n_1 \qquad 5.6$$

where n_2 is the refractive index of the cladding. However, equation 5.5 was derived assuming that $\sin \theta = \theta$, which is an approximation only valid at small values of θ. In conventional optical fibres the difference in refractive indices will be very low, making the assumption valid. However, in this study, the chosen cladding materials gave a large difference, making the assumption invalid. A method was therefore required to overcome it.

In effect what equation 5.5 says is that θ_z at $p=p_{max}$ must be less than θ_c and, hence, equation 5.4 can be rewritten as:

$$\sin \theta_c > p_{max} \pi/(2*n_1*k*a) \qquad 5.7a$$

and, substituting for k

$$\sin \theta_c > p_{max} \lambda/(4*n_1*a) \qquad 5.7b$$

Equation 5.7b then allows the integer p_{max} to be calculated, enabling θ_z for each integer value of p to be calculated using equation 5.4.

The angles θ_o and θ_i, marked in figure 5.5, will vary for each modal group, depending on the precise location of χ (see figure 5.5). To take account of this spread, a number of rays were considered in each modal grouping. This was done by moving χ to different, fixed, positions, for example χ_1, thus varying r to r_1. For this study, rays were considered every 0.5 μm through the core, but not impinging on the walls on entry into the curved section. Thus, 17 rays were considered per mode group, equally spaced through the core. The number of rays considered for each modal grouping, multiplied by the number of mode groups, p_{max}, gives the total number of rays and was termed S.

To calculate the losses associated with the introduction of a bend, Bader and Maclean (1991) established the values of θ_o and θ_i. The formulae used are shown in equations 5.8a and 5.8b respectively:

$$\cos \theta_o = (r \cos \theta_z)/(R+a) \qquad 5.8a$$

$$\cos \theta_i = (r \cos \theta_z)/(R-a) \qquad 5.8b$$

These angles were calculated for each value of θ_z and each value of r, to give the two angles of intersection for each ray under consideration. It should be noted, however, that θ_i can cease to exist at certain geometries. This is because the ray will reflect from the outer wall at a large angle such that it does not hit the inner wall, but continues its path only interacting with the outer wall. Thus, if

equation 5.8b gives an impossible answer, θ_i can be taken to be zero.

Using equations 5.8a and 5.8b, ϕ_{tr} can be calculated from:

$$\phi_{tr}=(\theta_o-\theta_i)= \cos^{-1}((r \cos \theta_z)/(R+a))-\theta_z \qquad 5.9$$

and ϕ_p can be calculated from:

$$\phi_p=2(\theta_o-\theta_i) \qquad 5.10$$

The geometry of the curve is such that θ_i is smaller than θ_z. Hence, if the ray is guided without loss in the straight fibre, it will not experience loss at the inner surface of the curved fibre. However, θ_o is always greater than θ_z with the result that both tunnelling and refraction can occur. These will both lead to loss of light power in the core of the fibre. So called leaky rays can exist when θ_o is less than θ_c; more power is lost from the ray as θ_o approaches θ_c. When θ_o is greater than θ_c, light rays are refracted out of the core and all of the power in the ray is lost. When leaky rays are present, the power is lost progressively, as more interactions with the outer surface occur. Thus, the number of reflections from this outer surface must be known. Firstly ϕ_b is defined as the angle of travel around the circlular arc. This must be greater than or equal to ϕ_{tr}. The number of reflections, N, is then calculated from:

$$N = ((\phi_b - \phi_{tr})/\phi_p) + 1 \qquad 5.11$$

where N is an integer.

The power remaining in the core, as a proportion of the light entering the core, $P(\phi_b)/P(0)$, at an angle ϕ_b around the circle is then:

$$P(\phi_b)/P(0) = \frac{1}{S}\sum_{S=1}^{S}(1-T)^N \qquad 5.12$$

where S is the total number of rays and T is the generalised Fresnel transmission function (Synder and Mitchell (1973)), calculated from:

$$T(\theta_o) = 4\{1-(\theta_o/\theta_d)^2\}^{1/2} * \mathrm{Exp}\{-2/3jR(\theta_d^2-\theta_o^2)^{3/2}\} \qquad 5.13$$

for cases where $\theta_o<\theta_d$, where θ_d is the complement of the critical angle, as defined in equation 5.6, and $j=2\pi n_1/\lambda$. Thus, using equations 5.12 and 5.13, the power output can be calculated for any ROC.

For the purposes of this study, to maintain compatibility with the loss measurements made in chapter 4, the loss was calculated over the length of 1 cm. Thus ϕ_b was calculated for each radius of curvature, to correspond to a total bent length of 1 cm. This assumes that the whole of the fibre is uniformly bent into a circular path, which is obviously not the case. However, the results will be an indication of a worst case scenario, with the true losses being lower than those calculated here. Calculations were carried out for a

cleaned fibre and also one which was coated with Sylgard 184. This was done to discover if the application of a coating could account for the increased losses observed in the coated fibre bundles, compared to those without a coating (see chapter 4).

The graph shown in figure 5.6 presents the power output from both a clad and unclad fibre with varying angular offsets between the two interacting fibres. This was calculated using equation 5.12 for each angular offset. The refractive indices used in the calculation were 1.4585 for the fibre, 1.41 for the silicone cladding and 1 for the air cladding It can be seen that the coated fibre would lose light much more rapidly than the uncoated one. This is due to the change of critical angle to a much lower value in the case of the coated fibres. It is, therefore, easier for a higher percentage of the total guided rays to either leak or be refracted from the fibre core. This provides a possible explanation for increased loss in the coated fibres.

The predicted loss in the uncoated fibre is lower than was observed. However, this model takes no account of surface contamination and damage to the fibres. The losses predicted for the silicone-coated fibre is higher than those experienced in the cutback test, for the fibre angular offsets seen to be prevalent in the fibre bundles. Here the assumptions made in the calculations account for this. The fibres within the bundle will be bent around a variety of curves with different ROC. It was assumed, however, that they would only be bent around one ROC, for the full 1 cm

length. In reality, some regions will have a large ROC and will, thus, give little or no loss, while others will be more curved and give a high loss.

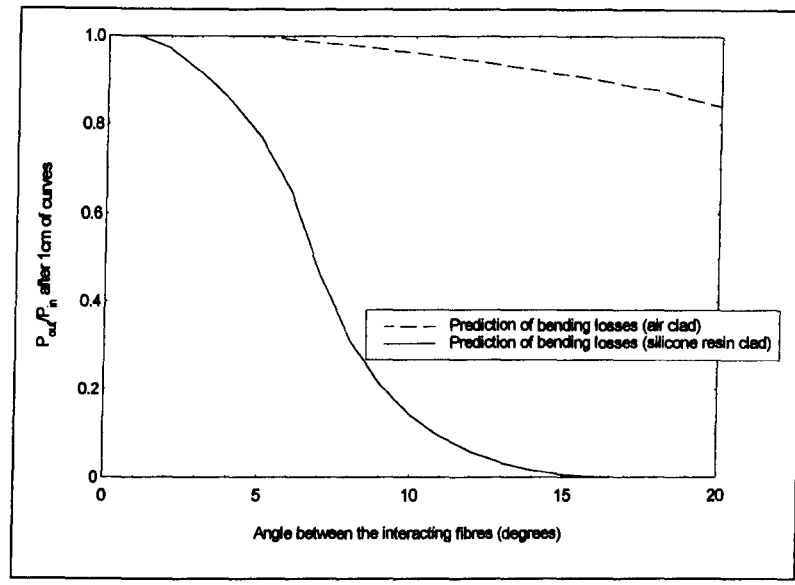

Figure 5.6. Graph showing the predicted losses due to bending in silicone and air clad fibres.

Within this model, no allowance has been made for the entry of light from one guiding core into another. With the multiplicity of guiding cores this is a possible interaction and may help to account for the predicted losses being higher than those observed. The loss will change if light couples from one core to another, as the model monitors the effect of curvature on a given number of rays with unit power. The coupling of light into a core will either change the number of rays, or the power in a ray. This will obviously affect the losses in the fibre and invalidate the model assumptions. Also, it was assumed that lost light was permenantly lost to the system. If light transfers from one

core to another, then this assumption is invalid and the overall loss will be reduced.

The effect of bending on the losses is firmly established for optical fibres and will account for a significant part of the losses from the RFLG. This mechanism of loss will add to the continuous background losses in the photograph shown in figure 5.1.

5.3. Evanescent losses from the RFLG after embedding

5.3.1. Experimental

Within an optical fibre, at the interface between the core and the cladding material, the light is reflected when guiding occurs. However, the reflection does not take place precisely at the interface, with the energy penetrating slightly into the cladding material. This penetration is refered to as the evanescent field. The evanescent field falls off exponentially, so the bulk of the energy is reflected at or very close to the interface, although some will penetrate to a significant depth into the cladding. An absorbing body within range of this energy penetration, will lead to loss of light from the core. The depth of energy penetration into a flat plate can be calculated using equation 5.14 (Harrick 1967).

$$DP=\lambda/(2*\pi*n_1*(\sin^2\theta-(n_2/n_1)^2)^{1/2} \qquad 5.14$$

where DP is the depth at which the energy has dropped to 37% (This being 1/e) of its original value. The other symbols take the following meanings: λ is the wavelength of light under consideration, n_1 is the refractive index of the core, n_2 is the refractive index of the cladding and θ is the angle between the ray and a line perpendicular to the direction of the fibre.

Evanescent losses will occur in the RFLG if fibres within it come into close contact with the matrix resin of the composite. This is due to the fact that the matrix resin has a refractive index greater than that of the fibres and will, therefore, not satisfy the requirements for guiding. Hence, any light energy penetrating as far as the matrix resin will be lost to the RFLG.

In order to examine the effect of these evanescent losses on the RFLG, six were prepared in the same way as those which were to be embedded. These were then placed within tubes of the shape shown in figure 5.7, a photodetector being attached to one end and a white-light source to the other. The third arm of the tube allowed bromonapthalene to be introduced, covering the light-guide 1 cm at a time. Bromonapthalene has a refractive index of 1.64 which was significantly higher than that of the glass fibres and would, thus, mimic the matrix resin of the composite. A reading of the transmitted light intensity was taken for each successive submersion length, the process being repeated for all of the RFLG's, using a clean tube for each

test, preventing contamination of the sample prior to testing.

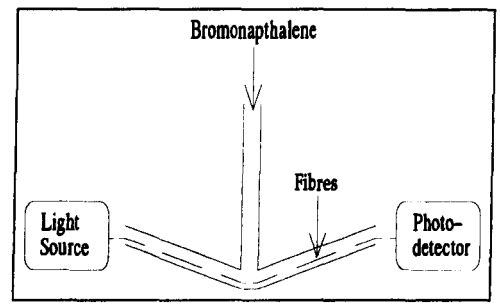

Figure 5.7. Schematic illustration of the experimental setup used to measure the effect of embedding on the guiding characteristics.

5.3.2. Results and discussion

5.3.2.1. Results

The results of the progressive submersion of the RFLG's in bromonapthalene are shown in figure 5.8. Each of the sample fibres were produced in the same way and were nominally identical. It can be seen that there is some variance between the results for each fibre due to the variation in coating quality observed in chapter 4. However, fitting exponential curves to the results showed that there was only a variance of between 6 and 13.5 %/cm of transmitted light. A solid line is superimposed on the data which shows the predicted extent of the loss. This was claculated using the model which will be developed in the following section. This figure will therefore be discussed in more detail later in the chapter.

5.3.2.2. Modelling light loss within the RFLG

In order to model the losses, the following assumptions were made:

i) the fibres within the bundle lie straight, and thus fibres within the bundle that are close to the matrix resin remain there

ii) there is no transfer of light between the guiding cores during transmission

iii) the coating is uniform, with thin regions remaining uniformly thin

iv) the amount of light energy which penetrates to the absorbing medium is lost to the system.

Examining equation 5.14, it can be seen that the depth of penetration depends on the angle of approach of the ray to the fibre wall. This was calculated using equations 5.4 to 5.7b for each of the bound modal groupings. The depth of penetration of each modal group was then calculated for a wavelength of 550 nm (roughly the middle of the visible spectrum), with n_1 and n_2 being taken as 1.4585 and 1.41 respectively.

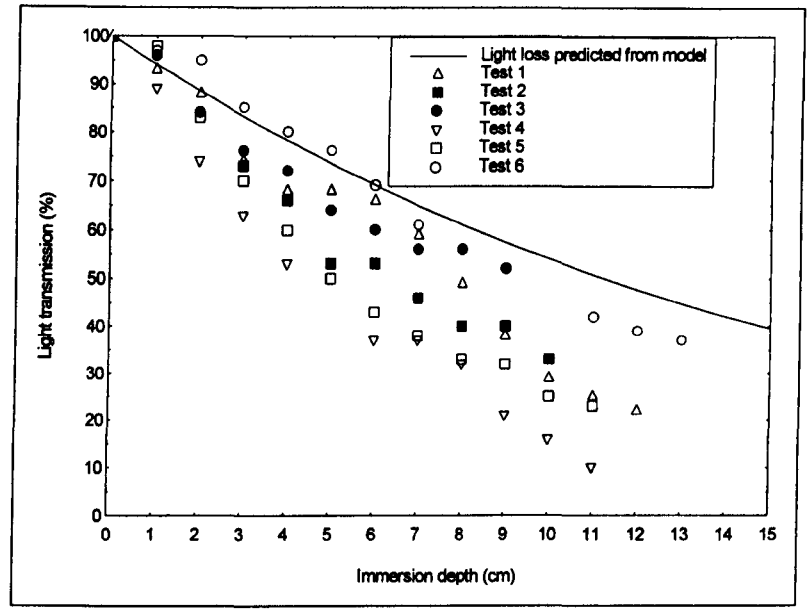

Figure 5.8. Graph of experimental results for the progressive submersion of RFLG's in bromonapthalene. The predicted loss from the model is also shown.

For the purposes of the model, a situation was considered where a single reinforcing fibre rested in a layer of coating such that at its thinnest point the coating was 100 nm thick. The assumed situation is shown in figure 5.9, along with the penetrating energy decay curves.

To calculate the fall in the penetrating energy, a loss curve was fitted through two known points, these being zero depth with 100% of energy remaining and DP depth with 37% of energy remaining

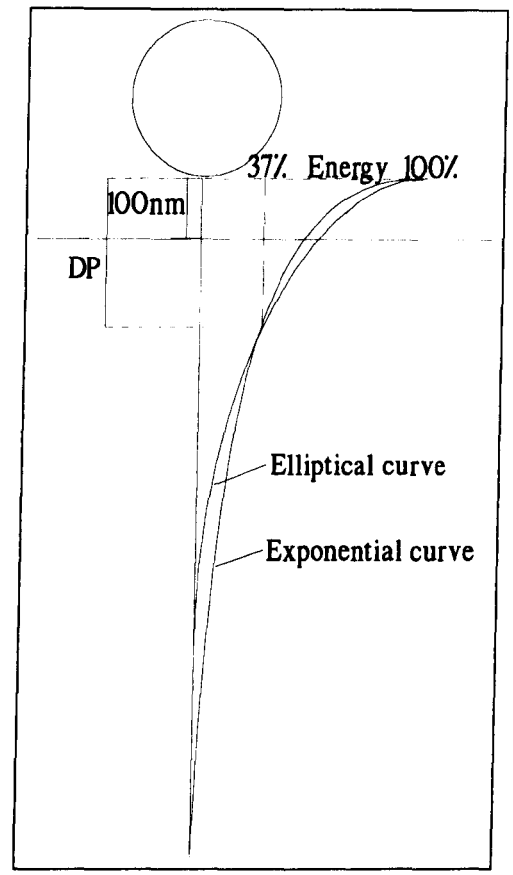

Fibre 5.9. Schematic illustration of the assumed arrangement of the fibre and cladding. The penetration of light energy into the cladding is also superimposed.

This data provided two coordinate points on the curve, allowing a model curve to be fitted. It was assumed that the fall off in energy was elliptical, not exponential, as it was possible to fit an elliptical curve to the two known fixed points. It was not possible to carry out similar curve fitting for an exponential curve, because too few points were known. The equation was calculated using the generic equation for an ellipse, centred at the origin, which is shown in equation 5.15

$$\frac{x^2}{a^2} + \frac{y^2}{b^2} = 1 \qquad 5.15$$

where x and y are general points on the axes, a is the intersection with the X-axis and b is the intersection with the Y-axis. The value of a was known to be 100%; b could then be calculated by letting the value of x be 37% and y be DP. From the obtained values of a and b, it was possible to calculate the amount of energy penetrating through the cladding material, for any thickness of cladding, for each modal group.

Considering rays propagating in the fibre, the rays will be distributed radially about the centre of the fibre. The amount of energy lost will vary around the fibre, with losses occuring only in the bottom half (see figure 5.10). The energy lost per modal group per reflection from the fibre's bottom surface can then be calculated in the following manner.

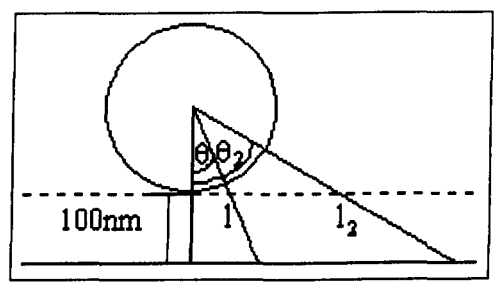

Figure 5.10. Schematic illustration showing the area over which light energy will be lost to the system.

The depth of penetration required to reach the absorbing medium was first calculated using the construction shown in figure 5.10 and equation 5.16.

$$\cos \theta = (a+100)/(a+l) \qquad 5.16$$

where θ is the angle around the fibre section, a is the fibre radius and l is the depth of penetration to the absorbing medium. Using the elliptical curves, which had been fitted to each modal grouping, the energy loss for each value of θ was calculated for each modal group.

The number of reflections from the lower surface of the fibre was then calculated for each modal group using equations 5.17 and 5.18.

The distance between successive reflections was first calculated using equation 5.17.

$$L = 2a/\tan \theta_z \qquad 5.17$$

where L is the distance between consecutive reflections at the top and bottom of the fibre, θ_z is the modal angle and a is the fibre radius. The number of reflections per centimetre on the bottom of the fibre was then calculated using equation 5.18.

$$NR = 1/2L \qquad 5.18$$

where NR is the number of reflections and L must have the units of centimetres.

Having calculated the number of reflections per centimetre for each modal group, the cumulative loss per modal group per centimetre was calculated. Initial power in each mode was taken as 100, with the fixed loss per reflection, calculated previously, being applied for each reflection. The calculated values are shown in table 5.1. The effective loss in the fibre as a whole, per centimetre, was calculated by averaging the losses in each mode, over the whole fibre. This was calculated to be around 36 %/cm per fibre.

Mode number	Percent lost per centimetre
1	28.9
2	28.9
3	30.0
4	30.0
5	31.1
6	32.2
7	33.3
8	35.6
9	37.8
10	43.3
11	64.4

Table 5.1. Percentage loss per centimetre for each modal grouping within the fibre core.

Once the loss in an isolated fibre had been determined, the situation for a RFLG was considered. In order to consider the actual losses in an RFLG, the average number of fibres which were close to the matrix resin was determined. Ten separate embedded RFLG's were examined using optical microscopy, to determine the number of reinforcing fibres in close proximity to the matrix resin. The results of this

study indicated that on average 33 fibres were close to the resin and would be expected to lose 36 % of their light energy. However, there were 200 fibres in the bundle. Assuming that each fibre carried an equal proportion of the initial light, the amount of light lost per fibre bundle was calculated to be around 6 %/cm. This value is similar to the observed values from the experiments, as shown in figure 5.8.

The assumption that the fall off in light energy was elliptical, as opposed to exponential, would lead to inaccuracies in the determination of the energy loss. Prior to the intersection point at 37 % (See section 5.3.1), the elliptical curve fit will tend to overestimate the energy lost, whereas after the intersection, it will tend to underestimate it (see figure 5.9). However, the number of known points on the curve precluded the fitting of an exponential curve.

The assumption that the fibres were straight and would stay spacially constant with respect to each other along the bundle length is also incorrect, as was discussed in section 5.2. This would lead to error in the prediction of energy loss, as new fibres could come into contact with the absorbing layer, leading to a spreading of the loss through more than the initial fibres. As the loss removes a fixed proportion of the light in the fibre, the largest amount is lost at the first reflection. Hence, this assumption will lead to an underestimation of the light loss.

The assumption that no energy transfer takes place between fibre cores is also an over-simplification. Just as light can transfer energy, via the evanescent field, into an absorbing body, so it can also transfer energy into a guiding body in its vicinity. As the fibres in the bundle are closely spaced, there is the possibility of transfering light energy between fibres which have experienced no loss and those that have lost light. This would lead to the model, as proposed, being inaccurate. A fibre that lost light after energy transfer, would lose a different amount from that which would be predicted if no transfer had occured.

The assumption that the coating is uniformly thick is also an over simplification, as the coating will vary randomly. In some areas the fibres will all be well coated and in others, more will be exposed than was assumed (discussed in greater depth in chapter 4). The geometry of the bundle means that it is more likely that substancially less fibres would be close to the resin than that more of the fibres would be close to it. This is because the bundle tends to exist as a clump, which will have a relatively constant circumference, meaning that only a given number of fibres can exist at the edge of the clump in a thinly coated region. Conversely, where a thick region exists, it will tend to surround the whole, or part, of the clump reducing the number of fibres in contact with the resin, in that region. In this manner a reduction in loss is more likely than an increase in loss, leading the model to overestimate.

The assumption that the layer of Sylgard 184 passes the fibre in a flat plane, will also lead to an inaccuracy. In fact it is observed in many of the RFLG's that at least one fibre will be close to the resin on more than one side. This will clearly lead to an underestimation of the losses, as the percentage of energy lost will be much higher in such a fibre than it would be if only one side of the fibre lost light.

From the above discussion it can be seen that the assumptions can lead to both over- and under-estimates being made of the total loss due to evanescent coupling. However, the effect of these losses on the RFLG has been demonstrated. It is suggested that evanescent losses will account for the vast majority of the excess loss observed in the embedded RFLG over and above those observed in the unembedded RFLG.

5.4. Scattering and absorption of light

Scattering of light, is another mechanism by which light could be lost to the core of a reinforcing fibre. The most likely form of scattering in this case, is due to impurities or irregularities. The presence of impurities within the fibre core could lead to localised changes in refractive index, leading to refraction of the light and possibly its loss from the core altogether. Blemishes on the fibre surface could also lead to scattering. These loss mechanisms should be minimised, to maximise guiding

characteristics, although with high purity silica fibres impurities should be low and, thus, the effect of refractive index changes on scattering should be minimal.

Scattering from inclusions in the core glass may, however, have a significant contribution in the case of these fibres. It was observed that the raw glass, from which the fibres were drawn, contained a significant amount of voids (section 3.1). If light were to strike one of these voids, it would have the effect of a prism in the structure and could increase scattering (see figure 5.11). It can be seen that voids in the fibre core would lead to light being lost at discrete locations, providing a mechanism by which the bright spots in figure 5.1 could be formed.

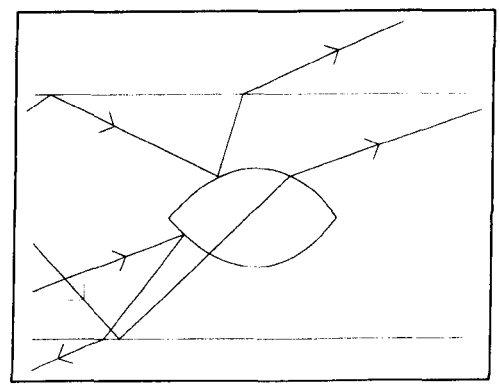

Figure 5.11. Schematic illustration of the scattering effects associated with the presence of voids in the fibre core.

5.5. The effect of voiding within the cladding

Voids were inevitable in the application of the coating, so their effect on the guiding characteristics was important. Two possible situations were considered, these being the presence of a void at the point of light launching into the fibre, and a void encountered in the RFLG structure. Each of these cases is illustrated in figure 5.12.

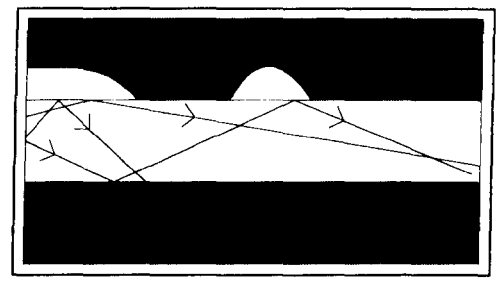

Figure 5.12. Schematic illustration of the effect that voids have on light guiding, both at the end of the fibre and also mid-fibre.

It can be seen from this diagram that the effect of the void at launching is a momentary increase in the critical angle leading to an initial large quantity of modes within the fibre. Once the fibre is surrounded by solid cladding these modes are lost to the fibre and the situation returns to that which would be expected if a void was not present. When a void is encountered in the middle of the fibre, light strikes the core/cladding interface at well below the critical angle for a core in contact with air. Therefore, the light continues to be guided, unaffected by the presence of the void. Thus, voids in the cladding have no significant loss-promoting effect over and above those of a

fully clad fibre and can be neglected from the point of view of this analysis.

5.6. Summary

Due to the observation of light loss from a fibre bundle, a variety of potential loss mechanisms have been discussed. Bending losses, well established in convential optical fibres, have been examined in the context of the RFLG. Evanescent losses from the RFLG, when embedded, have also been examined both numerically and experimentally. Both of these loss mechanisms were found to be capable of giving significant losses in the RFLG. The effect of surface damage and voiding both within the fibre and between fibre and matrix have also been examined. Voiding within the fibre and surface damage were both shown to be potential loss inducing mechanisms.

Chapter 6. Results 4: Examination of damage development in composite containing reinforcing fibre light-guides

This chapter discusses the development of damage within the composite, under impact and crush testing. The level of adhesion between the prospective cladding materials and the composite was also examined. Bearing in mind the adhesion data, the effect that the presence of the RFLG had on damage development was examined.

6.1. Study of the adhesion between the cladding and the matrix resin

6.1.1. Experimental

To provide information on the level of adhesion between the cladding polymers and the composite, a specimen was prepared consisting of a layer of cladding polymer sandwiched between two square pieces of pre-preg 1 cm in length. The sandwich of pre-preg and cladding polymer was then attached between two aluminium strips, previously abraded and degreased with acetone, to form a lap-shear specimen. The edges of the sample were sealed using PTFE tape to prevent the resin flowing out of position, and the sample was cured under slight positive pressure, to ensure intimate contact between the cladding polymer and the matrix resin.

Five samples were prepared using each of the cladding polymers Sylgard 184 and OG 137, as well as samples with no cladding polymer between the pre-preg squares, to give a reference value. Prior to preparation of the composite the silicone resin was fully cured, whereas the OG 137 was applied to the surface of one of the pre-preg squares as a solution and allowed to dry.

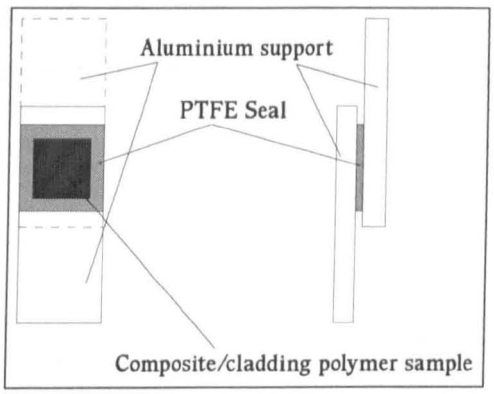

Figure 6.1. Schematic illustration of the samples used to test the interface strength between the cladding polymers and the composite.

Testing was carried out using a Tensometer type 'E' tensile tester at a speed of 0.5 mm/minute, a load/extension curve being plotted as testing proceeded. The fracture surfaces were observed upon failure, to pin-point the locus of failure.

6.1.2. Results and Discussion

The graph shown in figure 6.2 shows a plot of peak load obtained for each of the specimen types, under tensile testing. It is clearly seen that the adhesion between the

Sylgard 184 and the composite is very low, an observation which is verified by examination of the fracture surface. The fracture was observed to be totally interfacial in nature, with no apparent adhesion between the two materials. In the case of OG 137, it is observed that the level of adhesion is much closer than that of the reference samples; again the fracture surface gives evidence to this. It was observed, in this case, that both pieces of pre-preg retained fragments of OG 137. This indicated that failure had occurred in both the OG 137 and the interface at similar levels of load.

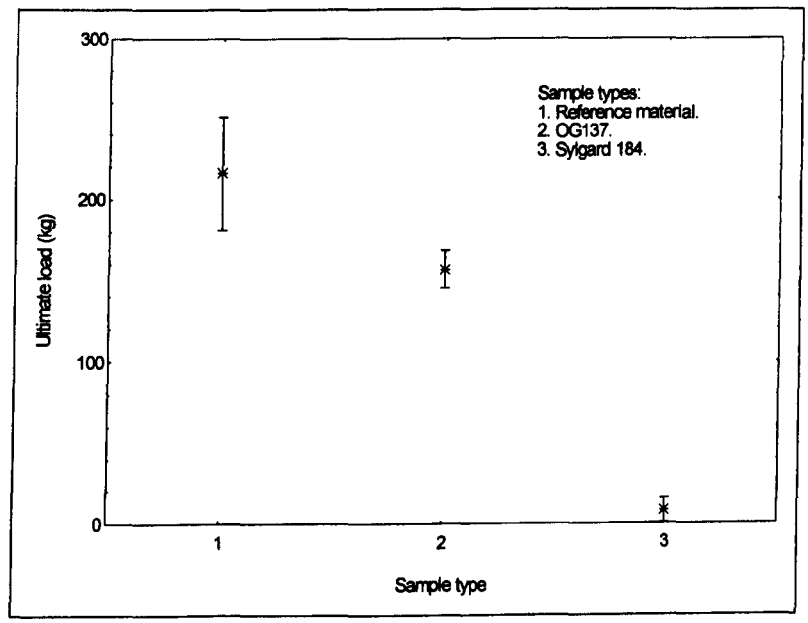

Figure 6.2. Graph showing the results of adhesion testing of the two chosen cladding polymers, with the composite. The strength obtained from reference panels is also shown.

While it can be said that the strength of the OG 137/composite interface approached that of the reference samples, it cannot be said that it approached that of the

composite/composite interface. This is because observation of the failure location in the reference samples showed that failure had occurred in the aluminium/composite interface. This showed that the composite/composite interface was significantly stronger than the reference level measured in the tests.

Although neither interface approaches the strength of the composite itself, it can be seen that the OG 137 has a stronger interface with the composite than Sylgard 184 and, hence, will be less detrimental.

6.2. Preliminary damage sensing study

6.2.1. Experimental

Initial sensing studies were carried out using an RFLG produced from fibre bundles described in section 3.2 as type 1 fibres. These fibres were first cleaned and then coated using the process described as method i in section 4.1.

Composite specimens were prepared using a 16 ply, cross-ply, lay-up sequence of $\{0,90,90,0,0,90,0,90\}_s$. Panels were prepared which contained no optical fibres, RFLG's, 30, 50 and 125 μm conventional optical fibres, to allow comparison of the effect of the various optical fibre types on the induced damage. Fibres were positioned every centimetre between plies 1 and 2 and also between plies 15 and 16, in the 0 direction, in the following manner: in the case of the RFLG and 125 μm optical fibres, a single fibre was placed

every centimetre, in the case of the 50 μm optical fibres a bundle of 6 to 10 fibres were laid every centimetre and in the case of the 30 μm optical fibres a bundle of 200 fibres were laid every centimetre. The panels were then cured in an autoclave and C-scanned, using a sound frequency of 10 MHz, before being cut into 70 mm squares. The specimens were then air dried at 60°C for three days and stored in a desiccator until required for testing.

Impact testing was carried out using five different impact energies, 2, 4, 6, 8 and 10 J, using a Rosand instrumented impact tester, fitted with a 20 mm hemispherical tup. Two samples of each type were impacted at each of 2, 4, 6 and 8 J, with one being impacted at 10 J. Subsequent to impact testing, the specimens were C-scanned to reveal the extent of the damage, and the damaged area was measured for each optical fibre type. The damaged areas were then compared, to reveal any differences between the specimens containing different optical fibre types.

The C-scanner used in this study was only capable of providing a profile image of the damaged region. In order to ascertain the likely location of the damage within the composite, reference composite panels containing no optical fibres, which had been impacted at one of the impact energies used in the study, were taken and mounted in cold-curing mounting resin. Cold-curing resin was chosen, as no heat or pressure had to be applied to the specimen, which would have tended to increase the damage in the already delaminated composite.

Having mounted each panel, it was then sectioned using a diamond wheel, to remove sections within the damaged region. Slices of 1 cm width were cut through the centre of the specimen, and to either side of the specimen. The composite slices were carefully polished to a 1 μm diamond finish, ensuring that all of the deformation introduced during diamond cutting and grinding was removed before progressing to a finer abrasive. A dye penetrant was then applied to the polished surface. The dye penetrant was allowed to soak into any cracks present in the polished surface, before being wiped off after a five minute soak time. The dye used was a fluorescent dye, which fluoresced under the light of a mercury discharge lamp. Using this arrangement, on a Leitz Optimat microscope, the presence and position of cracks could be observed, as the dye penetrant fluoresced with a green light in the crack locations. Photographs of the sections were taken using a 3200 ASA film as the light levels were very low.

6.2.2. Results and Discussion

Typical C-scans from the composite containing RFLG's, at each of the impact energies used in the study, are shown in figure 6.3, along with an unimpacted reference panel.

The vertical lines apparent on the panels containing RFLG's are not delaminations, but are due to the presence of the RFLG's. They appear in this fashion as the sound-wave

transmission characteristics of the silicone resin is significantly different from that of the composite, leading to scattering of the ultrasonic waves. The increase in size of the delamination, as the incident impact energy increases, is clearly seen.

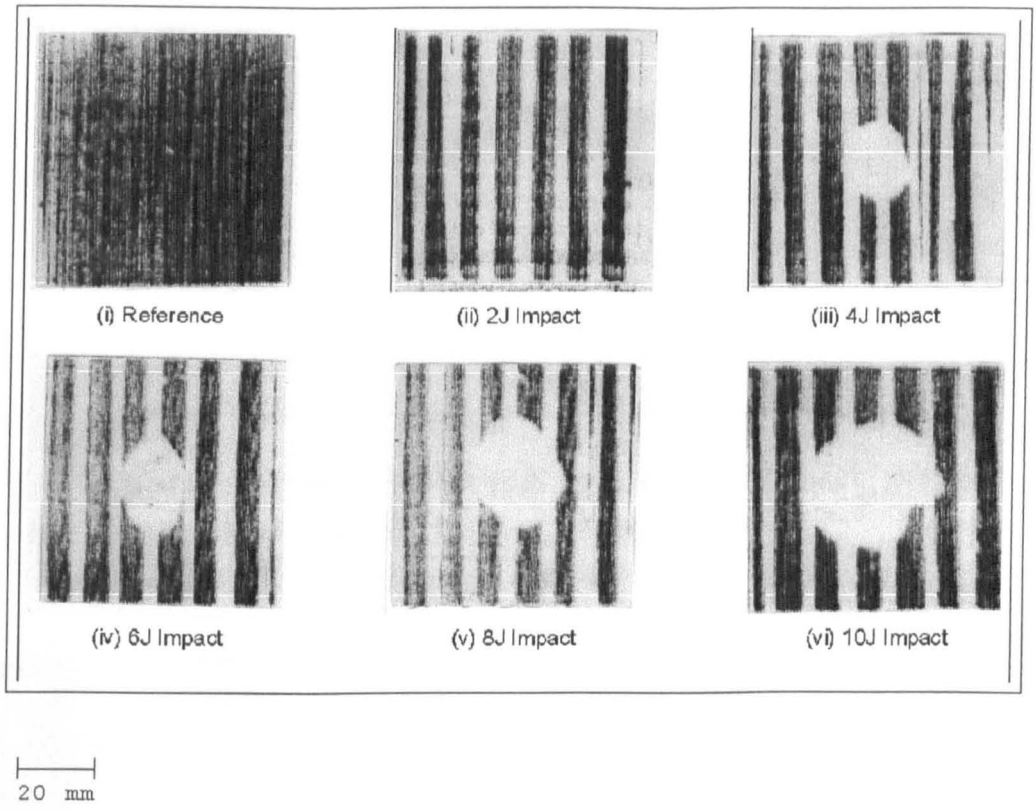

Figure 6.3. C-scan images of an unimpacted reference panel and five composite panels containing RFLG's impacted at increasing impact energies.

Comparison was carried out between the measured delamination areas for each of the optical fibre types used in this study. The results are shown in figure 6.4. It can be seen that there is no significant difference between the measured delamination areas for each of the different optical fibre types. This indicates that despite the poor adhesion

between the RFLG and the composite, they do not appear to have a detrimental effect on the properties of the composite under impact loading.

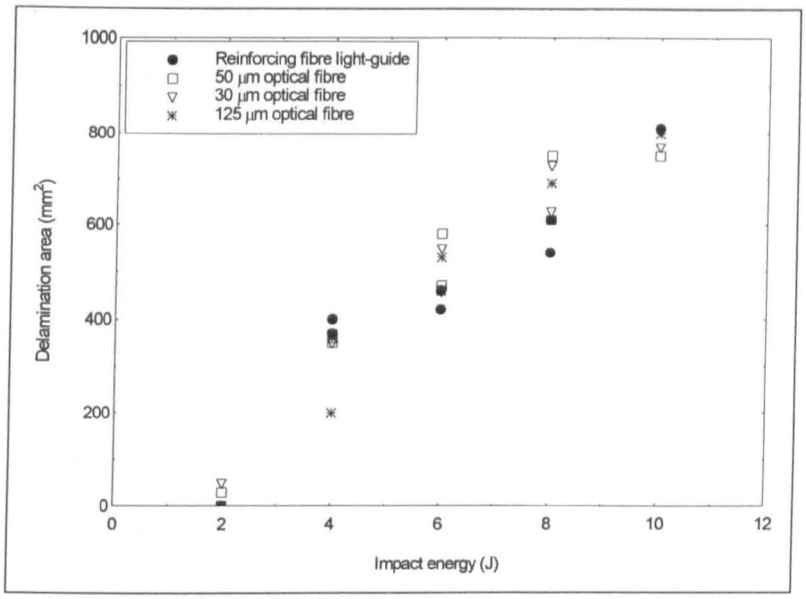

Figure 6.4. Graph of the delamination area against impact energy for the different sample types used in the preliminary study.

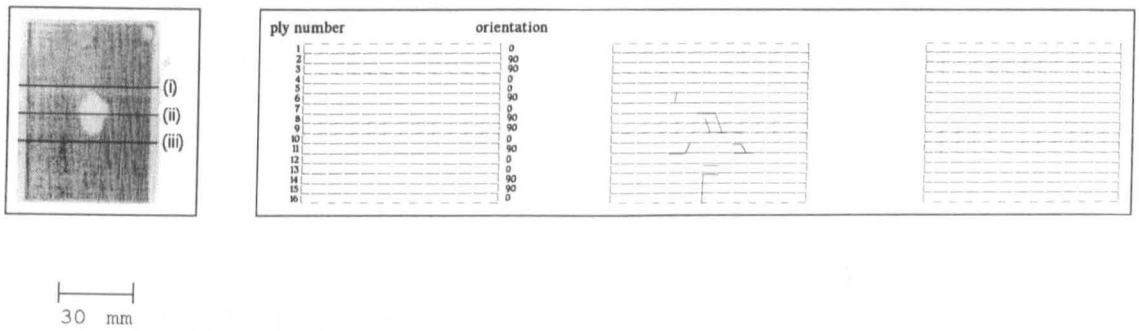

(a) (b) (c) (d)

Figure 6.5. Illustrating the location of damage within a reference panel impacted at 2 J. Sections (b), (c) and (d) show the damage across sections indicated by lines (i), (ii) and (iii) in figure (a), respectively.

The examination of the location of the impact damage, revealed that a 2 J impact gave predominantly transverse

splitting of 90° plies. However, some delamination was observed, shown in figure 6.5. An 8 J impact not only gave splitting through the plies, but significant delamination at 0/90 interfaces. The damage area was also seen to have spread further after the 8 J impact. This is shown in figure 6.6.

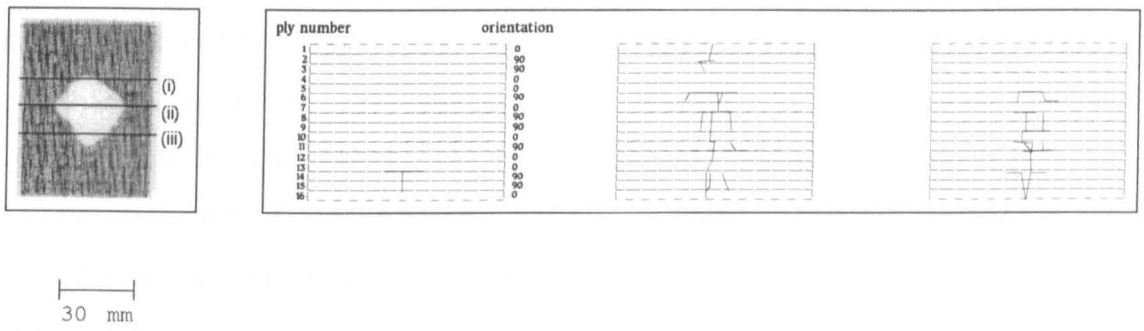

(a) (b) (c) (d)

Figure 6.6. Illustrating the location of damage within a reference panel impacted at 8 J. Sections (b), (c) and (d) show the damage across sections indicated by lines (i), (ii) and (iii) in figure (a), respectively.

6.3. Crush testing

6.3.1. Experimental

Crush testing was carried out on samples of composite containing RFLG's and also composite containing no light-guides, to simulate impact damage in a more controllable fashion. RFLG's were embedded between plies 1

and 2 of a 16 ply composite with the lay-up sequence $\{0,90,90,0,0,90,0,90\}_s$. The RFLG's used in this study were produced using type 2 fibres, with an optimised coating described as method iii in section 4.1. The composite was produced in 200*20 mm strips of approximately 2.5 mm thickness. These were cut to give a specimen of 100*20 mm, for the purposes of crush testing. The geometry of tup and of specimen clamping used for the crush test was the same as that used in the impact study. The setup used was a 20 mm hemispherical tup, the sample being edge clamped and the central portion unsupported. Three RFLG's were embedded within each specimen, with one fibre embedded centrally, one fibre placed 2 mm to one side of the centre and the other placed 4 mm to the other side, allowing damage spread to be monitored.

Prior to testing being carried out, each strip was C-scanned to ensure that the composite contained no large voids. Each composite strip was crushed to an individual indentation depth of either 0.125, 0.25, 0.375, 0.5, 0.625, 0.75, 0.875 or 1 mm respectively, with two composite specimens of each type being tested to each level. Subsequent to the crush testing, the samples were C-scanned, to allow the difference between the sample before and after testing to be examined, and the size of any damaged region to be ascertained.

The size of each delamination was measured by firstly scanning the C-scanned image into a computer and then using Data Translations Global Lab Image software to measure the area of delamination, directly from the images. The

delamination area was obtained from the computer in terms of pixels, this being converted to mm^2 using the calibration facility of the software.

Examination of the damage location was carried out in the manner discussed in the previous section, using a fluorescent dye penetrant. In this instance, however, rather than cutting 1 cm wide sections, the damage location was examined by polishing 2 mm from each specimen between examinations. In this manner, the damage was examined at regular intervals through the section, rather than a brief snap-shot through the centre and at the edges being obtained, as was the case in the previous study. Photography was again carried out using a 3200 ASA film, to give images of the whole damage region. The size of the damage regions dictated that a montage technique be used to give a full image. The montage was achieved by scanning the photographs into a computer file and processing the images using image analysis and manipulation software. This enabled large montage sections to be easily produced for later analysis. The location of delaminations, revealed by fluorescence microscopy, was used to compare damage formation within the reference panels and those panels which contained RFLG's.

6.3.2. Results and discussion

6.3.2.1 C-scanned data

The results of C-scanning for reference panels and RFLG panels after impact are shown in figures 6.7 and 6.8 respectively.

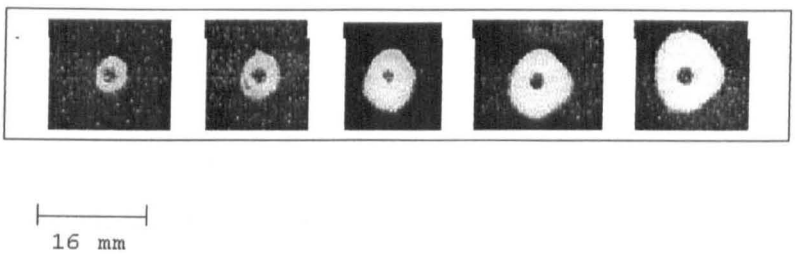

(a) (b) (c) (d) (e)

Figure 6.7. C-scanned images of the damage contained in the reference panels. Picture (a) is for an indentation depth of 0.5 mm; (b) 0.625 mm; (c) 0.75 mm; (d) 0.875 mm and (e) 1 mm.

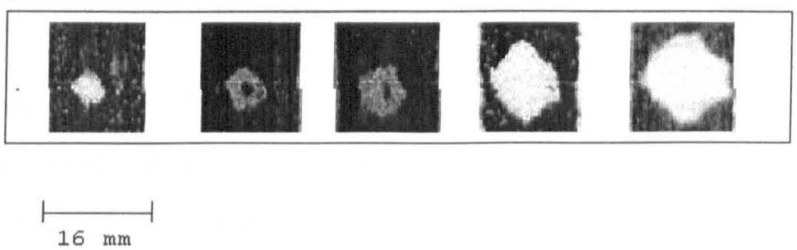

(a) (b) (c) (d) (e)

Figure 6.8. C-scanned images of the damage contained in the panels containing RFLG's. Picture (a) is for an indentation depth of 0.5 mm; (b) 0.625 mm; (c) 0.75 mm; (d) 0.875 mm and (e) 1 mm.

Measurement of the damage area for impacted specimens revealed that there was no significant difference between the areas observed for the reference panels and those containing the RFLG's (see figure 6.9).

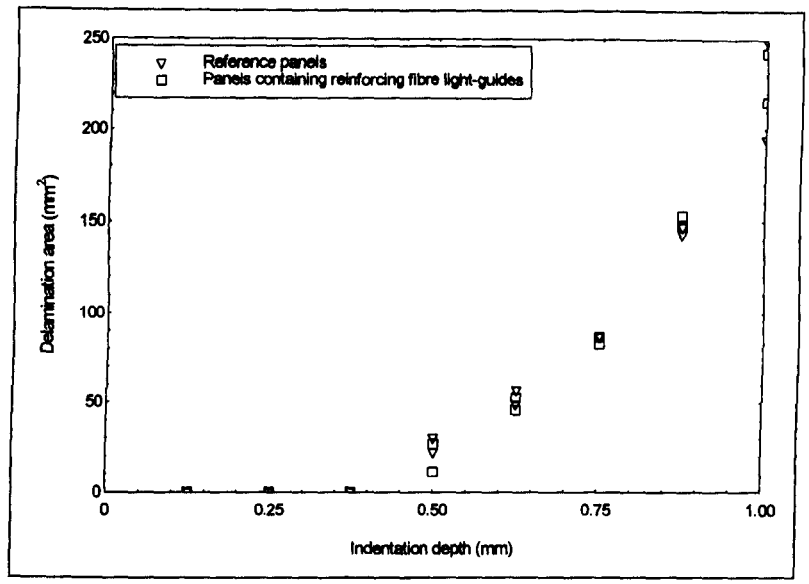

Figure 6.9. Graph of the change in delamination area with indentation depth for both panels containing RFLG's and reference panels.

6.3.2.2. Damage location study

6.3.2.2.1. Visual observations

Results from the damage location study revealed no damage within the composite before an indentation depth of 0.625 mm. This is in conflict with the C-scanned data, but it was considered possible that, due to the small damage area, the damage could have been missed in the polishing process. At indentation depths of 0.625 mm and above, the damage was evident.

It was observed that, in general, the location of damage was consistent between reference panels and panels containing RFLG's. The location of the delamination damage showed no significant variation, tending to be towards the edges at

the point of indentation, with very little damage observed in the centre of the specimen. Further from the indentation point, to either side of the central section, damage was observed to move in towards the centre of the composite. This happened with both the reference panels and those containing RFLG's. It would appear, therefore, that the presence of an RFLG in the composite did not adversely affect the resistance of the composite to delamination, in the arrangement chosen for the tests.

Example sections for a reference panel and a panel containing RFLG's are shown in figures 6.10 and 6.11 respectively; the similarity in the location of the delaminations can be seen, with cracks and delaminations showing up as bright lines. The reasons for the particular morphology of the impact damage pattern will be discussed in the next section.

One difference in the damage pattern does, however, present itself. A crack can be seen emanating from the location of an RFLG in figure 6.11, and running vertically through plies 2 and 3 of the composite. Plies 2 and 3 can be seen to have bent in the vicinity of the RFLG's, to make space for them within the composite. The observed crack tends to emanate from either the central or 2 mm displaced RFLG. The composite in this region is already bent around the RFLG's and will, thus, suffer more serious bending stress as it is in the centre of the specimen. The stress fields leading to the formation of this crack are discussed in more detail in the following section.

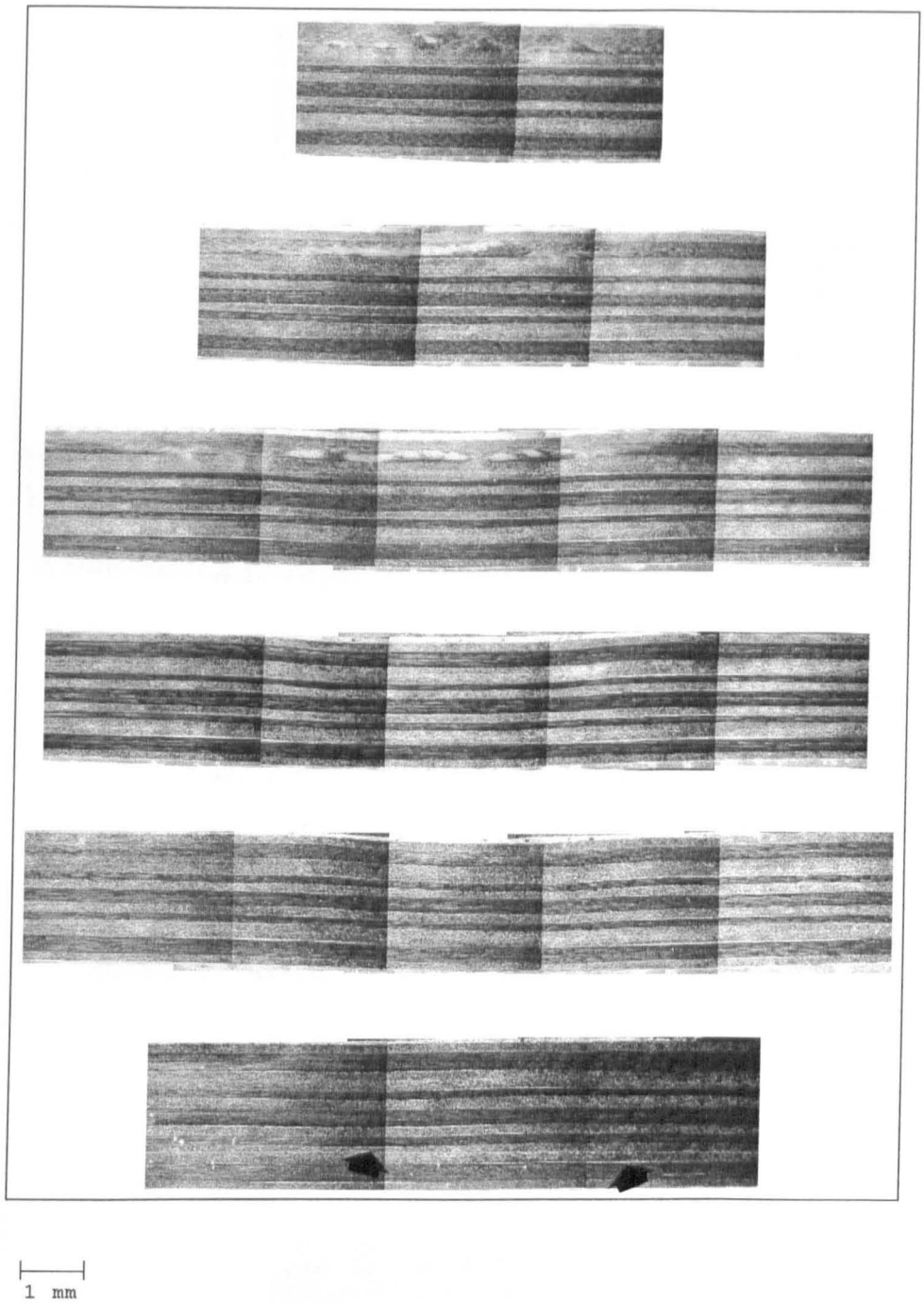

Figure 6.10. Sections showing the location of damage within a reference panel crush tested to an indentation depth of 1 mm. Fractures can be observed as bright lines within the composite structure, with two typical delaminations being indicated with arrows.

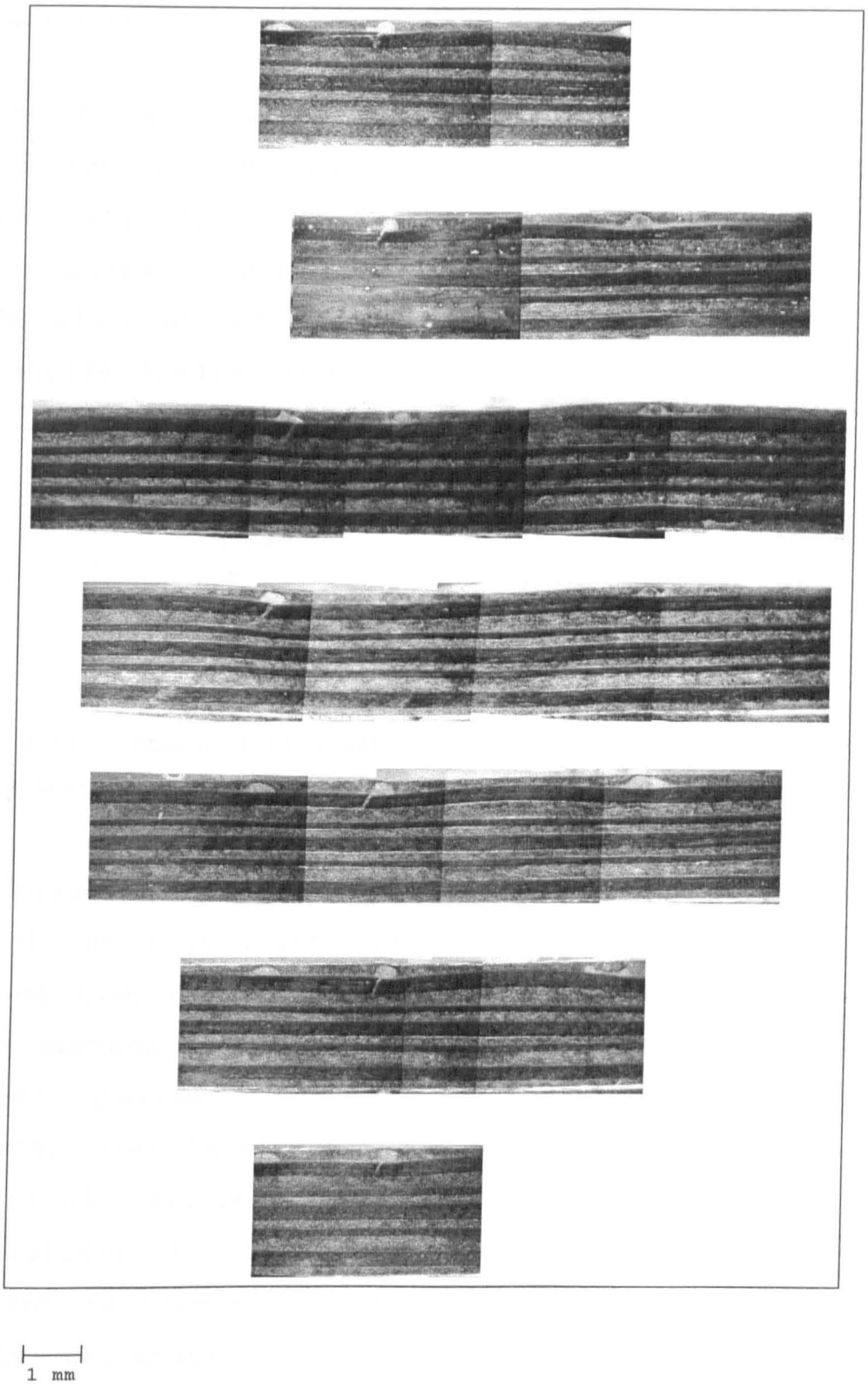

Figure 6.11. Sections showing the location of damage within a composite panel containing RFLG's, crush tested to an indentation depth of 1 mm. Fractures can be observed as brightlines within the composite structure.

6.3.2.2.2. Consideration of stresses

As it is bent, the composite will be under a complex arrangement of stresses, considered macroscopically in figure 6.12. It can be seen that the composite experiences both compressive and tensile loading within its structure, in the plane of the composite sheet. Also there will be a compressive loading through the thickness of the composite at B, due to the tup impinging on its surface.

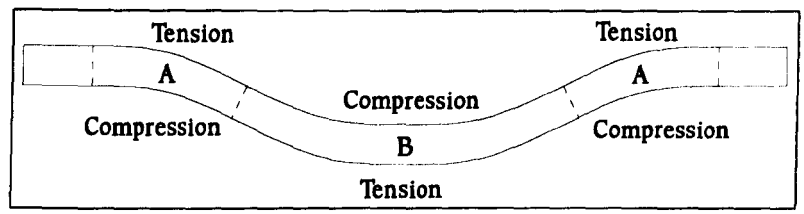

Figure 6.12. Stress fields within the composite plate subjected to a bending load.

Considering the tensile and compressive loadings towards the ends of the bent region (marked A in Figure 6.12) it is observed that the top surface is under tension, while the bottom surface is in compression. At the centre of the specimen (marked B in figure 6.12) the situation is reversed. Both tensile and compressive loading will lead to interfacial stresses building up which can cause delaminations to develop between unlike plies. The situation is considered for the four possible combinations of ply orientations and loadings. These being 0/90 interface in tension and compression and also 90/0 interface in tension and compression, the resultant deformations, leading to delaminations occurring, are shown in figure

6.13. In this figure, the deformations of the 0 and 90 degree plies are considered for a ply which is unconstrained. Any difference in unconstrained deformations between the two plies indicates an area where a differential stress will build up and failure is more likely to occur. Thus, delaminations due to bending could occur on all of the considered interfaces.

Liu (1987) examined the bending stiffness mismatch and proposed this as the reason for delamination to occur. The deformation induced by bending, again for separate unconstrained plies is considered in figure 6.14. This would suggest that delamination would only occur upon a 90/0 interface, as in a 0/90 interface any delaminations will tend to close, due to the manner in which the two plies deform. In the case of the 90/0 interface, as the 90 degree ply resists bending, it will tend to cause tensile stresses at the interface, leading to delamination. However, in the situation considered by this study, the indentor contacts the surface at a point, not in a line. Under these circumstances, a 90° rotation of the sample inverts the interface from 0/90 to 90/0 and delaminations can occur because of the bending stiffness argument. Thus, delamination would be expected to occur on both 0/90 and 90/0 interfaces, as observed in the polished sections.

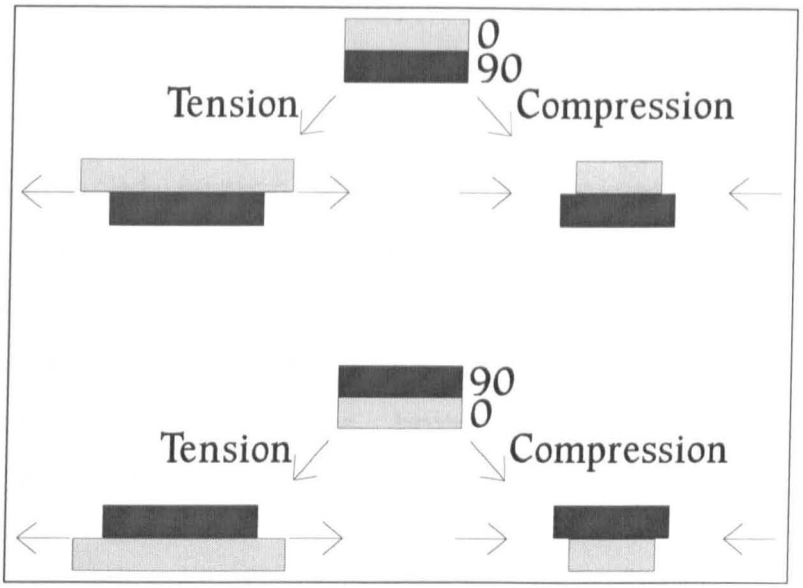

Figure 6.13. Illustration of the unconstrained ply deformation due to various loading regimes, showing the strain differentials which lead to delamination.

Little delamination was seen in the centre of the specimen, directly beneath the indentation point. It is proposed that this is directly due to the presence of the tup. The compressive loading associated with the tup, as it impinges on the surface, would tend to close any cracks which run into that region, limiting the potential for delamination.

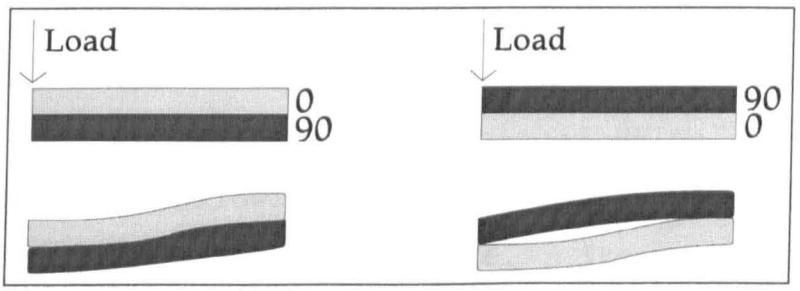

Figure 6.14. Schematic illustration of the effect of bending on delamination of the composite, from the bending analysis view point.

The tup, being hemispherical, will constrain a circular region at the centre of the deformed zone. Delamination will not be likely to occur in this zone and, thus, a central undamaged region would be anticipated. Refering to figures 6.7 and 6.8, such a region can be seen to be present in the C-scans. When considering the damaged sections shown in figures 6.10 and 6.11, the expected morphology of the damage must, therefore, be born in mind. Damage would therefore be expected to occur in the shaded region shown in figure 6.15.

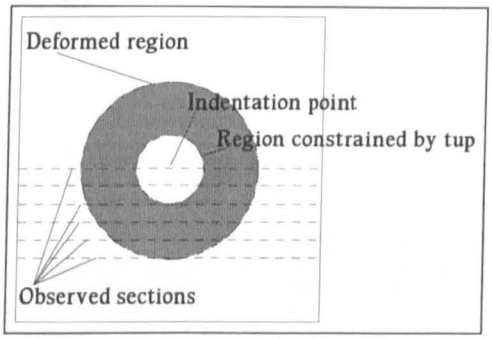

Figure 6.15. Schematic illustration showing the deformation induced by a central indentation and the spread of the damaged region through the examined sections.

The observed crack through plies 2 and 3, emanating from the region of the central or 2 mm displaced RFLG, is thought to develop in the following manner. The geometry of the situation is shown in figure 6.16. It can be seen that prior to the indentation process, plies 2 and 3 are already bent due to the presence of the RFLG. Once indentation commences, the central region on the top surface will be under compressive loading. It is, thus, likely that if the

compressive load is sufficiently great, the composite will fail in this region, in the manner expected of a compressive failure. The expected morphology of such a crack is shown in figure 6.16 and is seen to be similar to the observed crack form. Thus, elimination of the bent region around the RFLG would reduce the likelihood of this form of failure.

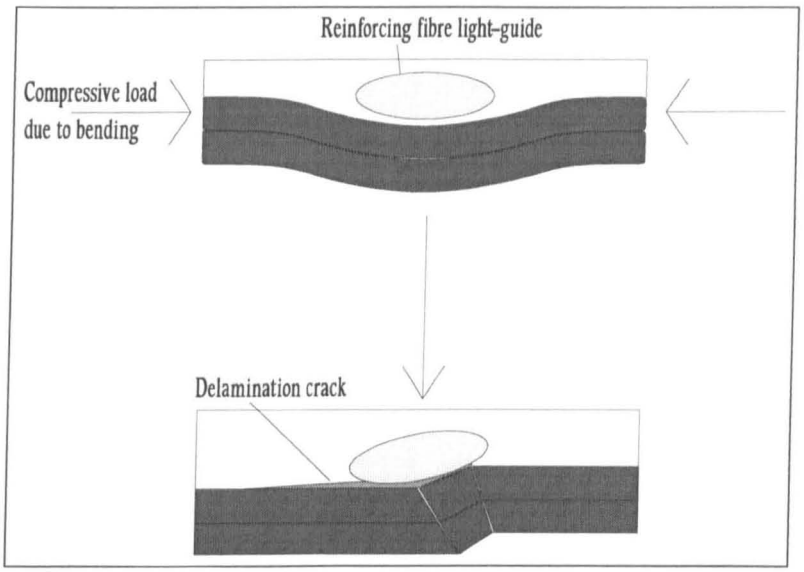

Figure 6.16. Illustrating the failure of plies 2 and 3 due to the presence of the RFLG and compressive loading due to bending.

6.4. Summary

The effect that the presence of an RFLG has on the damage location within the composite has been established. It was first established that the interface between Sylgard 184 and the composite was very weak, while that of OG137 was relatively strong. However, despite the weak interface, initial impact studies found the delamination area was not increased by the presence of RFLG's. More detailed studies,

using crush testing, confirmed that the area of delamination was not increased although a damage mechanism associated with the RFLG was identified. The stresses generated during crush testing were considered in order to account for the damage morphology observed in the samples.

Chapter 7. Results 5: Examination of the performance of the reinforcing fibre light-guide as a damage sensor

This chapter contains a discussion of the performance of the RFLG as a sensing element. In order to understand the sensing process of the RFLG and its performance when embedded within the composite, a knowledge of the average strength of the fibres and adhesion between the fibres and cladding was also necessary.

7.1. Average fibre strength determination and adhesion testing

7.1.1 Experimental

The fragmentation test was used to establish both the adhesion between the fibres and cladding and also the Weibull statistical information for the fibres. This approach was adopted as it overcame some of the difficulties involved in handling the fibres which precluded the testing of single, unembedded, fibres. The interfacial shear strength was obtained using a classical force balance approach, with the conversion factor of 4/3 used to calculate the ineffective length from the average fragment length.

Single silica fibres were separated, from a fibre bundle which had been cleaned. Care was taken to handle the fibres only at one end, leaving the majority of the fibre in a virgin condition. A thin layer of Sylgard 184 was cast into a square polypropylene tray, which was approximately 10 cm wide. The separated fibre was then placed upon the surface of the resin. It was found to be possible to place two fibres within each tray without them interfering with each other. Once this had been done, a second thin layer of resin was poured on top of the fibres. To cure the resin, the specimens were placed in an oven at either 100°C or 35°C, the cure times being 1 hour or 3.5 days respectively.

Once the specimens had been cured, the resin was removed from the tray. Microscopic examination was used to locate the fibres and tensile 'dog-bone' specimens with a gauge length of 15 mm were stamped out of the resin. Care was take to ensure the fibre lay straight along the gauge length of the specimen.

Testing was carried out using a Polymer Laboratories Mini-Mat miniature tensile testing machine, at a speed of 0.5 mm/min, to an applied strain of 20 %. Fragments were observed using oblique lighting, with a stereo-microscope being used to view the specimen. A CCD camera was attached to the camera mounting tube of the microscope, allowing the fragmentation process to be recorded on to a video. After all the specimens had been examined, the videos were reviewed and the strain at which each fragment formed was measured.

7.1.2 Results and Discussion

The fragmentation specimen cured at 100°C displayed fragmentation of the fibre immediatly after curing (shown in figure 7.1a); other areas, with no fragmentation, displayed a sine wave bending of the fibre (shown in figure 7.1b). This was due to thermal contraction of the resin after curing. When cured at 35°C no fragments were formed, although small amounts of sine wave deformation could still be observed. Test results, therefore, were all for the 35°C cure schedule.

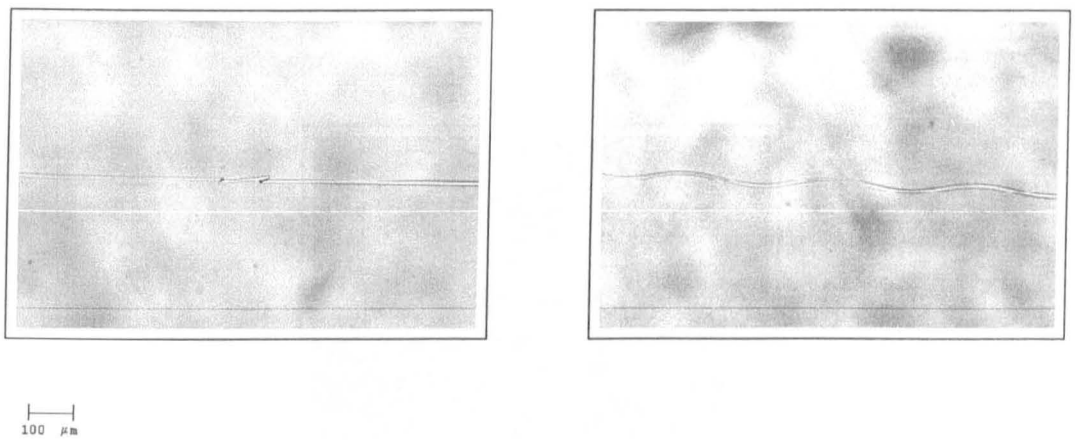

(a) (b)

Figure 7.1 a and b. Showing a thermal expansion induced fragment and rippling respectively.

Fragmentation was observed in all 16 of the samples tested. However, 5 of the samples were seen to give a large amount of debonding and interfacial damage, or to contain a fibre which was seriously off-centre in the specimen (see figure 7.2). These samples were rejected, as the assumption that

the strain in the fibre is equal to the strain in the matrix, could not be made with any level of certainty. Thus, 11 samples were accepted, giving a total of 80 fragments. An example of an acceptable sample is shown in figure 7.3. The strain at which each fragment occurred was recorded from the video screen, by measuring between fixed gauge marks on the sample. A gauge length of 12 mm was considered for each specimen as this length was clearly visible at all levels of strain. Due to the relatively small number of fragments, it was decided to plot all of these on the same Weibull plot, giving a considered gauge length of 132 mm. Considering the samples together also had the advantage that any analysis would be more accurate, as there were more fragments under consideration.

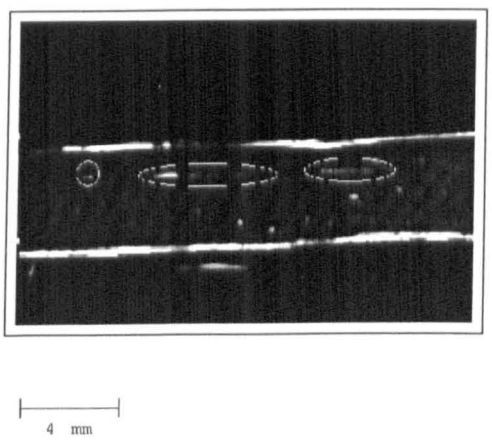

Figure 7.2. Photograph of a fragmentation specimen showing a seriously off-centre fibre with debonding along the fibre. This can be seen by the extended bright regions (circled) indicating fibre breakage and debonds running along the fibre edges.

The calculation process used in this study, was a development of that proposed by Shioya and Takaku (1995). This involved modification of the Weibull equation to allow

determination of the Weibull parameters from a plot of the natural logarithm of the number of fractures against the natural logarithm of the strain. The equation that they developed is shown in equation 7.1.

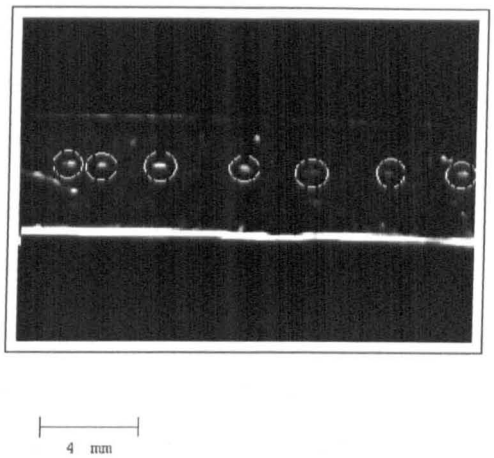

Figure 7.3. Photograph of a fragmentation specimen showing good fragmentaion. This can be seen by the bright points of light (circled) indicating an isolated break with no disturbance to the surrounding interface.

$$\ln(n) = \beta \ln(\varepsilon_c) - \beta \ln(\lambda / E_f) + \ln(L/L_o) \qquad 7.1$$

where n is the number of fragments, L is the gauge length, ε_c is the composite strain and E_f is the fibre modulus. The parameters β and λ are the Weibull shape and scale parameters respectively. The parameter L_o is defined by Shioya and Takaku (1995) as an arbitrarily determinable reference length. However, it is proposed in this study that L_o must, in fact, be the sample gauge length used, so as to remove any arbitrary changes in the Weibull shape and scale parameters. The other modification to the equation is to use a Weibull equation in terms of strain rather than

stress, as in equation 7.1. The equation used in this study is therefore given in equation 7.2.

$$\ln(n) = \beta \ln(\varepsilon_c) - \beta \ln(\varepsilon_o) \qquad 7.2$$

where ε_o is the Weibull scale parameter in terms of strain. The Weibull parameters were determined by plotting a graph of $\ln(n) : \ln(\varepsilon_c)$. This gave a straight line at lower strains, which had a gradient of β, with ε_o being determined from the intercept on the strain axis. At higher strain, the curve deviated from the predicted straight line, as the area over which stress within the fibres is building up becomes more significant reducing the overall fibre stress. The graph of the experimental results is shown in figure 7.4. By using the above method, β was determined to be 1.23, with ε_o being calculated to be 0.0013, for a gauge length of 132 mm.

From this data it was possible to predict values for ε_o at different gauge lengths. This was achieved by using weakest link theory to predict the value of ε_o at the new gauge length, using equation 7.3.

$$\varepsilon_{o(1)} / \varepsilon_{o(2)} = (L_2 / L_1)^{1/\beta} \qquad 7.3$$

The classic Weibull plot of $\ln(\ln(1/(1-P_f))) : \ln(\varepsilon)$, where P_f is the probability of fibre failure, could then be plotted using equation 7.4

$$P_f = 1 - \exp(-(\varepsilon/\varepsilon_o)^{\beta}) \qquad 7.4$$

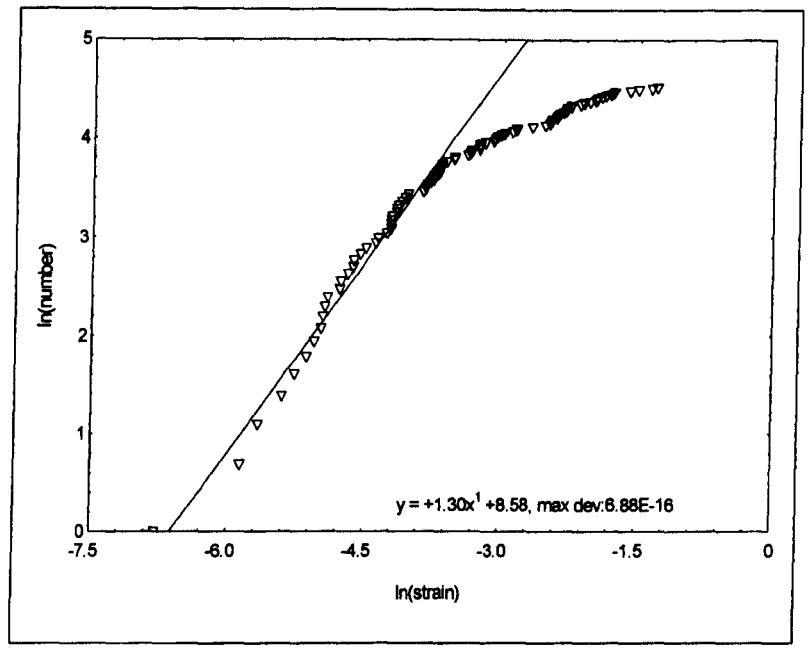

Figure 7.4. Experimental plot of the number of fragments against the strain, showing the straight line fitted to the initial measurements.

As an example, the Weibull plot at 40 mm was calculated and is shown alongside the curve fitted to the experimental data in figure 7.5.

The strength of the interface was calculated using the relationship shown in equation 7.5.

$$\tau = (D * E_f * \varepsilon_c) / (2 * \delta) \qquad 7.5$$

where τ is the interfacial shear stress, D is the fibre diameter, measured as 9 μm, E_f is the fibre modulus of 72 GPa, ε_c is the composite strain when $\ln(\ln(1/(1-P_f)))=0$ and δ is the ineffective length. The ineffective length was calculated using equation 7.6.

$$\delta = 4/3 * \text{the average fragment length.} \qquad 7.6$$

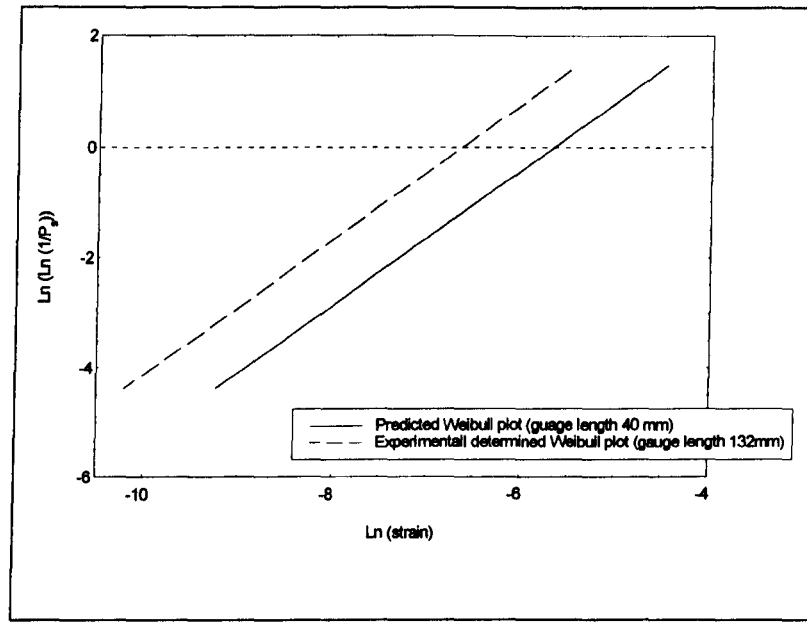

Figure 7.5. Weibull plot calculated from the measured Weibull parameters.

The values of ε_c and the average fragment length used, were those at saturation of the fragmentation process. This meant that the interfacial shear stress calculated was the limiting value and, therefore, the interfacial shear strength. From the experimental study, the average fragment length was found to be 1.63 mm, δ was calculated to be 2.2 mm and τ was calculated as 54 MPa.

7.2. The effect of bend stresses on the fibres

7.2.1. Experimental

Having established the statistics of fibre failure for the fibres used in this study, the effect of bending at different ROC was examined. This initially involved the modelling of the stress in a fibre for a given bend radius. The stress at which 1, 50 or 99 % of the fibres would be expected to have broken, for each bend radius was also calculated.

The effect of bending on the transmission characteristics of the RFLG was tested by bending five separate RFLG's around fixed radii. The radii used in this study were 3, 7, 10, 13, 17, 24, 35, 43 and 52 mm, the RFLG being encased in shrunk HST to support it while it was bent. The encased fibre was connected to a white-light source and a photodetector. Modelling of the effect of this bending on the RFLG was undertaken, incorporating stress concentration factors to provide data on the interaction of breaks.

7.2.2. Results and Discussion

7.2.2.1 Theoretical effect of bending on the fibres

Stress analysis was carried out on the fibres in the following manner. The strain in a bent glass fibre was calculated, using simple beam analysis, considering the

fibre as a beam with one fixed end and one free end, with a distributed load. The equation used in this analysis is shown in equation 7.7.

$$\varepsilon = y*\delta*C_1/L^2 \qquad 7.7$$

where y is the distance from the neutral axis, δ is the deflection, C_1 is a constant relating to the beam geometry and L is the length of interaction. The value of C_1 for this geometry was 8. The value of y was taken as the radius of the fibre, $4.5*10^{-6}$ m. The values of δ and L were calculated considering that the fibre was bent around 90°, using the construction shown in figure 7.6.

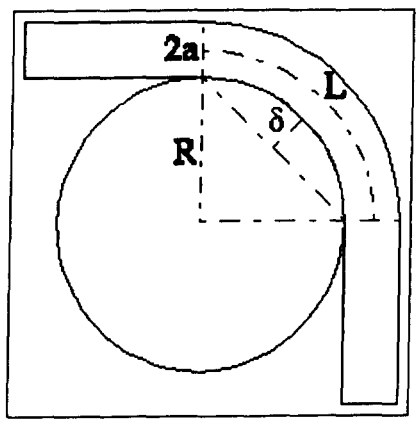

Figure 7.6. Schematic construction showing how L and δ are calculated.

From figure 7.6 it can be seen that equations 7.8 and 7.9 can be used to calculate L and δ respectively.

$$L = (\pi*(2R+2a))/4 \qquad 7.8$$

$$\delta = 0.293*R \qquad 7.9$$

where R is the ROC and a is the fibre diameter, taken as $4.5*10^{-6}$ m.

Using these equations, the stress in the fibre for any ROC can be calculated. Figure 7.7 shows the stress values predicted for ROC's varying over two orders of magnitude.

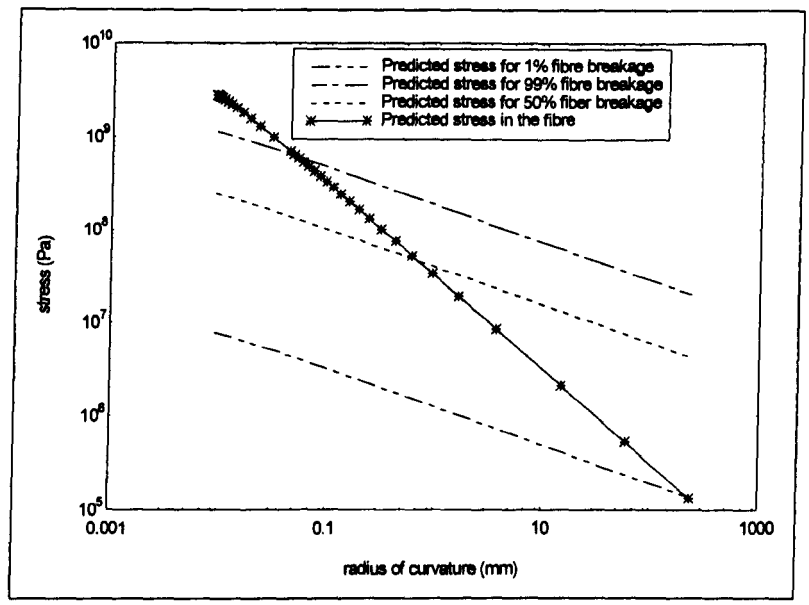

Figure 7.7. Predicted number of fibres failing for a given radius of curvature.

Also shown in figure 7.7 are lines showing the stresses for given probabilities of failure, either 1, 50 or 99 %, which were calculated as follows. The operative Weibull scale parameter for each interaction length, assuming a 90° bend, was calculated using equation 7.3. Having calculated the Weibull scale parameter, the probability of failure was fixed as 0.01, 0.5 or 0.99 and calculation of the strain was carried out for each value of P_f, using equation 7.4. The

values of strain calculated were converted to stress using the fibre modulus of 72 GPa.

Looking at figure 7.7, it can be seen that a significant number of fibres will have broken, for an ROC as large as 1 cm and the first few fibres would be expected to have failed at an ROC of greater than 10 cm. This is the area at which the sensing action of the RFLG would be expected to be operative. The effect of bend induced fibre breakage on the light transmission characteristics, at these larger ROC was, therefore, examined.

7.2.2.2. Effect of bending on transmission characteristics

Results from the experimental study revealed a steady loss of light with decreasing bend radius, as shown in figure 7.8.

The number of fibres expected to break at each bend radius was modelled using an analysis similar to that described in the construction of figure 7.7. Equation 7.7 was again used to calculate the strain in the fibres, with the same value of C_1. The values of L and δ were calculated using equations 7.8 and 7.9 respectively, for each ROC used in the study, assuming that the length of interaction equated to a 90° bend in the fibre. From this strain data, the probability of failure of the fibre was calculated using equation 7.4, having first calculated ε_o for each of the radii used in the test, using equation 7.3.

Having calculated the probability of a fibre failing when a bend of each of the radii, was introduced, the percentage of light lost due to fibre failure in the bend was calculated. The probability of failure equated to the percentage of light lost, as it was assumed that each fibre carried an equal amount of light prior to fracture and none afterwards.

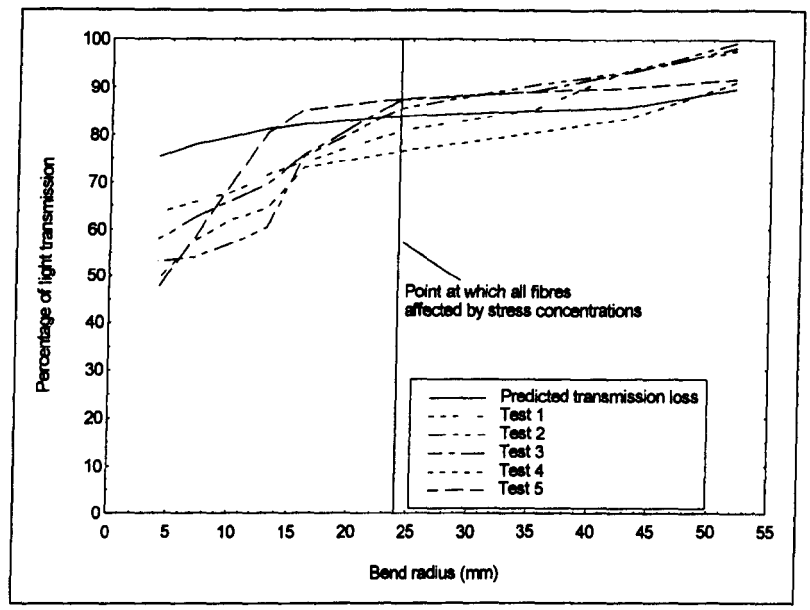

Figure 7.8. Graph of the experimental loss curves from the bending experiment alongside predicted loss curves.

An extension to this model was considered by the inclusion of a strain concentration correction. The sample under consideration was a coated bundle of fibres and, thus, a strain concentration could affect the fibres around a broken one. The strain concentration used in this model were 1, 1.33 and 1.15 for fibres unaffected by a broken one, next to a broken one and the next-nearest neighbour to a broken one respectively (See section 2.1.3). The determination of

these values has been discussed in chapter 2. The number of fibres around a broken one was taken as 6 for both nearest and next-nearest neighbours, as it was assumed that the fibres were closely packed.

The inclusion of the strain concentration factor meant that a proportion of the fibres would experience a higher probability of failure than the unaffected fibres. The presence of three operative probabilities of failure was allowed for in the model, by assuming that the overall probability of failure was a weighted mean of those, calculated using equation 7.10.

$$Pf_o = (Pf_n * F_n + Pf_s * F_s + Pf_t * F_t) / (F_n + F_s + F_t) \qquad 7.10$$

where Pf_o is the overall probability of failure, Pf_n is the probability of failure of the fibre unaffected by the strain concentration, Pf_s is the probability of failure of the fibres affected by the first strain concentration and Pf_t is the probability of failure of the fibres affected by the second strain concentration. The values F_n, F_s and F_t are the number of fibres experiencing each probability of failure.

The results from the model concurred well with the measured loss for each ROC, at the start of the test (see figure 7.8). At tighter bend radii, the measured light-loss deviated from the model used. The deviation from the model is thought to result from the presence of strain concentrations as the fibres break. At the point of deviation (marked by a vertical line), it is noted that all

the glass fibres within the RFLG are either broken or affected by a strain concentration. At this point it is expected that the strain concentrations from fibre breaks will increase (see chapter 2), leading to accelerated failure of fibres and explaining the deviation from the model.

7.3. Preliminary Sensing Studies

7.3.1. Experimental

Preliminary sensing studies were carried out in the manner described in section 6.2. Samples containing 30, 50 and 125 μm optical fibres, along with samples containing RFLG's, were impact tested. The precise arrangement of the specimen was discussed previously. To give good optical coupling of light into and out of the light-guides, the edges of the specimen were polished to a 1 μm diamond finish.

Prior to impact testing, the intensity of the light transmission through each fibre was measured. This was carried out using an X-travel stage on to which the specimen was clamped. The stage was positioned between a white-light source and a photodetector fixed opposite each other. A linear variable displacement transducer (LVDT) was used to monitor the movement of the X-travel stage. A schematic illustration of the experimental setup is shown in figure 7.9.

In order to measure the light intensity through the fibres, the panel was scanned between light source and detector. To measure the variation of light intensity, the photodetector was connected via a data aquisition board to a computer. The LVDT was also connected to the computer, to allow spatial positioning of the intensity measurements. This setup allowed a trace of intensity against position to be obtained, showing the position and intensity of the embedded fibres. It was ensured that the test could be replicated by repeating each examination three times, with the sample being removed and repositioned between tests.

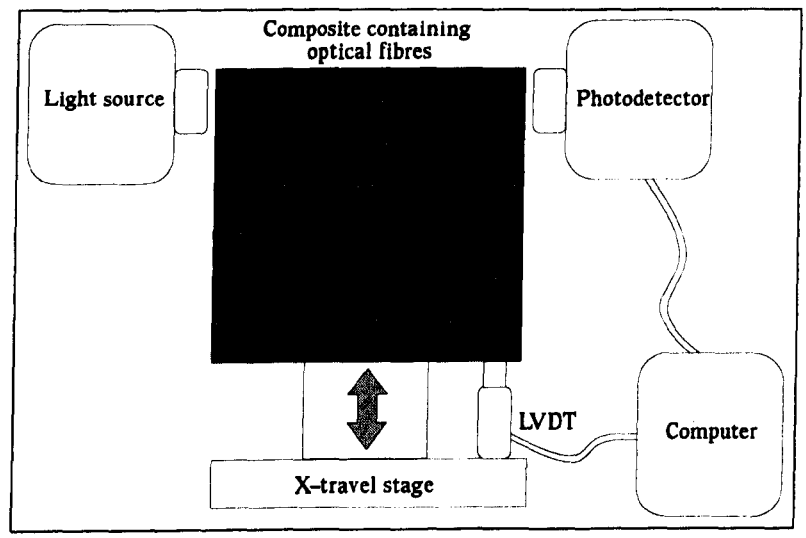

Figure 7.9. Schematic illustration of the experimental setup used in the preliminary sensor study.

The specimens were impacted using a Rosand instrumented impact tester, with a 20 mm hemispherical tup. Two test specimens of each type were impacted at each of four different impact energies, namely 2 J, 4 J, 6 J and 8 J. One specimen of each type was impacted at 10 J. The light intensity through each fibre was again measured subsequent

to the impacts and compared with the intensities measured prior to impact.

7.3.2. Results and Discussion

Examples of the optical fibres used in this study are shown in figure 7.10.

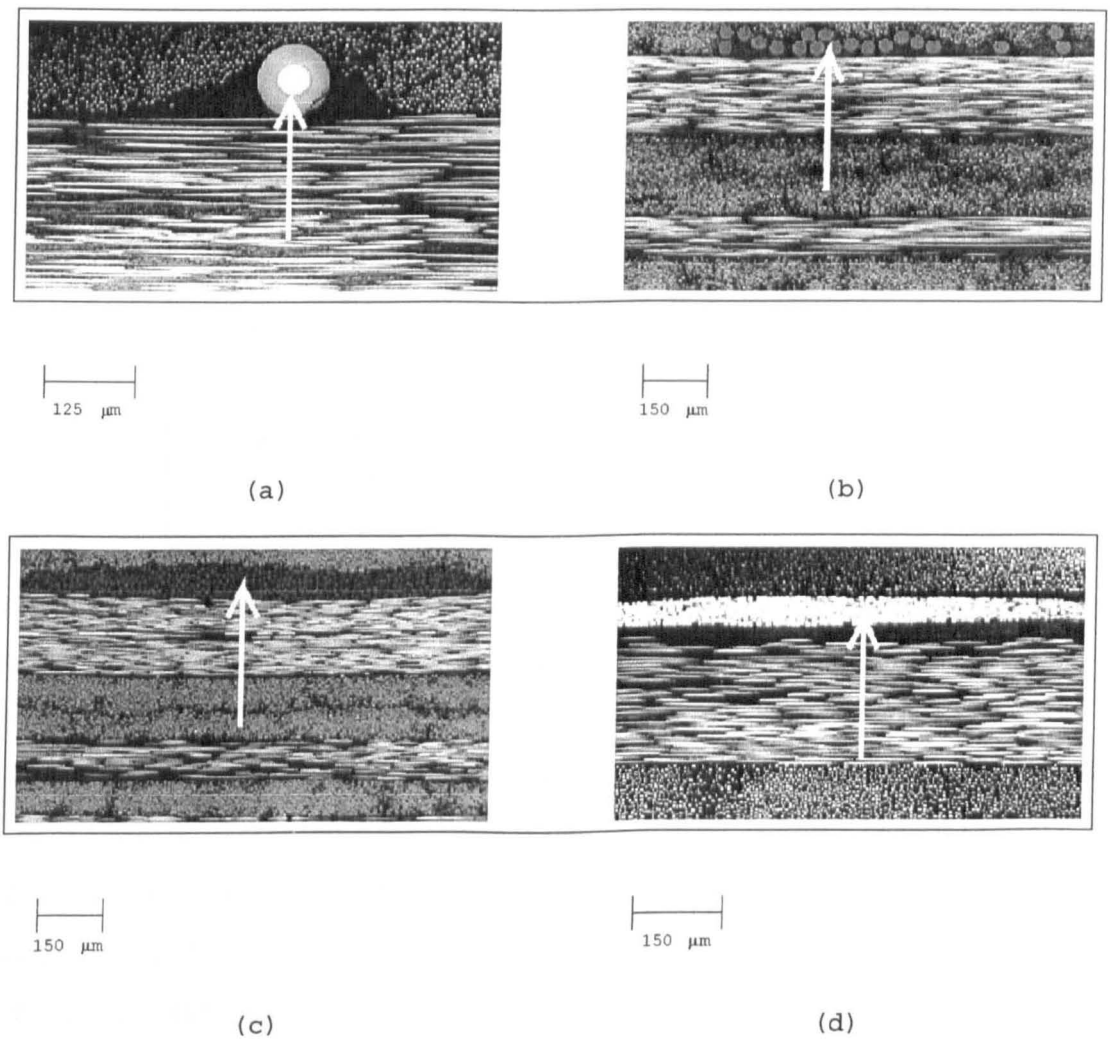

Figure 7.10. Photographs showing a) 125 µm, b) 50 µm, c) 30 µm and d) RFLG.

Results from impact testing revealed that the different optical fibres used in this study had markedly different sensor performance. The intensity measurement approach gave a clear indication of where impact damage had taken place, with a distinct loss of intensity in one or more of the fibres around the impact point. The results discussed are all taken from the fibres between plies 15 and 16.

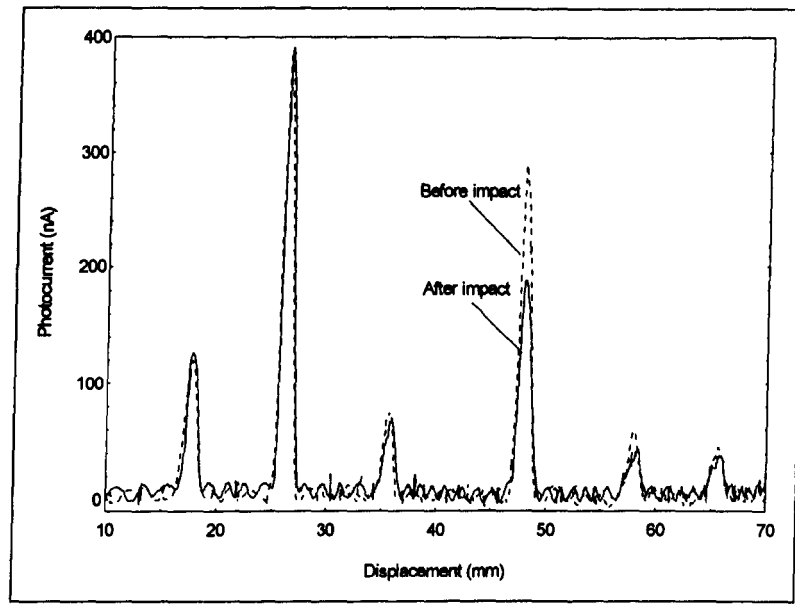

Figure 7.11. Intensity trace from the bottom fibres of a RFLG based composite panel taken before and after a 2 J impact.

In the case of the RFLG's, specimens impacted with an energy of 2 J showed detection of the damage. An example of the light intensity trace is shown in figure 7.11. At this energy, none of the other fibre types gave a change in intensity and, hence, no damage was detected.

The 30 and 50 μm optical fibres gave the same sensitivity as each other, being capable of detecting a 4 J impact, or

greater. An example of the light intensity trace for a specimen containing 50 μm optical fibres, is shown in figure 7.12.

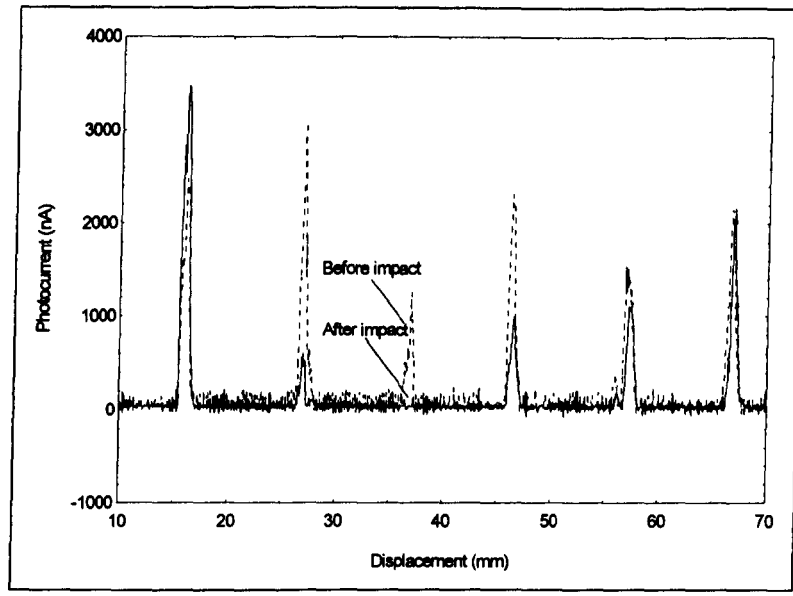

Figure 7.12. Intensity trace from the bottom fibres of a 50 μm optical fibre panel taken before and after a 6 J impact.

The 125 μm optical fibres proved to be the least sensitive, only being capable of detecting a minimum of a 6 J impact (See figure 7.13).

From this study it was concluded that the RFLG was capable of acting as a sensor for impact damage detection and was indeed more sensitive to impact damage than the conventional optical fibres.

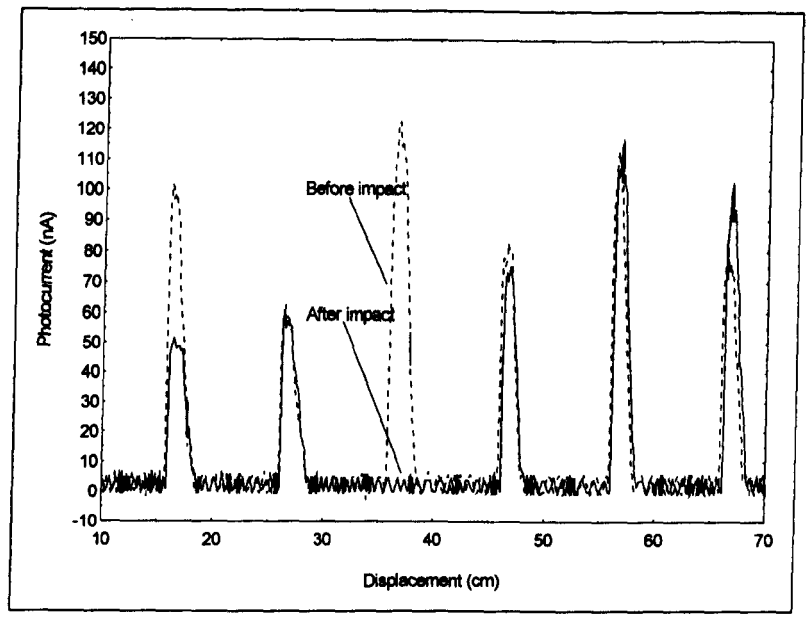

Figure 7.13. Intensity trace from the bottom fibres of a 125 μm optical fibre panel taken before and after a 6 J impact.

7.4. Crush testing

7.4.1. Silicone clad RFLG's

7.4.1.1. Experimental

Samples were prepared in the manner discussed in section 6.3. The edges of the samples were polished to ensure good light coupling into and out of the RFLG. To connect the RFLG's to a white-light source a clamp was made which could be fixed firmly on to the edge of the composite sample. The fibre-optic output from the light source could then be firmly attached. To give stable connection of the RFLG to a photodetector, large core optical fibres were fitted in to clamps made from polyethylene. These were then clamped on

to the edge of the composite, over the location of the embedded RFLG's. The large core optical fibre could then be connected to photodetectors. The security of the attachment was examined by clamping a section of composite to a light source and photodetector and subjecting it to a violent displacement. The light transmission was measured before and after this, with the process being repeated five times.

Crush testing was carried out using an Instron 1195 machine at a testing speed of 0.5 mm/min. The 20 mm hemispherical tup, used in impact testing, was mounted on to the crosshead and lowered on to the clamped sample. The limit switches were set so that a constant withdrawn height could be attained. The crosshead was withdrawn to the limit switch cut-off point, and an initial reading of the transmitted light intensity was taken. The tup was then pressed into the composite to a depth of 0.125 mm, before being withdrawn to the limit switch cut-off point. A reading of the light transmission was then taken again. This process was repeated on the same sample of composite in the same location, for indentation depths of 0.25, 0.375, 0.5, 0.625, 0.75, 0.875 and 1 mm. Testing was repeated for 7 samples.

7.4.1.2. Results and Discussion

Examination of the security of the clamps, which were used to connect the RFLG's to the photodetectors, revealed that the light intensity varied by less than 0.1 % of the reading

after each shake. It was therefore deemed that the security of the clamping arrangement was sufficient.

The results from crush testing revealed that the RFLG was capable of detecting damage development within a composite, confirming the results from the preliminary study (section 7.3). However, it went on to extend this, revealing that progressive damage could be successfully followed. Results from each of the fibres positioned centrally, 2 mm and 4 mm away from the point of contact, for all of the specimens are shown in figures 7.14, 7.17 and 7.18 respectively.

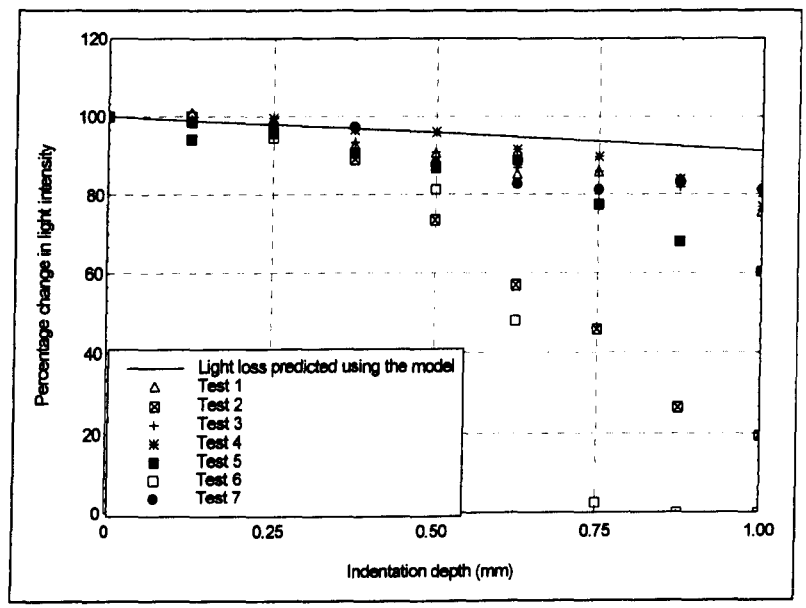

Figure 7.14. Results of crush testing of composite panels containing Sylgard 184 clad RFLG's, showing the light transmission data from the central fibres. The predicted curve is also shown as the solid line.

Concentrating firstly on data from the central fibres, shown in figure 7.14, it can be seen that as the indentation depth increases, more light is lost from the RFLG's. This follows a generally linear path, particularly over the first few

points, to an indentation depth of 0.5 mm. After this point there is greater deviation from the straight line. The point of deviation marks the start of the composite experiencing large scale failure, and it is suggested that the failure will be the cause of the excess losses experienced at higher indentation depths.

Prediction of the expected loss for a given indentation depth was carried out in a similar manner to that used in the bending analysis (section 7.2), carried out using equations 7.4 and 7.7. In this case, the beam was assumed to be fixed ended and to have a distributed loading regime. This gave the value of the constant C_1, in equation 7.7, as 384. The value of y, the distance from the neutral axis, was again taken as the radius of the fibre, $4.5*10^{-6}$ m. The deflection, δ, was taken as being equal to the indentation depth, plus the thickness of ply 1.

Strain was again calculated, using equation 7.6, with the gauge length being taken as 16 mm, the unsupported width of the specimen.

Having calculated the maximum strain in the centre of the fibre, the strain distribution was assumed to be as shown in Figure 7.15. It can be seen that the distribution consists of three main regions. These are due to the shape attained by the fibres under bending. At the edges, the fibre top surface will be under tension with the bottom under compression. The situation is reversed in the centre section of the fibre. Thus, the maximum strain experienced

in the centre falls away along the fibre to zero before a maximum strain in the edges is attained. This is shown in the strain profile in figure 7.15. Equation 7.7 takes no account of the strain at the edge of the bent region, giving only the maximum strain. Therefore, the maximum edge strain was calculated by assuming that the edge region, up until the zero strain point, took the form of a beam with one fixed end, of length 4 mm, with a distributed load. This gave the value of C_1 as 8, enabling the maximum edge strain to be calculated.

In the above manner, the maximum strains at the edge and in the middle of the fibre, as well as the presence of zero points were known. The position of these points along the fibre were also known, allowing elliptical curves to be fitted through the maxima from the two closest zero points, as shown in figure 7.15. This allowed the strain in a reinforcing fibre to be modelled precisely, allowing the calculation of the probability of failure for small segments around the bend. In this way the number of fibres failing in each segment of the fibre bundle could be calculated and the total number of broken fibres for such a bend could be predicted.

The ellipses are symmetrical around a mirror line running perpendicularly through the maximum strain point. Because of this, only half of each of the three curves need be considered, with twice the number of segments experiencing that strain. However, due to the symmetry of the two outer curves, only one of these need be considered, with

calculated values being multiplied to take this into account.

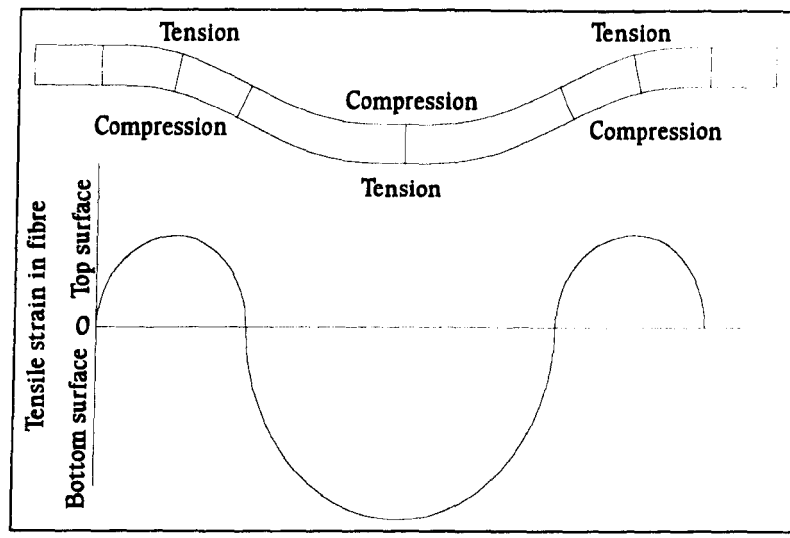

Figure 7.15. Schematic illustration of the bending of a reinforcing fibre due to indentation, and the induced strain profile in the fibre.

The strain in the fibre was calculated for segments of 100 μm length around the bend. The Weibull statistical probability of failure was calculated for a 100 μm segment, using equation 7.4. Again, the strain concentration factors were included using a weighted mean calculation, which took exactly the same form as shown in equation 7.10. The total number of reinforcing fibres broken at each indentation depth was calculated from these probabilities of failure. From this analysis the predicted curve shown in figure 7.14 was calculated assuming that each fibre initially carried the same amount of light and after fracture carried none.

It can be seen that the curve fit was reasonable at the lower indentation depths, although it deviated at higher

indentation depths. The deviation is thought to be due to the unpredictable and increasing strains resulting from the fracture of the composite. It should be noted that delaminations are only observed to occur from an indentation point of 0.5 mm, with large scale fracture occuring from 0.625 mm.

Turning attention to figure 7.17, considering the fibre positioned 2 mm from the point of indentation, it can again be seen that the experimental data shows a decrease of light intensity with increasing indentation depth. This change in intensity also follows a broadly linear pattern and again the deviation occurs at the point where the composite starts to fracture.

As the RFLG is offset from the centre, it will not be indented to the same degree as the central one. Thus, the strain in the fibres will be lower and the model to predict the induced light loss must be modified. This was done by assuming that the deformation was linear, with a deformed length of 16 mm and a central displacement equal to the indentation depth. The new value of δ for the displaced fibres can then be calculated using trigonometry and the construction shown in figure 7.16. It can be seen that the predicted curve fits the data reasonably, only significantly deviating once the composite has started to macroscopically fracture.

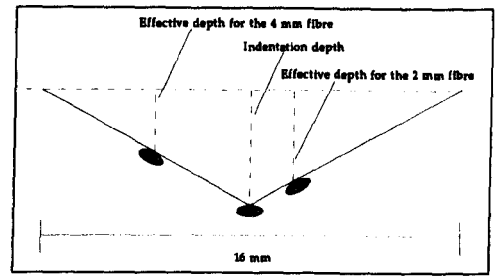

Figure 7.16. Construction to allow the calculation of the maximum indentation depth for the fibres displaced from the indentation point.

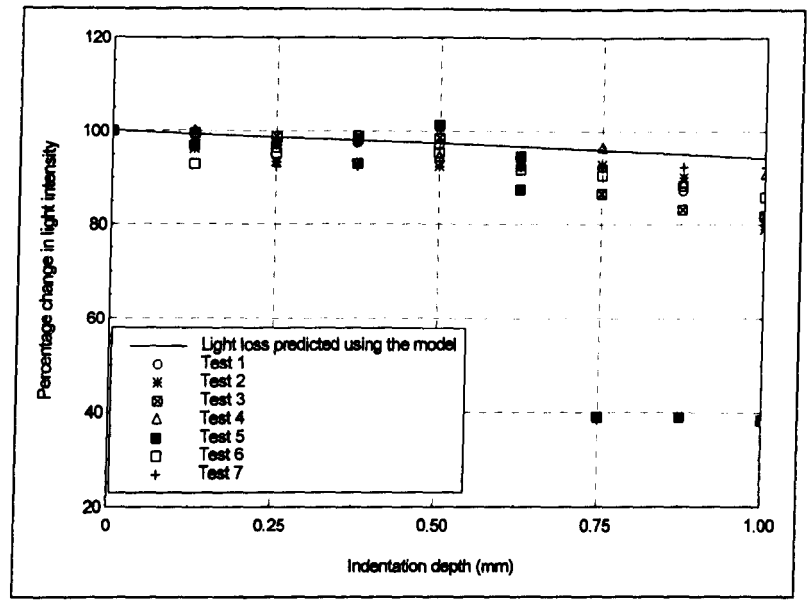

Figure 7.17. Results of crush testing of composite panels containing Sylgard 184 clad RFLG's, showing the light transmission data from the fibres placed 2 mm from the centre. The predicted curve is also shown as the solid line.

Finally, looking at figure 7.18, in which the fibre is positioned 4 mm from the point of indentation, it can be seen that as the indentation progressed, there was increased loss of light, indicating detection of the increasing damage. It can also be seen that this is less marked than in the previous two RFLG positions, indicating that further away from the indentation, or impact point, the damage would

be expected to be less severe. Using the new value of δ calculated in the method described above, the predicted curve again fits reasonably with the experimental data, up to the point where the composite starts to fail.

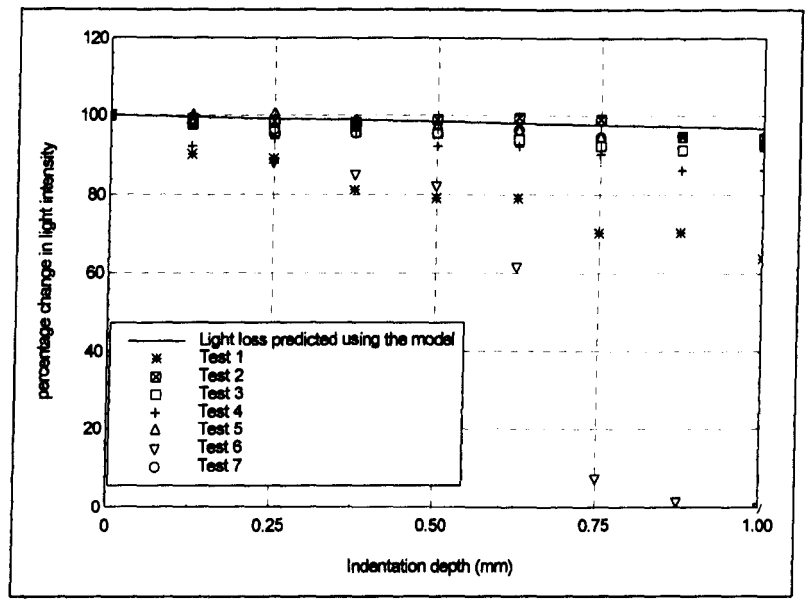

Figure 7.18. Results of crush testing of composite panels containing Sylgard 184 clad RFLG's, showing the light transmission data from the fibres placed 4 mm from the centre. The predicted curve is also shown as the solid line.

It is observed that the model, while fitting the measured data reasonably, tends to underestimate the number of fibres breaking. This is likely to be due to the overestimation of the failure stress by Weibull analysis, due to the likelihood of rejection of the weakest fibres because of breakage at the time of separation, or due to stresses imposed during handling.

7.4.2. OG137 clad RFLG

7.4.2.1. Experimental

It has been stated previously that more than one potential cladding material, with suitable optical properties, was available for this study (chapter 3). Once the principle of the RFLG had been demonstrated using Sylgard 184, another of the potential cladding materials was examined. This was done with a view to overcoming some of the problems associated with the use of a silicone resin. The main problem, its poor adhesion, was demonstrated in section 6.1. Epoxy Technologies OG 137 was selected as the cladding material to be examined, as it was a rigid thermoplastic, whereas the other possible materials were flexible. Excessive flexibility of the Sylgard 184 was perceived as one of the problems associated with its use.

Initial results (section 3.1) had shown that OG 137 gave a distinctly void-filled coating, because of the rapid evaporation of the solvent in which it was dissolved. It was, however, found to be possible to produce a RFLG, containing minimal voiding, by baking the coated fibre bundle in an oven at a temperature of 200°C. At this temperature, the OG 137 had softened and the voids collapsed, leaving a relatively void-free solid. The thickness of this coating was found to be too low to sustain guiding over all but short distances once embedded. The problem was overcome by applying 2 further coatings of the OG 137, each coating being baked as before.

A single RFLG of this type was embedded centrally between plies 1 and 2 of composite specimens with the same dimensions and lay-up sequence as those used for crush testing of the silicone-clad RFLG's. Crush testing of the composite was then carried out as for the silicone coated RFLG's, although no reference specimens were tested. This was due to the lack of material available and because it was not deemed essential as this was a preliminary study; the main thrust of this study was to demonstrate the effectiveness of the RFLG as a sensor for damage, when a more rigid cladding material was employed. The RFLG's were connected to the light source and photodetectors in the same manner as used previously (section 7.4.1).

7.4.2.2. Results and discussion

Optical microscopy was carried out on an embedded OG 137 coated RFLG, with it being analysed using both transmitted and reflected light (see figures 7.19a and 7.19b).

It can be seen that the fibres guide well throughout the bundle, indicating that the coating is of reasonable quality. It can also be seen that the disruption to the composite, caused by the presence of the RFLG is lower than that caused by the Sylgard 184 clad RFLG. This is thought to be due to melting or softening of the OG 137 during cure of the composite, allowing it to deform under the curing pressure, minimising disruption. The deformation would be

in stark contrast to the resistance of the thermosetting Sylgard 184, which would have little tendency to deform. Thus, OG 137 gives a much less disruptive, more practical, RFLG from this point of view.

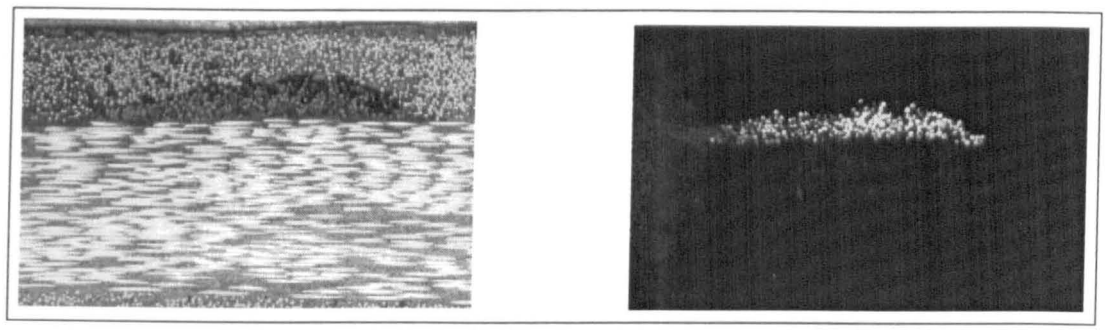

(a) (b)

Figure 7.19 a and b. Showing photographs of an OG 137 clad RFLG in both reflection and transmission. The lower disruption caused by this fibre, compared to the silicone clad RFLG is clearly seen.

Results from crush testing the specimens containing the OG 137 coated RFLG's are shown in figure 7.20. It can be seen that, as with the silicone-coated RFLG's, at low deformation the light loss is linear. However, in the case of the OG 137 coated RFLG's, this linear region is much shorter. This is thought to be due to the brittle nature of the OG 137. Whereas the silicone resin will tend to blunt cracks and reduce the effect of external pressures on the reinforcing fibres, the brittle OG 137 will tend to crack and lead to premature failure of the reinforcing fibres. This would account for the rapid loss in linearity shown by the RFLG in this instance. Prior to this loss, it can be seen that,

again, the model fits reasonably with the loss data, although more data would be required to confirm this.

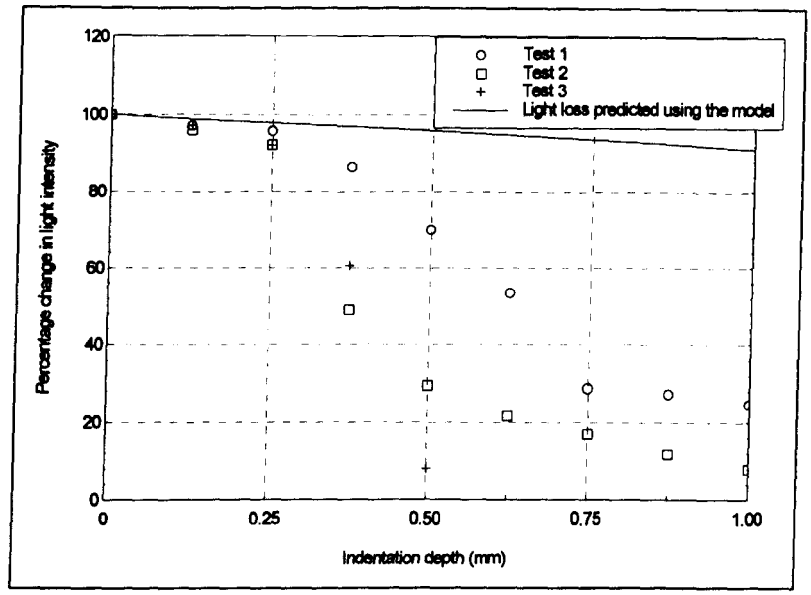

Figure 7.20. Results of crush testing of composite panels containing OG 137 clad RFLG's. The predicted curve is also shown as a solid line.

7.4.3. Comparison of different cladding materials

From comparison of the results obtained using OG 137 as the cladding and those obtained using Sylgard 184, it would appear that the operation of the RFLG as a sensor, depends critically on the properties of the cladding. Both of the cladding materials used in this study proved suitable for use in the production of a RFLG and to be capable of acting as damage sensors. The operation of the sensor produced using these cladding materials has been modelled over the linear region of the curve. It has, however, been observed that the portion over which the model is valid depends on the cladding material.

The sensor produced using Sylgard 184 as the cladding material, performed in a linear fashion until the composite started to delaminate and crack extensively. At this point the central RFLG, and that placed 2 mm from the centre, were seen to deviate from the straight line predicted. The RFLG placed 4 mm from the centre was seen to deviate to a lesser extent. In this manner, the spread of the damage through the composite could be followed. The RFLG clad using OG 137, however, was seen to deviate from the straight line at much lower indentation depths.

This difference in performance of the two RFLG's is thought to be due to the difference in the properties of the cladding. The silicone resin is highly flexible and will, thus, conform to the deformation induced by indentation. In contrast, the OG 137 is brittle and will tend to crack under deformation. The effect of this cracking will be to break more reinforcing fibres than would be predicted by the model. Due to the unpredictable nature of the cracking within the RFLG, the amount of loss after cracking of the cladding will be random. The softer nature of the Sylgard 184 would eliminate the effect of cladding failure, postponing the onset of random failure until the failure of the composite itself.

7.5. Summary

The statistical failure parameters of the fibres and the level of adhesion between fibre and matrix were determined. This provided necessary data for the development of a model which was used to predict the performance of the RFLG.

Experimental data was presented, from preliminary impact studies, which demonstrated the potential of the RFLG to detect damage. This preliminary study was extended, using RFLG's with a Sylgard 184 silicone resin cladding, by crush testing. The RFLG was shown to be capable of monitoring progressive damage development. This was followed by an examination of an alternative cladding polymer, Epoxy Technologies OG137, which was also shown to be capable of acting as a progressive damage sensor; however differences in the performance of the two sensors were observed. These differences and the reasons for them were analysed.

Chapter 8. Conclusions and further work

8.1. Conclusions

It has been demonstrated that glass reinforcing fibres can be used to produce an RFLG.

The optical performance of the RFLG has been maximised for the raw materials used.

It has been demonstrated that the RFLG can be embedded within carbon fibre composites.

The effect of the RFLG on the delamination of the composite under impact was found to be negligible despite the low adhesion between the cladding material and the composite.

Once embedded, the RFLG has been found capable of acting as an impact energy sensor. A linear fall in the transmitted light intensity was found to apply, up to the point that either the composite, or the cladding of the RFLG, started to crack.

Two cladding materials were examined in this study, one flexible and the other brittle. The flexible cladding was found to leave linearity at the point that the composite started to crack excessively. The brittle cladding was found to leave linearity once the cladding material started to fail. This occurred before failure of the composite.

The fall in transmitted light intensity, due to an impact event, was modelled. The effect of other potential loss mechanisms have also been considered, both qualitatively and quantitatively.

8.2. Further Work

8.2.1. Immediate Requirements

There are two key areas which require addressing in order to maximise the performance and sensitivity of the RFLG as an impact sensor. These are the quality of the reinforcing fibres used and the properties of the cladding material.

Addressing the first of these, the reinforcing fibres used in this study were commercially available high purity silica reinforcing fibres. It was found, in this study, that the glass used to produce the fibres contained voids, indicating the possibility of voids within the fibres. Both the presence of voids and any damage to the fibre surfaces would limit the light guiding performance of the fibres. Therefore, the performance of the sensor would be improved if these imperfections could be eliminated. Of these, the voiding would be the easier to address, in the following manner. The raw glass could be carefully prepared and selected to minimise the presence of voids. The use of optical glass production techniques may also help in this aim.

It would be more difficult to address the problem of surface damage, as this is introduced by the process of handling the fibres after production, and also in subsequent preparation. However, one way of limiting this damage would be to apply the cladding material at the point of fibre manufacture. This would prevent the handling associated with fibre cleaning and subsequent cladding application, which was unavoidable in this study.

Turning attention to the other key area, for this application the cladding material must have suitable optical properties to allow the formation of a light-guide and also suitable mechanical and adhesion properties, to enable it to act as a reinforcing element in the composite. This study has demonstrated that the properties of the cladding material has a significant effect on the performance of the sensor. It is suggested that the ideal properties for a prospective cladding material would be:

i) Refractive index as low as possible

ii) Very good adhesion to epoxy matrix resins

iii) Mechanical properties which are similar to the epoxy matrix, but slightly more flexible.

The first two will maximise the optical performance of the RFLG and the stress transfer in to the fibre. The third of these, however, is important to maximise the performance of the sensor. It was found, in this study, that a brittle cladding lost its linear response to impact damage, when the

cladding failed; whereas a flexible cladding maintained its linearity until failure of the composite. Therefore, a flexible cladding gives more information on the failure of the composite and is thus desirable. The mechanical properties must, however, be close to those of the matrix to allow the RFLG to contribute to the composite strength.

8.2.2. Potential Scope

If a suitable cladding material was available, this sensor would open up a number of very interesting possibilities. In this study, the RFLG has been presented as a discrete optical fibre within a carbon fibre composite. However, the existence of a favourable cladding material would allow the construction of sensing plies which could be incorporated as part of the structure. This would have the following advantages:

i) Impact location and sizing could be easily obtained, if crossed sensing plies were used.

ii) The composite would be hybridised using both glass fibres and a flexible resin, allowing the impact performance to be altered in the ways discussed in the literature survey.

Thus, a truly versatile, simple, cost effective sensor would be obtained.

References

Akhavan F. Watkins S. E. & Chandrashekhara K. (1995). *Hybrid sensors for impact-induced strain in smart composite plates.* SPIE PROC. **2444**, 514-525.

Ambur D. R. Starnes Jr. J. H. & Prasad C. B. (1995). *Low-speed impact damage-initiation characteristics of selected laminated composite plates.* AIAA J. **33**, 1919-1925.

Andersons J. & Tamuzs V. (1993). *Fiber and interface strength distribution studies with the single-fiber composite test.* COMP. SCI. TECHNOL. **48**, 57-63.

Ashbee K. (1989). *Fundamental principles of fiber reinforced composites.* TECHNOMIC.

Aslown E. M. Nardin M. & Schultz J. (1989). *Stress transfer in single fibre composites: Effect of adhesion, elastic modulus of fibre and matrix and polychain mobility.* J. MAT. SCI. **24**, 1835.

Bader A. H. Maclean T. S. M. Gazey B. K. Miller J. F. & Ghafoori-Shiraz H. (1989). *Radiation from circular bends in multimode and single-mode optical fibres.* IEE PROC.-J **136**, 147-151.

Bader A. H. Maclean T. S. M. Ghafouri-Siraz H. & Gazey B. K. (1991). *Bent slab ray theory for power distribution in core and cladding of bent multimode optical fibres.* IEE PROC.-J **138**, 7-12.

Bader A. H. & Maclean T. S. M. (1991). *Transition and pure bending losses in multimode and single-mode bent optical fibres.* IEE PROC.-J **138**, 261-268.

Baxevanakis C. Jeulin D. & Valentin D. (1993). *Fracture statistics of single-fibre composite specimens.* COMP. SCI. TECHNOL. **48**, 47-56.

Bibo G. A. & Hogg P. J. (1996). *Review: the role of reinforcement architecture on impact damage mechanisms and post-impact compression behaviour.* J. MAT. SCI. **31**, 1115-1137.

Bibo G. Leicy D. Hogg P. J. & Kemp M. (1994). *High-temperature damage tolerance of carbon fibre-reinforced plastics: part 1: impact characteristics.* COMPOSITES **25**, 414-424.

Bibo G. A. Hogg P. J. & Kemp M. (1995). *High-temperature damage tolerance of carbon fibre-reinforced plastics: part 2: post-impact compression characteristics.* COMPOSITES **26**, 91-102.

Biddulph R. H. Bader M. G. & Buxton A. (1994). *A simple apparatus for measuring the tensile-strength of single fibres.* MEAS. SCI. TECHNOL. **5**, 9-11.

Boll D. J. Bascom W. D. Weidner J. C. & Murri W. J. (1986). *A microscopy study of impact damage of epoxy-matrix carbon-fibre composites.* J. MAT. SCI. **21**, 2667-2677.

Broutman L. J. (1965). *Failure mechanisms for filament reinforced plastics.* MOD. PLAST. **April** 143-151 and 214-216.

Campbell J. F. Vanderheiden E. G. Martinez L. A. Cairnes D. S. & Abdallah M. G. (1992). *A multi-purpose sensor for composite laminates based on a piezo-electric film.* J. COMPOSITE MAT. **26**, 334-349.

Cantwell W. J. (1996). *The interlaminar fracture behaviour of carbon fibre reinforced plastics at low temperatures.* PROC. INSTN. MECH. ENGRS. **210**, 1-7.

Cantwell W. J. & Morton J. (1991). *The impact resistance of composite materials - a review.* COMPOSITES **22**, 347-362.

Cawley P. (1994). *The rapid non-destructive inspection of large composite structures.* COMPOSITES **25**, 351-357.

Chaturvedi S. K. & Seirakowski R. L. (1985). *Effects of impactor size on impact damage-growth and residual properties in an SMC-R50 composite.* J. COMPOSITE MAT. **19**, 100-113.

Chang C. C. & Sirkis J. (1995). *Optical sensors embedded in composite panels for impact detection.* SPIE PROC. **2444**, 502-513.

Chi Z. & Chou T. W. (1983). *An experimental study of the effect of prestressed loose carbon strands on composite strength.* J. COMPOSITE MAT. **17**, 196-209.

Chi Z. Chou T. W. & Shen G. (1984). *Determination of single fibre strength distribution from fibre bundle testings.* J. MAT. SCI. **19**, 3319-3324.

Chiu W. K. Galea S. C. Zhang H Jones R. & Lam Y. C. (1994). *The use of piezoelectric thin film sensors for structural integrity monitoring.* J. INTELL. MAT. SYS. STRUCT. **5**, 683-693.

Chohan V. & Galiotis C. (1997). *Effects of interface volume fraction and geometry on stress redistribution in polymer composites under tension.* COMP. SCI. TECHNOL. **57**, 1089-1101.

Clark G. (1989). *Modelling of impact damage in composite laminates.* COMPOSITES **20**, 209-214.

Cowking A. Attou A Siddiqui A. M. Sweet M. A. S. & Hill R. (1991)a. *Testing E-glass fibre bundles using acoustic emission.* J. MAT. SCI. **26**, 1301-1310.

Cowking A. Attou A. Siddiqui A. M. Sweet M. A. S. & Hill R. (1991)b. *An acoustic emission study of failure by stress corrosion in bundles of E-glass fibres.* J. MAT. SCI. **26**, 301-306.

Cox H. L. (1952). *The elasticity of paper and other fibrous materials.* BRIT. J. APPL. PHYS. **3**, 72-92.

Daniels H. E. (1945). *The statistical theory of the strength of bundles of threads.* PROC. ROY. SOC. LOND. **183A**, 405-435.

Dry C. (1995). *Smart multiphase composite materials which repair themselves by a release of liquids which become solid.* SPIE PROC. **2444**, 410-413.

Dry C. (1996). *Procedures developed for self-repair of polymer matrix composite materials.* COMPOSITE STRUCT. **35**, 263-269.

Dry C. & Mcmillan W. (1997). *A novel method to detect crack location and volume in opaque and semi-opaque brittle materials.* SMART. MATER. STRUCT. **6**, 35-39.

Favre J. P. & Jacques D. (1990). *Stress transfer by shear in carbon fibre model composites. Part 1: Results of single-fibre fragmentation tests with thermosetting resins.* J. MAT. SCI. **25**, 1373-1380.

Fiedler B. & Schulte K. (1997)a. *Photo-elastic analysis of fibre-reinforced model composite materials.* COMP. SCI. TECHNOL. **57**, 859-867.

Fiedler B. & Schulte K. (1997)b. *Stress concentrations in single and multiple fibre model composites.* Paper presented at IPCM '97, EGER.

Fukuda H. & Kawata K. (1976). *On the stress concentration factor in fibrous composites.* FIBRE SCI. TECHNOL. **9**, 189-203.

Ghatak A. K. & Thyagarajan K. (1989). *Optical Electronics.* CAMBRIDGE UNIVERSITY PRESS.

Gloge D. (1972). *Bending loss in multimode fibres with graded and ungraded core index.* APPL. OPT. **11**, 2506-2513.

Goldrein H. T. Palmer S. J. P. & Huntley J. M. (1996). *Microstructural strain analysis of composites using high magnification moire interferometry.* Paper Presented at APPL. OPT. DIV. CONF. READING.

Grace J. L. Poland S. H. Murphy K. A. Claus R. O. Abraham P. & Sridharan K. (1996). *Embedded fibre optic sensors for structural damage detection.* SPIE PROC. **2718**, 196-201.

Greene J. A. Tran T. A. Bhatia V. Gunther M. F. Wang A. Murphy K. A. & Claus R. O. (1995). *Optical fibre sensing technique for impact detection and location in composites and metal specimens.* SMART. MATER. STRUCT. **4**, 93-99.

Greenhalgh E. Bishop S. M. Bray D. Hughes D. Lahiff S. & Millson B. (1996). *Characterisation of impact damage in skin-stringer composite structures.* COMPOSITE STRUCT. **36**, 187-207.

Gros X. E. & Lowden D. W. (1995). *Electromagnetic testing of composite materials.* INSIGHT **37**, 290-293.

Gurvich M. R. Dibenedetto A. T. & Pegoretti A. (1997)a. *Evaluation of the statistical parameters of a Weibull distribution.* J. MAT. SCI. **32**, 3711-3716.

Gurvich M. R. Dibenedetto A. T. Ranade S. V. (1997)b. *A new statistical distribution for characterizing the random strength of brittle materials.* J. MAT. SCI. **32**, 2559-2564.

Hagege R. & Bunsell A. R. (1988). *Testing methods for single fibres. In 'Composite materials series volume 2. Fibre reinforcements for composite materials.'* Ed. A. R. Bunsell. ELSEVIER SCIENCE PUBLISHERS.

Hale K. F. Hokenhull B. S. & Christodoulou G. (1980). *The application of optical fibres as witness devices for the detection of plastic strain and cracking.* 'STRAIN' **October**, 150-154.

Haque A. & Raju P. K. (1995). *Sensitivity of the acoustic impact techniques in characterizing defects/damage in laminated composites.* J. REINF. PLAST. COMP. **14**, 280-296.

Harrick N. J. (1967). *Internal reflection spectroscopy.* INTERSCIENCE PUBLISHERS.

Harris B. (1986). *Engineering composite materials.* INSTITUTE OF METALS.

Hedgepeth J. M. & van Dyke P. (1967). *Local stress concentrations in imperfect filamentary composite materials.* J. COMPOSITE MAT. **1**, 294-309.

Herrera-Franco P. J. & Drzal L. T (1992). *Comparison of methods for the measurement of fibre/matrix adhesion in composites.* COMPOSITES **23**, 2-27.

Highsmith A. L. & Keshav S. (1997). *Quantitative assessment of fibre fracture in damaged laminates using X-ray radiography.* J. COMPOS. TECHNOL. RES. **19**, 10-19.

Hill R. & Okoroafor E. U. (1995). *Weibull statistics of fibre bundle using mechanical and acoustic emission testing: the influence of interfibre friction.* COMPOSITES **26**, 699-705.

Hitchen S. A. & Kemp M. J. (1995). *The effect of stacking sequence on impact damage in a carbon fibre/epoxy composite.* COMPOSITES **26**, 207-214.

Hitchen S. A. & Kemp R. M. J. (1996). *Development of novel cost effective hybrid ply carbon-fibre composites.* COMP. SCI. TECHNOL. **56**, 1047-1054.

Hofer B. (1987). *Fibre optic damage detection in composite structures.* COMPOSITES **18**, 309-315.

Hong S. & Liu D. (1989). *On the relationship between impact energy and delamination area.* EXP. MECH. **June**, 115-120.

Hull D. (1981). *Introduction to composite materials.* CAMBRIDGE UNIVERSITY PRESS.

Ireman T. Thesken J. C. Greenhalgh E. Sharp R. Gadke M. Maison S. Ousset Y. Roudolff E. & La Barbera A. (1996). *Damage propagation in composite structural elements - coupon experiments and analyses.* COMPOSITE STRUCT. **36**, 209-220.

Jenq S. T. & Chang C. K. (1995). *Characteriation of piezo-film sensors for direct vibration and impact measurement.* EXP. MECH. **September**, 224-232.

Jiangliang Y. Qing X. Guohua Y. Dexiu H. & Yeulong Z. (1996). *Etched fibreoptic strain sensor.* SPIE PROC. **2895**, 408-414.

Jones R. T. Sirkis J. S. Friebele E. J. & Kersey A. D.. (1995). *Location and magnitude of impact detection in composite plates using neural networks.* SPIE PROC. **2444**, 469-480.

Joshi S. P. & Munir N. I. (1996). *Impact location, energy and damage detection in smart structures.* SPIE PROC. **2718**, 185-193.

Joshi S. P. & Sun C. T. (1985). *Impact induced fracture in a lamiated composite.* J. COMPOSITE MAT. **19**, 51-66.

Kaczmarek H. (1995). *Ultrasonic detection of damage in CFRPs.* J. COMPOSITE MAT. **29**, 59-95.

Kaczmarek H. & Maison S. (1994). *Comparative ultrasonic analysis of damage in CFRP under static indentation and low-velocity impact.* COMP. SCI. TECHNOL. **51**, 11-26.

Kaiser J. H. (1993). *Millimetre wave heating for thermographic inspection of carbon fiber-reinforced composites.* MATER. EVAL. **May**, 597-599.

Karasek M. L. Strait L. H. Amateau M. F. & Runt J. P. (1995)a. *Effect of temperature and moisture on the impact behaviour of graphite/epoxy composites; Part I - impact energy absorption.* J. COMPOS. TECHNOL. RES. **17**, 3-10.

Karasek M. L. Strait L. H. Amateau M. F. & Runt J. P. (1995)b. *Effect of temperature and moisture on the impact behaviour of graphite/epoxy composites; Part II - impact damage.* J. COMPOS. TECHNOL. RES. **17**, 11-16.

Kelly A. & Tyson W. R. (1965). *Tensile properties of fibre reinforced metals: copper-tungsten and copper-molybdenum.* J. MECH. PHYS. SOLIDS **32**, 329-350.

Khatri S. C. & Koczak M. J. (1996). *Thick-section AS4-graphite/E-glass/PPS hybrid composites: Part II. Flexural response.* COMP. SCI. TECHNOL. **56**, 473-482.

Komorowski J. P. Simpson D. L. & Gould R. W. (1990). *A technique for rapid damage detection with implication for composite aircraft structures.* COMPOSITES **21**, 169-173.

Lagace P. A. & Wolf E. (1995). *Impact damage resistance of several laminated material systems.* AIAA J. **33**, 1106-1113.

Lammerant L. & Verpoest I. (1996). *Modelling of the interaction between matrix cracks and delaminations during impact of composite plates.* COMP. SCI. TECHNOL. **56**, 1171-1178.

Lesser A. J. (1997). *Effect of resin crosslink density in the impact damage resistance of laminated composites.* POLYM. COMPOS. **18**, 16-27.

Levin K. & Jarlås R. (1997). *Vulnerability of embedded EFPI-sensors to low-energy impacts.* SMART. MATER. STRUCT. **6**, 369-383.

Liu D. (1988). *Impact induced delamination - a view of bending stiffness mismatching.* J. COMPOSITE MAT. **22**, 674-692.

Liu D. & Malvern L. E. (1987). *Matrix cracking in impacted glass/epoxy plates.* J. COMPOSITE MAT. **21**, 594-609.

Loewenstein K. L. (1983). *The manufacturing technology of continuous glass fibres: 2nd edition.* ELSEVIER.

Love J. D. & Winkler C. (1978). *Power attenuation in bent multimode step-index slab and fibre waveguides.* ELECTRON. LETT. **14**, 32-34.

Malki A. Gafsi R. Michel L. Lebarrere M. & Lecoy P. (1996). *Impact and vibration detection in composite materials by using intermodal interference in multimode optical fibers.* APPL. OPT. **35,** 5198-5201.

Mallick P. K. (1988). *Fiber-reinforced composites: materials, manufactureing and design.* MARCEL DEKKER.

Marsh D. M. (1959). *Tensile testing machine for microscopic specimens.* J. SCI. INSTR. **36,** 165-169.

Marsh D. M. (1961). *Micro-tensile testing machine.* J. SCI. INSTR. **38,** 229-234.

Measures R. M. Glossop N. D. W. Lymer J. Leblanc M. West J. Dubois S. Tsaw W. & Tennyson R. C. (1989). *Structurally integrated fibre optic damage assessment system for composite materials.* APPL. OPT. **28,** 2626-2633.

Mili M. R. Bouchaour T. & Merle P. (1996). *Estimation of Weibull parameters from loose-bundle tests.* COMP. SCI. TECHNOL. **56,** 831-834.

Moller K. O. (1988). *Optics.* UNIVERSITY SCIENCE BOOKS.

Neary T. E. Huston D. R. Wu J. & Spillman Jr. W. B. (1996). *In-situ damage monitoring of composite structures.* SPIE PROC. **2718,** 202-217

Nedele M. R. & Wisnom M. R. (1994)a. *Three-dimensional finite element analysis of the stress concentration at a single fibre break.* COMP. SCI. TECHNOL. **51**, 517-524.

Nedele M. R. & Wisnom M. R. (1994)b. *Stress concentration factors around a broken fibre in a unidirection carbon fibre-reinforced epoxy.* COMPOSITES **26**, 549-557.

Netravali A. N. Topoleski L. T. T. Sachse W. H. & Phoenix S. L. (1989). *An acoustic emission technique for measuring fiber fragment length distributions in the single-fiber-composite test.* COMP. SCI. TECHNOL. **35**, 13-29.

Noharet B. Chazelas J. Bonniau P. Lecuellet J. & Turpin M. (1995). *Impact detection on airborne multilayered structures.* SPIE PROC. **2444**, 460-467.

Ochiai S. Schulte K. & Peters P. W. M. (1991). *Strain concentration factors for fibers and matrix in unidirectional composites.* COMP. SCI. TECHNOL. **41**, 237-256.

Okafor A. C. Chandrashekhara K. & Jiang Y. P. (1995). *Damage detection in composite laminates with built-in piezoelectric devices using modal analysis and neural network.* SPIE PROC. **2444**, 314-325.

Okafor A. C. Chandrashekhara K. & Jiang Y. P. (1996). *Location of impact in composite plates using waveform-based acoustic emission and Gaussian cross-correlation techniques.* SPIE PROC. **2718**, 291-302.

Owen Jr. G. E. (1981). *A comparison of impact tests for assessment of fiberglass reinforced plastic toughness.* POLYM. ENG. SCI. **21**, 467-473.

Pan N. Chen H. C. Thompson J. Inglesby M. K. Khatua S. Zhang X. S. & Zeronian S. H. (1997). *The size effects on the mechanical behaviour of fibres.* J. MAT. SCI. **32**, 2677-2685.

Pavier M. J. & Clarke M. P. (1995). *Experimental techniques for the investigation of the effects of impact damage on carbon fibre composites.* COMP. SCI. TECHNOL. **55**, 157-169.

Pierce S. G. Philp W. R. Culshaw B. Gachagan A. McNab A. & Hayward G. (1996)a. *Ultrasonic inspection of CFRP plates using surface bonded optical fibre sensors.* SPIE PROC. **2718**, 345-354.

Pierce S. G. Philp W. R. Culshaw B. Gachagan A. McNab A. Hayward G. & Lecuyer F. (1996)b. *Surface-bonded optical fibre sensors for the inspection of CFRP plates using ultrasonic Lamb waves.* SMART. MATER. STRUCT. **5**, 776-787.

Richardson M. O. W. & Wisheart M. J. (1996). *Review: Review of low-velocity impact properties of composite materials.* COMPOSITES PART A **27A**, 1123-1131.

Rosen B. W. (1964). *Tensile failure of fibrous composites.* AIAA J. **2**, 1985-1991

Scarponi C. & Briotti G. (1997). *Ultrasonic detection of delaminations on composite materials.* J. REINF. PLAST. COMP. **16**, 768-790.

Schindler P. M. May R. G. Claus R. O. & Shaw J. K. (1995). *Location of impacts on composite panels by embedded fiber optic sensors and neural network processing.* SPIE PROC. **2744**, 481-489.

Scott I. G. & Scala C. M. (1982). *A review of non-destructive testing of composite materials.* NDT INT. **April**, 75-86.

Seo D. C. & Lee J. J. (1995). *Effect of embedded optical fiber sensors on transverse crack spacing of smart composite structures.* COMPOSITE STRUCT. **32**, 51-58.

Shaw I. K. Sirkis J. S. Freibele E. J. Jones R. T. & Kersey A. D. (1995). *Model of transverse plate impact dynamics for design of impact detection methodologies.* AIAA J. **33**, 1327-1334.

Shelley T. (1996). *Low cost eddies find defects in composites.* EUREKA **October**, 12-13.

Shioya M. and Takaku A. (1995). *Estimation of fibre and interfacial shear strength by using a singl-fibre composite.* COMP. SCI. TECHNOL. **55**, 33-39.

Sirkis J. S. Chang C. C. & Smith B. T. (1994). *Low velocity impact of optical fiber embedded laminated*

graphite/epoxy panels. Part I: Macro-scale. J. COMPOSITE MAT. **28**, 1347-1369.

Sirkis J. S. & Chang C. C. (1994). *Low velocity impact of optical fiber embedded laminated graphite/epoxy panels. Part II: Micro-scale.* J. COMPOSITE MAT. **28**, 1532-1552.

Sirkis J. S. & Lu I. P. (1995). *On interphase modeling for optical fiber sensors embedded in unidirectional composite systems.* J. INTELL. MAT. SYS. STRUCT. **6**, 199-209.

Sirkis J. S. & Singh H. (1994). *Moire analysis of thich composites with embedded optical fibres.* EXP. MECH. **December**, 300-305.

Sjobolm P. O. Hartness J. T. & Cordell T. M. (1988). *On low-velocity impact testing of compsite materials.* J. COMPOSITE MAT. **22**, 30-52.

Smith G. C. (1991). *Quantitative surface analysis for materials science.* INSTITUTE OF METALS.

Smith R. A. (1994). *Ultrasonic defect sizing in carbon-fibre composites - an initial study.* INSIGHT **36**, 595-604.

Smith I. C. & Hoa S. V. (1994). *Utilization of PVDF sensors to determine impact damage in graphite/epoxy plates by acousto-ultrasonic technique.* J. REINF. PLAST. COMP. **13**, 111-127.

Synder A. W. & Mitchell D. J. (1973). *Generalised Fresnel's law for loss due to curvature.* ELECTRON. LETT. **9**, 609-610.

Snyder A. W. & Mitchell D. J. (1974). *Bending losses of multimode optical fibres.* ELECTRON. LETT. **10**, 11-12.

Sohn M. S. & Hu X. Z. (1995). *Comparitive study of dynamic and static delamination behaviour of carbon fibre/epoxy composite laminates.* COMPOSITES **26**, 849-858.

Tan K. S. Guo N. Wong B. S. & Tui C. G. (1995). *Comparison of Lamb waves and pulse echo in detection of near-surface defects in laminate plates.* NDT&E INT. **28**, 215-223.

Throckmorton P. E. Hickman H. M. & Browne M. F. (1963). *Origin of stress failure in glass reinforced plastics.* MOD. PLAST. **November**, 140-150, 189-193, 198.

Tsai S. W. & Hahn H. T. (1980). *Introduction to composite materials.* TECHNOMIC.

Udd E. (1991). *Fibre optic sensors, an introduction for engineers and scientists.* WILEY INTERSCIENCE.

van den Heuvel P. W. J. Peijs T. & Young R. J. (1997). *Failure phenomena in two-dimensional multi-fibre microcomposites: 2. A Raman spectroscopic study of the influence of inter-fibre spacing on stress concentrations.* COMP. SCI. TECHNOL. **57**, 899-911.

Varelas D. Limberger H. G. Salathe R. P. & Kotrosios C. (1997). *UV-induced mechanical degradation of optical fibres.* ELECTRON. LETT. **33**, 804-806.

Vavilov V. Maldague X. Dufort B. Robitaille F. & Picard J. (1993). *Thermal non-destructive testing of carbon epoxy composites: detailed analysis and data processing.* NDT&E INT. **26**, 85-95.

Wagner H. D. Amer M. S. & Schadler L. S. (1984). *A study of statistical variability in the strength of single aramid filaments.* J. COMPOSITE MAT. **18**, 312-338.

Wagner H. D. & Eitan A. (1990). *Interpretation of the fragmentation phenomenon in single-filament composite experiments.* APPL. PHYS. LETT. **56**, 1965-1967.

Wagner H. D. & Eitan A. (1993). *Stress concentration factors in two-dimensional composites: Effects of material and geometrical parameters.* COMP. SCI. TECHNOL. **46** 353-362.

Wagner H. D. Phoenix S. L. & Schwartz P. (1996). *Fibre interactions in two-dimensional composites by micro-Raman spectroscopy.* J. MAT. SCI. **31**, 1165-1173.

Weibull W. (1951). *A statistical distribution function of wide applicability.* J. APP. MECH. **September**, 293-297.

Wiggenraad J. F. M. Aoki R. Gadke M. Greenhalgh E. Hachenberg D. Wolf K. & Bubl R. (1996). *Damage propagation*

in composite structural elements - analysis and experiments on structures. COMPOSITE STRUCT. **36**, 173-186.

Wilson D. M. (1997). *Statistical tensile strength of Nextel™ 610 and Nextel™ 720 fibres.* J. MAT. SCI. **32**, 2535-2542.

Wisnom M. R. & Green D. (1995). *Tensile failure due to interaction between fibre breaks.* COMPOSITES **26**, 499-508.

Woo E. M. & Chen J. S. (1995). *Instrumented impact evaluation of a toughened carbon fibre epoxy composite.* POLYM. ENG. SCI. **35**, 129-136.

Wooh S. C. & Daniel I. M. (1994). *Three-dimensional ultrasonic imaging of defects and damage in composite materials.* MATER. EVAL. **October** 1199-1206.

Wu E. & Liau J. (1994). *Impact of unstitched and stitched laminates by line loading.* J. COMPOSITE MAT. **28**, 1640-1658.

Wu H. Y. T. & Springer S. (1988). *Measurement of matrix cracking and delamination caused by impact on composite plates.* J. COMPOSITE MAT. **22**, 518-532.

Xian X. J. & Choy C. L. (1994). *Impact resistance and damage evaluation of carbon fibre reinforced modified bismaleimide composites.* J. REINF. PLAST. COMP. **13**, 1135-1153.

Yariv A. (1991). *Optical Electronics-4th Edition.* SANDERS COLLEGE PUBLISHERS.

Zhu Y. T. Blumenthal W. R. Taylor S. T. & Lowe T. C. (1997). *Analysis of size dependence of ceramic fiber and whisker strength.* J. AM. CERAM. SOC. **80**, 1447-1452.

Zweben C. (1968). *Tensile failure of fiber composites.* AIAA J. **6**, 2325-2331.

Appendix A. Publications arising from this work

1. Hayes S. Liu T. Brooks D. Monteith S. Vickers S. & Fernando G. F. *A novel self-sensing optical fibre reinforced composite.* Applied optics and opto-electronics, Institute of Physics, Reading, 456-470 Sept (1996).

2. Hayes S. Brooks D. Liu T. Vickers S. & Fernando G. F. *A novel self-sensing reinforcing fibre light guide.* Journal of Smart Materials and Structures, 6, 432-440 (1997).

Part of this work was presented at the SPIE conference on smart materials in San Diego (1996) as: Hayes S. Brooks D. Liu T. Vickers S. & Fernando G. F. *In-situ self-sensing fibre reinforced composites.* SPIE proceedings: Smart Sensing, Processing and Instrumentation, 2718, 408-416 (1996).

3. Doyle C. Martin A. Liu T. Hayes S. Crosby P. A. Brooks D. Badcock R. A. & Fernando G. F. *In-situ process and condition monitoring of advanced fibre reinforced composite materials using optical fibre sensors.* Journal of Smart Materials and Structures Special issue: Fibre Optic Structural Sensing. 7, 145-158 (1998).

Part of this work was presented at the SPIE conference on smart materials in Beijing (1996) as: Doyle C. Martin A. Wu M. Liu T. Hayes S. Brooks D. Badcock R. A. & Fernando G. F. *Intensity-based optical fibre sensors for condition monitoring of*

engineering materials. SPIE proceedings, 2895, 288-299 (1996).

4. Zolfagar K. Khan N. Brooks D. Hayes S. Liu T. & Fernando G. F. *Self-sensing fibre reinforced composites.* (Invited Paper) SPIE Far East & Pacific Rim Symposium on Smart Materials, December 11-14, Bangalore (1996) (Not yet published)

Paper 1

PAGE

NUMBERING

AS ORIGINAL

A novel self-sensing optical fibre reinforced composite

S. Hayes, D. Brooks, T. Liu, S. Vickers & G. F. Fernando*

Department of Materials Engineering, Brunel University, Uxbridge, Middlesex, UB8 3PH. U.K.

*To whom correspondence should be addressed.

Abstract. This paper reports on the design and development of a novel class of advanced fibre reinforced composite (AFRC) where some of the reinforcing fibres act as the light guide. This class of fibres have been termed 'self-sensing fibres' and composites manufactured incorporating the self-sensing fibres have been termed 'self-sensing composites'. The self-sensing fibres were embedded within a 16-ply carbon fibre reinforced epoxy composite. The feasibility of using these fibres for impact damage detection was successfully demonstrated.

1. Introduction

The detection of impact damage in AFRC structures is of significant interest especially in cases where these materials are used for load bearing applications [1]. Impact damage can drastically reduce the mechanical and structural integrity of AFRCs [2]. Unlike conventional engineering materials, it is often very difficult to detect low velocity impact damage in AFRC structures [3]. A number of optical fibre sensor systems have been demonstrated as being suitable for damage detection in AFRCs. Conventional optical fibres have outer diameters in the range 125-230 μm, whereas reinforcing fibres have outer diameters in the range of 7-12 μm. The use of large diameter optical fibres can result in the introduction of fibre waviness in the reinforcing fibres. Fibre waviness has been shown to reduce the compressive properties of AFRCs [4,5,6]. Conventional optical fibre sensors such as Bragg gratings, interferometric sensors etc. can not be readily incorporated into AFRC manufacturing processes. The costs associated with these sensor systems also tends to prohibit their use in mass produced AFRC components, e.g., filament wound pressure vessels. A potential solution to theses problems is to use the reinforcing fibre as the optical sensing medium. The self-sensing composite is ideal for applications where it is necessary to know if a specified load/strain threshold has been exceeded, rather than, requiring information on the magnitude of the load or strain. The reinforcing fibre system used in this study were commercially available (Quartzel) 11 μm high purity silica fibres. These fibres have a low dielectric constant, offer high heat resistance and a high resistance to thermal shock. As a consequence of this, they are used extensively in the aircraft industry for radomes, electromagnetic windows and thermal insulation applications.

2. Experimental

2.1 Production of the self-sensing composites

The Quartzel fibres were donated by Quartz ET Silice, France. The fibre tows contained approximately 400 individual filaments. The fibres tows were desized at 700°C in an electric furnace and upon cooling to ambient temperature, a silicone resin (cladding) was applied to the Quartzel fibres. The Quartzel 'optical fibres' were then placed in-between the outer two plies of a 16 layered cross-ply $[0,90,90,0,0,90,0,90]_S$ composite. The optical fibre bundles were located at a spacing of 10 mm. The prepreg system used was T300/920 (carbon fibre reinforced epoxy) as supplied by Ciba-Geigy. Composites without any embedded optical fibres were also manufactured for comparison purposes. The composites were autoclaved using the manufacturer's recommended cure schedule. The cured composite panels were cut into 70 mm squares, c-scanned and then dried in an air-circulating oven at 60°C for three days. The test specimens were then stored in a desiccator until required.

2.2 Light intensity measurements

After the coating operation, the attenuation characteristics of the Quartzel optical fibres were evaluated using a Photon Kinetics FOA-1000 universal fibre optics analyser. The transmission loss of the self-sensing fibres were measured using the cut-back method.

The intensity of light transmitted through each embedded optical fibre bundle was measured before and after impact. This was achieved using the experimental arrangement illustrated in Figure 1. Here the composite panel was clamped on to an X-translation stage which moved the panel between a white light source and a visible light enhanced photodiode. The signal output from a custom made Access Pacific photodiode amplifier gave the transmitted intensity through the fibres. The position of the optical fibre bundle was measured using a linear variable displacement transducer.

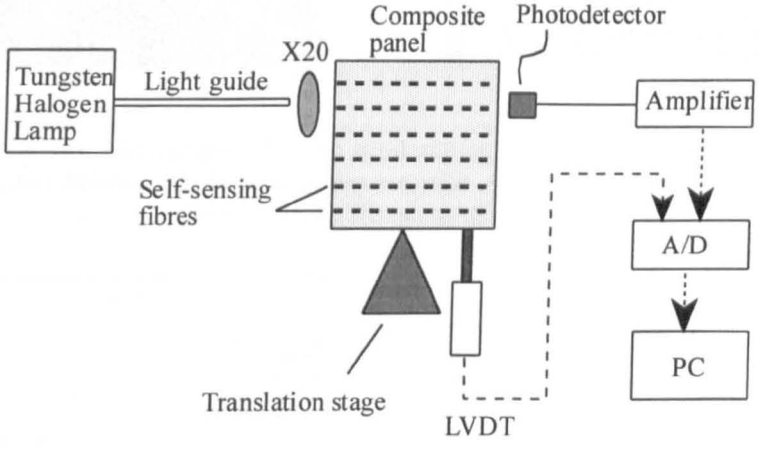

Figure 1 Experimental set-up for the optical intensity measurements through the embedded Quartzel optical fibres.

2.3 Introduction of impact damage

The composite panels were impacted on Rosand Instrumented falling-weight impact testing machine at 2 J, 4 J and 6 J using a 10 mm hemispherical tup. The specimens were c-scanned again after the impact trials and the light transmission intensity through the embedded optical fibre bundles were re-measured.

3. Results and discussion

3.1 Quality of the Quartzel optical fibres

The burn-off and coating process which were used in the current trials resulted in significant fibre fractures. The difficulties associated with obtaining a high quality coating are illustrated in Figures 2 (a and b). Figure 2 (a) illustrates the case where a reasonable coating quality was obtained and Figure 2 (b) shows a region with a poor coating quality. Attempts are currently being made to spread the fibres prior to the coating operation. A range of low viscosity resins are also being investigated to improve the penetration of the resin into the fibre bundle. A previous study on the effectiveness of the burn-off treatment to remove the 'size' (coating applied to the fibres at the time of manufacture to protect the fibre from damage) indicated the presence of contaminants in the form of carbides on the fibre surface [7]. Therefore, the high attenuation characteristics exhibited by the current set of Quartzel fibres as shown in Figure 3 is understandable. Improvements to the optical fibre quality is being addressed through the use of un-twisted fibre tows and a dual-desizing process. Here the fibre size will initially be removed using an acidic solution followed by the burn-off as described previously [7]. An automated coating process will be used in future studies to improve the quality and the consistency of the coating process.

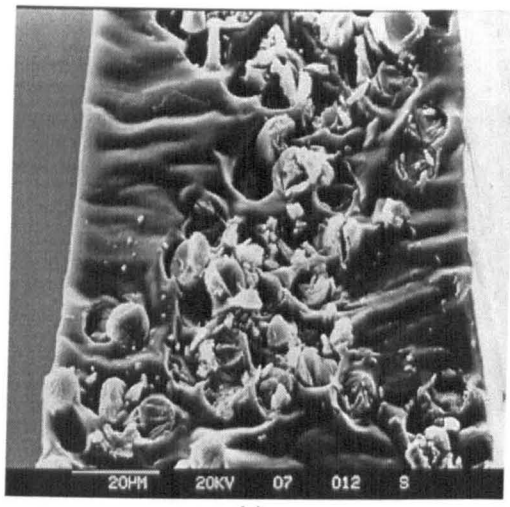

(a)

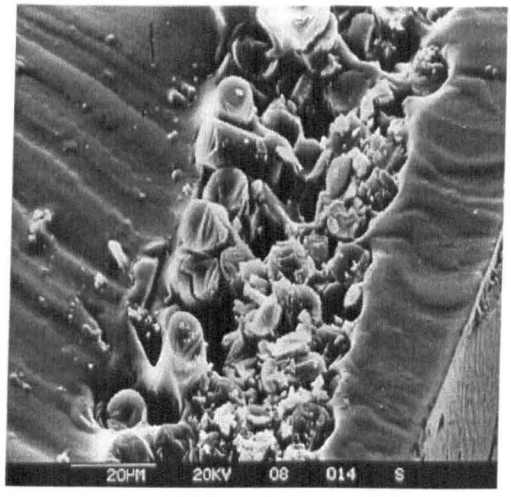

(b)

Figures 2 (a and b): (a) Micrograph indicating good wetting and penetration by the silicone resin into the fibre bundle; (b) Micrograph showing poor penetration of the silicone resin. Note also the surface damages on the fibres due to cleaving.

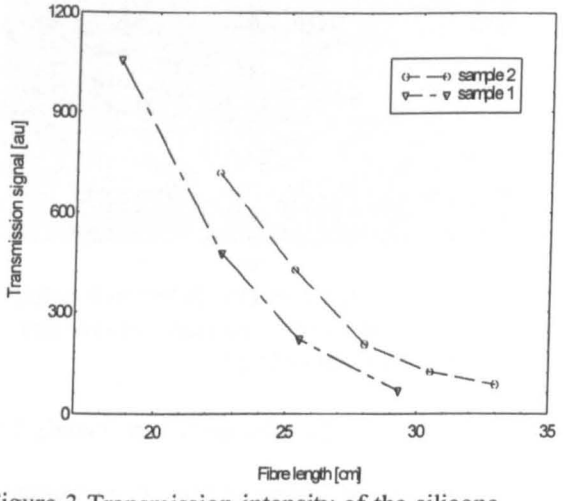

Figure 3 Transmission intensity of the silicone coated self-sensing fibres.

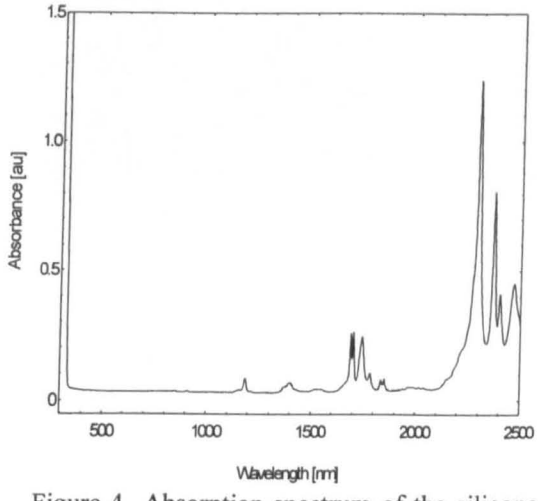

Figure 4 Absorption spectrum of the silicone resin. A path length of 2 mm was used.

Figure 4 illustrates the absorption spectrum for the silicone resin obtained using a PERKIN ELMER Lamda 19 UV/VIS/NIR spectrometer. Figure 4 showed that no significant absorption took place between 400 and 1600 nm.

The quality of the cleave can also play an important role in the efficiency of the light coupling into the Quatrzel optical fibres. The difficulties associated with obtaining a good cleave are readily apparent in Figures 5 (a and b). A brief study was under taken to investigate the influence of applied tension on the fibres during the cleaving operation. The fibre tows were subjected to a radius of known curvature and then cleaved using a sharp blade. The introduction of a high tensile load on the fibres proved beneficial in obtaining a clean fracture surface, see Figure 5 (a). When the fibre was under a lower tensile or compressive load, a poor quality of cleave was obtained, see Figure 5 (b). Research is continuing to establish the optimum approach to cleaving these fibres. The quality of the cleave was not an issue when the self-sensing fibres were embedded in the composite because the launch and detection-ends were polished, see Figure 6 (a). With reference to Figures 6 (b) the mismatch between the reinforcing fibres and the optical fibre (50/125) and the presence of a resin rich region are clear.

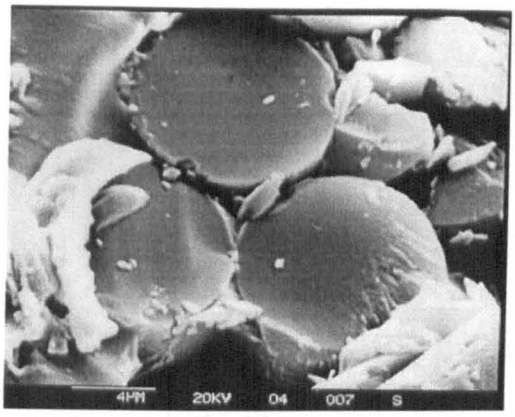

(a)

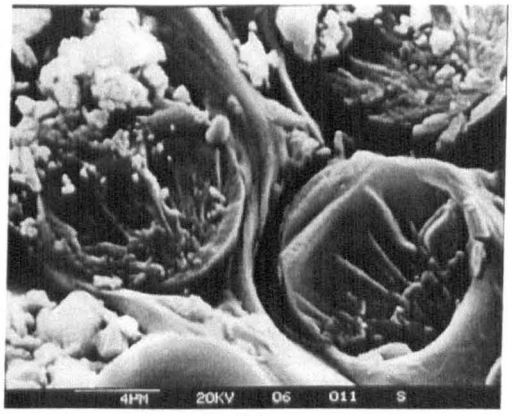

(b)

Figures 5 (a and b): (a) Micrograph showing reasonable quality cleaves when the fibres were cleaved under a high tensile load; (b) Micrograph showing poor quality cleaves when the fibres were cleaved under low tensile or compressive loads.

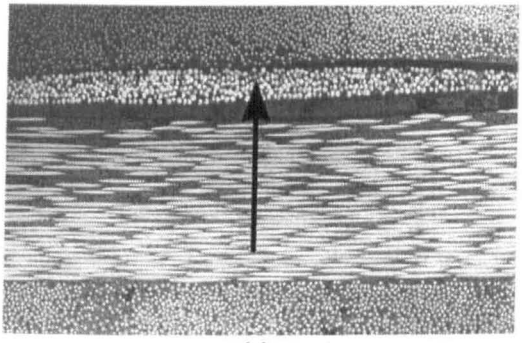

(a)

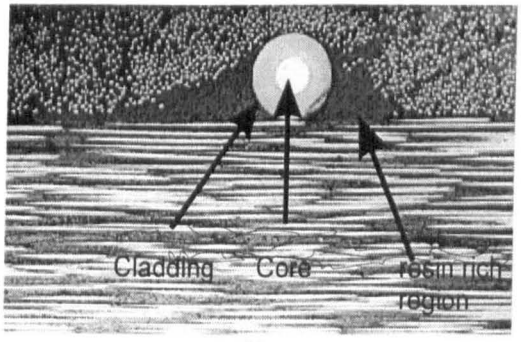

(b)

Figures 6 (a and b): (a) Micrograph of a polished section from the self-sensing composite. The arrow indicates the location of the embedded self-sensing fibre bundle; (b) Micrograph of an embedded 50/125 multimode optical fibre in a carbon/epoxy composite.

3.2 Detection of impact damage

Figures 7 (a-c) illustrate typical c-scans for the self-sensing composites which were impacted at 2 J, 4 J and 6 J. The white vertical stripes represent the location of the Quartzel optical fibres and the white regions marked (x) represent the extent of the delamination as a consequence of the impact. The extent of the delaminations was found to increase with increasing incident impact loads. It is not clear at this stage if the presence of the self-sensing fibres influenced the extent and/or the nature of the delaminations. For example, Figure 7 (c) indicated that delaminations had taken place in the self-sensing fibre direction. This is understandable because of the poor affinity between the fully cured silicone resin and the epoxy matrix. However, co-curing the two resin systems will enhance the interfacial bonding.

Figures 8 (a and b) illustrate the light transmission characteristics of the composite panels before and after impact at 2 J for the impacted surface and the opposite side respectively. The data for the 4 J was not included as it showed a similar behaviour to the samples which were impacted at 2 J. Figures 9 (a and b) show the light transmission characteristics of the composite panels before and after a 6 J impact. The decrease in the light intensity after the impact event was clearly seen in all cases. There was some indication from Figure 9 (a) that the self-sensing fibre bundle which was located to the left of the primary impact zone also sustained some damage. This observation is also verified by the c-scan shown in Figure 7 (c). It is proposed that the nature of the coating, the depth of the embedment and the type of coating can be selected to optimise the sensitivity of the impact damage detection system.

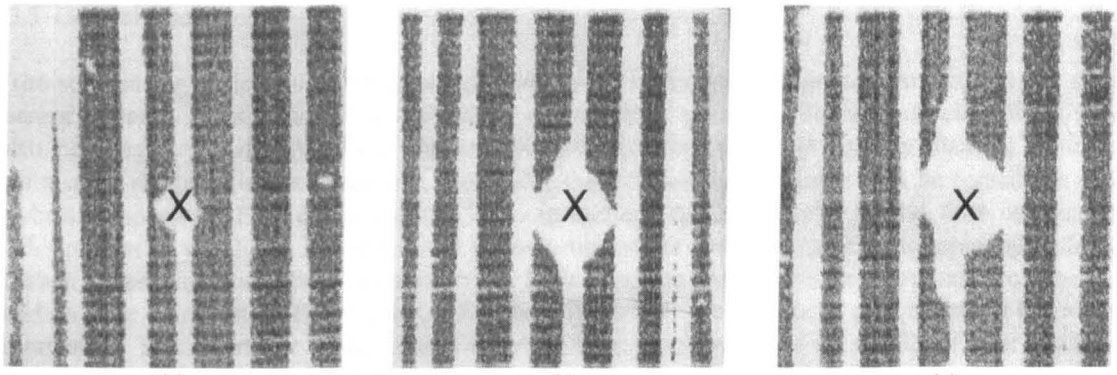

(a) (b) (c)

Figures 7 (a, b and c): C-scans for the self-sensing composites subjected to a 2 J, 4 J and 6 J impact respectively. The delaminated region is marked with a (x).

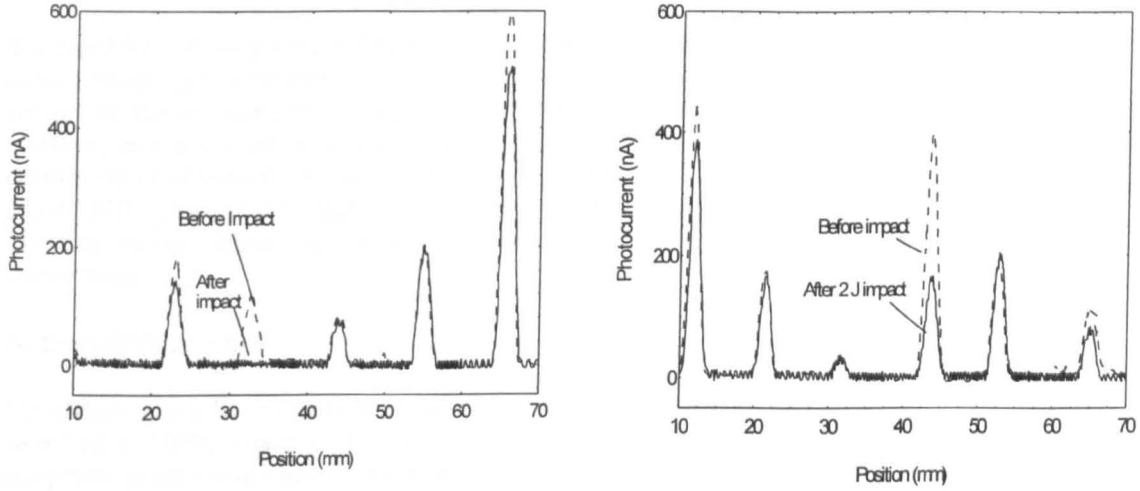

(a) (b)

Figures 8 (a and b): Optical transmission intensity through the self-sensing fibres before a 2 J impact: (a) the impacted surface and (b) the opposite side of the impacted surface.

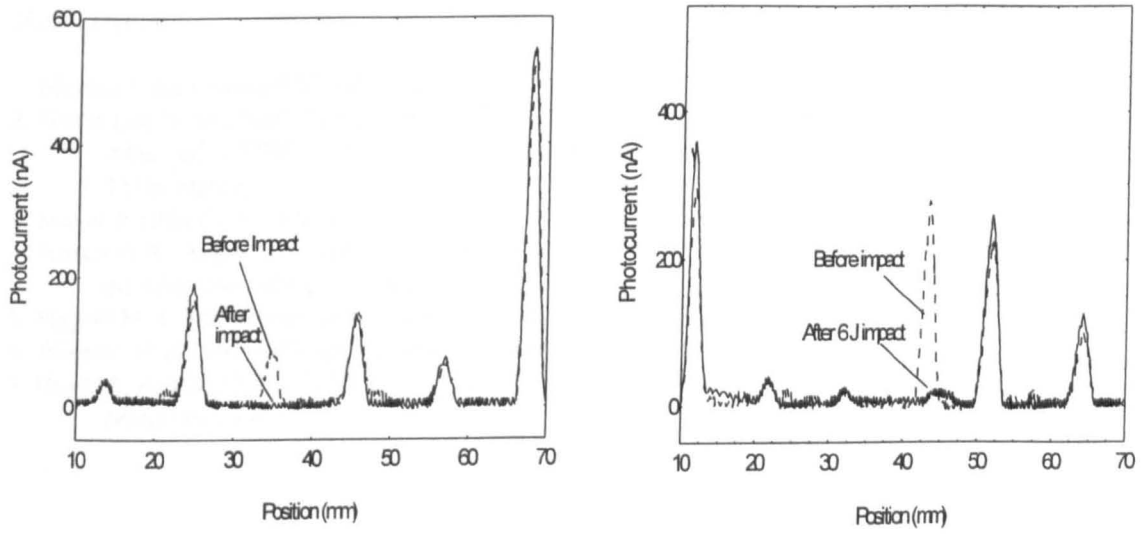

(a) (b)

Figures 9 (a and b): Optical transmission intensity through the self-sensing fibres before a 6 J impact: (a) the impacted surface and (b) the opposite side of the impacted surface.

3.3 General discussion

The self-sensing optical fibre reinforced composites offer advantages over conventional optical fibre sensor systems. Firstly, since the self-sensing optical fibres are conventional reinforcing fibres, they can be integrated into any AFRC preforms or manufacturing processes such as filament winding, pultrusion, pre-pregging and weaving. Secondly, the self-sensing composites can be considered as a hybrid composite (AFRC containing two or more reinforcing fibre types). Hybrid fibre composites offer properties which can not be realised by their mono-fibre counterparts. For example, hybridising carbon fibres with glass fibres has been shown to improve the impact resistance compared to a mono-carbon fibre composite. Thirdly, the self-sensing fibres will permit a large area of the AFRC to be monitored. This is a major limitation of the current range of conventional optical fibre sensor systems. It is proposed that the cladding material can be selected to sense a range of other parameters, for example, diffusion of fluids into the composite.

4. Conclusions

The feasibility of using the reinforcing fibres as the light guide was successfully demonstrated. These optical fibres were embedded within a carbon fibre composite and were used as a crack-detection sensor. In the current programme, 150 cm long self-sensing fibres were successfully produced, however, they could not be produced on a consistent basis. It is proposed that the light transmission characteristics of these fibres can be improved by reducing the extent of fibre breakage, improving the quality of the cleave and by improving the coating process. The self-sensing composite was capable of detecting incident impacts as low as 2 J within and at a distance of 10 mm away from the primary impact zone.

Acknowledgements

The authors would like to thank the EPSRC for CASE studentships for D. Brooks and S Hayes, and the award of a ROPA award to T. Liu. G. Fernando acknowledges the receipt of a Royal Society equipment grant for the development of the sensor. The authors would like to thank Professors P. Curtis, B. Ralph, Drs. S. Hitchen, M. Kemp and J. Coleman of the DRA and J. Harry of QUARTZ ET SILICE for supporting the research programme. The assistance given by Dr. K Hale, S. Knowles and J. Moses are duly acknowledged.

References

1 Morton J and Cantwell W 1991 *Composites* **22** (5) 347-362
2 Gause Lee W and Buckley Leonard J 1987 *Instrumented Impact Testing of Plastics and Composite Materials ASTM STP 936* Kessler S L, Adams G C, Driscoll S B and Ireland D R ed. (ASTM Philadelphia)
3 Meyer P 1988 *Composite Science and Technology* **33** 279-293
4 Jensen D W, August J A and Pascual J 1992 *Active Materials and Adaptive Structures* Knowles G J ed. (IOP Publishing Ltd, Bristol and Philadelphia)
5 Piggott M R 1995 *Composites Science and Technology* **53** 202-205
6 Wisnom M R 1994 *J. Composite Materials* **28** 1 66-76
7 Hayes S, Brooks D, Liu T, Vickers S and Fernando G F *SPIE Proceeding Smart Structures and Materials 1996*

Paper 2

Smart Mater. Struct. 6 (1997) 432–440. Printed in the UK PII: S0964-1726(97)82362-2

In situ self-sensing fibre reinforced composites

S Hayes, T Liu, D Brooks, S Monteith, B Ralph, S Vickers and G F Fernando†

Department of Materials Engineering, Brunel University, Uxbridge, Middlesex, UK

Received 15 October 1996, accepted for publication 24 January 1997

Abstract. This paper discusses the development of a novel composite system in which some of the reinforcing fibres act as the light guide. The reinforcing fibre light guide was made by applying an appropriate cladding material onto commercially available 9 μm diameter silica fibres. The resultant light guide was termed a 'self-sensing' fibre. The self-sensing fibres were embedded within a 16-ply carbon fibre reinforced epoxy prepreg system and cured to produce a composite panel. The composite panels were impact tested to investigate the feasibility of using the self-sensing fibres as an impact damage sensor system. Similarly, three types of conventional optical fibre, with outer diameters of 30, 50 and 125 μm respectively, were also embedded within composite panels. The results indicated that the self-sensing fibres were capable of detecting impact damage as low as 2 J for impacts carried out using a 20 mm hemispherical tup. The self-sensing fibres proved more sensitive to impact damage than the conventional optical fibres used in this study.

1. Introduction

A number of optical-fibre-based sensor (OFS) systems have been used for inferring the structural integrity of advanced fibre reinforced composites (AFRCs). The sensor designs include Bragg gratings [1, 2], Fabry–Pérot [3] and intensity-based [4, 5] optical fibre sensors. In terms of costs, the intensity-based OFS techniques tend to be significantly cheaper than interferometric techniques. In cases where the absolute values of temperatures and strains are not required, intensity-based health monitoring techniques can offer a cost effective means of monitoring the structural integrity of AFRCs. However, from an AFRC design viewpoint, there is a significant mismatch in the diameter of optical fibre sensors and the reinforcing fibres in the composite. The diameters of the optical fibres are generally in the range of 125–230 μm, whereas the reinforcing fibres (such as carbon and glass fibres) usually have a diameter in the range of 7–12 μm. The effect of this diameter mismatch is not apparent when the composite is subjected to tensile mechanical testing, but it can be detrimental when the material is subjected to long-term dynamic compressive and/or tension/compression loading. This diameter mismatch also makes it difficult to integrate a large number of OFSs into the composite. Furthermore, the integration of the OFS into composite preforms such as prepregs or woven fabrics is currently difficult to achieve at a continuous production level.

A possible solution to the above mentioned diameter mismatch between the optical fibre and the reinforcing fibres is to use the reinforcing fibres as a light guide. Conventional E-glass fibres are not suitable for transmitting light over long distances; however, quartz reinforcing fibres which are commercially available are ideal for this application. These fibres have a low dielectric constant, offer high heat resistance and a high resistance to thermal shock. As a consequence of this, they are used extensively in the aircraft industry for radomes, electromagnetic windows and thermal insulation applications. The term 'self-sensing fibres' is used in the following text to describe the appropriately coated quartz fibres which then act as a light guide. The term 'self-sensing composites' refers to the situation where the self-sensing fibres are embedded in the composite. The self-sensing composite is ideal for applications where it is necessary to know if a specified load/strain threshold has been exceeded rather than requiring information on the magnitude of the load or strain.

2. Experimental details

2.1. Selection of reinforcing fibre light guide and cladding material

With reference to table 1, the commercially available Quartzel fibres were identified as a suitable candidate to prove the concept of the reinforcing fibre light guide as they have comparable mechanical properties to conventional E-glass fibres. A selection of the cladding materials which were initially evaluated for this programme is presented in table 2 along with relevant properties of interest.

† To whom correspondence should be addressed.

0964-1726/97/040432+09$19.50

Table 1. Specified properties for selected fibre types.

Property	Quartzel	E-Glass	S-Glass	PMMA	Optical[a]
Diameter (μm)	9	12	9	250–3000	125
Coefficient of thermal expansion ($\times 10^{-6}$)	0.54	5	4	260	0.54
Refractive index (589 nm: 23 °C)	1.4585	1.547	1.524	1.492	1.46
Young's modulus (GN m^{-2})	73	76	86	3.3	73.1
Tensile strength (GN m^{-2})	3.6	3.2	4.4		3.6
Maximum service temperature (°C)	1050	650	700	100	600

[a] Optical refers to typical commercially available 50/125 multimode optical fibres.

Table 2. Selected properties for potential cladding materials.

Property	OG135[a]	Sylgard 182[b]	THV200P[c]
Polymer type	Epoxy	Silicone	Fluoro
Refractive index (589 nm: 23 °C)	1.45	1.41	1.35
Coefficient of thermal expansion ($\times 10^{-6}$)	58	96	—
Young's modulus (GN m^{-2})	—	0.006	0.006
Cure time and temperature	150 °C/1 h	150 °C/15 min	solvent cast
Maximum service temperature (°C)	395	200	330

[a] Epoxy Technologies.

[b] Dow Corning.

[c] 3M.

2.2. De-sizing and surface analysis

The term de-sizing is used to describe the situation where the coating (size) which was applied to the reinforcing fibres at the time of manufacture is removed. The fibres were coated with a proprietary organic 'size' at the time of manufacture to protect the fibres from abrasion damage during production. The fused quartz fibres were donated by Quartz et Silice in the form of a continuous fibre bundle consisting of approximately 400 individual filaments. The following experiments were carried out to investigate the optimum de-sizing conditions. (i) Refluxing the fibres in an acetic acid solution with a pH of four for a period of 3 h at 95 °C. The de-sized fibres were then washed with deionized water to remove any residual acetic acid from the fibres. (ii) Pyrolysis of the as-received fibres in a tube furnace at 700 °C in air. With reference to the pyrolysis experiments, two heating regimes were investigated, namely (a) heating the fibres from ambient to 700 °C using a heating rate of 10 °C min^{-1} and (b) introducing the fibres directly to the furnace which was set at 700 °C. These two heating regimes are referred to as slow and fast respectively.

The surface of the Quartzel fibres was inspected using scanning electron microscopy (SEM) and x-ray photoelectron spectroscopy (XPS). The SEM samples were secured onto mounting stubs with double-sided tape and then sputter coated with gold. The XPS test specimens were prepared just prior to the analysis. Due care and attention was paid to avoid any contamination of the fibre surfaces.

2.3. Coating (cladding) the reinforcing fibres

The silicone resin (Sylgard 182) was prepared by mixing the base resin and the hardener in the required proportions of 10:1 by weight of resin to hardener. The coated fibres were first passed between a pair of rollers and then drawn through a furnace which was set at 150 °C. The draw rate was 15 mm min^{-1}. The thickness of the resultant self-sensing fibre bundle was approximately 70 μm.

2.4. Light transmission characteristics of the self-sensing fibres

The attenuation characteristics of the Quartzel optical fibres were evaluated after the coating operation using a Photon Kinetics FOA-1000 universal fibre optics analyser. The transmission loss of the self-sensing fibres was measured using the cut-back method. Experiments were also conducted to investigate the best way to cleave the self-sensing fibres.

2.5. Production of the self-sensing composites

The composite panels were produced from Ciba–Geigy T300/920 carbon fibre prepregs. A vacuum-assisted hand lay-up technique was used to produce 300 mm square panels with a ply sequence of 16 plies in the sequence $\{0, 90, 90, 0, 0, 90, 0, 90\}_s$. The conventional optical fibres and the self-sensing fibres were introduced between plies 1 and 2 and plies 15 and 16 at a spacing of 10 mm. Five categories of composites were manufactured:

(i) reference composite with no optical fibre embedment;

(ii) self-sensing composite;

(iii) composite containing (conventional) embedded 125 μm optical fibres;

(iv) composite with (custom made) embedded 50 μm optical fibres;

(v) composite with (custom made) 30 μm embedded optical fibres.

In the case of the 125 μm optical fibres and the self-sensing fibres, a single fibre and a coated fibre bundle respectively were laid each time. In the case of the 50 μm optical fibres a small bundle of 8 to 14 fibres was laid. For the 30 μm optical fibres, the whole 200-fibre bundle was laid each time. The panels were cured in an autoclave using the manufacturer's recommended cure schedule. The cured panels were C-scanned as a quality check and then cut into 70 mm squares. The test specimens were dried in an air-circulating oven at 60 °C for three days and stored in a desiccator until required for impact testing.

2.6. Light intensity measurement and impact testing

The intensity of the light transmission through each optical fibre was measured prior to conducting the impact tests. This was achieved by clamping the test panel on to an X-travel stage. A schematic illustration of the experimental set-up is shown in figure 1. The reproducibility of the light transmission measurements was investigated by repeating each test three times with the panel being removed and reclamped between each test. The panel, white light source and visible light enhanced silicon photodiode were fixed in the Y- and Z-planes: this allowed the panel to be scanned in the X-plane using the travel stage. A custom built Access Pacific photodiode amplifier, sensitive to photocurrent in the range 100 pA to 10 nA, was used to assess the light transmission characteristics of the embedded self-sensing fibres. The test specimen was screened to prevent stray light reaching the photodiode other than by passing through the upper row of fibres. This was achieved by baffles positioned above and below the clamping frame. A linear variable displacement transducer (LVDT) was used to identify the position of the self-sensing fibres along the panel. The data from the photodiode amplifier and the LVDT were captured to a computer with a Data Translation data acquisition board and a custom written data acquisition program using DT-Vee software. Each panel was tested and then turned over to allow examination of the self-sensing fibres located on the opposite side of the composite panel.

The test specimens were impacted on a Rosand Instrumented Impact Tester using a 20 mm hemispherical tup. Two test specimens per composite type were impacted at impact energies of 2, 4, 6 and 8 J. One test specimen per composite type was impacted at 10 J. After impact the light intensity was measured as described in the previous paragraph and subsequently the panels were also C-scanned after impact testing to establish the extent of delamination.

3. Results and discussion

3.1. De-sizing and surface analysis

Figures 2(a) and (b) show SEM micrographs of the surface of the self-sensing fibres before and after burn-off. It is apparent from the figure that the burn-off treatment was successful in removing debris from the fibre surfaces. The XPS results for the different de-sizing treatments used in this study are summarized in table 3.

With reference to table 3, considerable scatter was observed in the as-received fibre data. The acetic acid de-sizing treatment was found to be not as effective as the pyrolysis de-sizing process. The pyrolysis-based de-sizing process was found to be least efficient when the fibres were introduced directly into the furnace which was set at 700 °C with a short hold period of 15 min. A longer dwell period resulted in the lowest carbon content on the surface of the fibres. It was not possible to identify the origin of the nitrogen peak with any certainty but it may be associated with the presence of amine functional groups in the size. The nitrogen peak was undetectable after the de-sizing operations. Typical XPS spectra for the quartz fibres subjected to different treatments are shown in figure 3.

3.2. Evaluation of the self-sensing fibres and composites

3.2.1. Quality of the cladding. SEM was used to inspect the quality of the impregnation process. Figures 4(a) and (b) illustrate good and poor penetration of the polymer around the de-sized Quartzel fibre bundle respectively. The quality of the coating was found to be a function of the polymer viscosity, temperature and the degree of separation of the individual fibres in the bundle. Further work is currently in progress to study the influence of resin (cladding material) viscosity on the coating quality. Other cladding materials such as epoxies are also being investigated.

3.2.2. Cleaving. The difficulties associated with obtaining good quality cleaves are also readily apparent in figures 5(a) and (b). The quality of the cleave for the self-sensing fibre system was found to be improved by cleaving the fibres under tension. This was achieved by bending the fibre bundles around glass cylinders of various diameters and then using a fresh razor blade to cleave the fibre bundle each time. Although pre-tensioning was found to improve significantly the quality of the cleaves, it was not possible to obtain a uniform cleave for all the individual fibres in the bundle. From a practical viewpoint, cleaving-related issues may not pose any significant concern because if the self-sensing fibres are embedded within the structure, then polishing the free edge of the structure to expose the embedded fibre bundle(s) is possible.

3.2.3. Embedded optical fibres and self-sensing fibres. Figures 6(a)–(d) illustrate the effect of the embedded 125, 50 and 30 μm fibres and the self-sensing fibres on the AFRC respectively. With reference to figure 6(a), the diameter mismatch between the reinforcing fibres and the conventional 50/125 μm optical fibre is readily apparent along with the presence of a large resin-rich region. In the context of a low-cost impact damage detection system, it is difficult to envisage large-area coverage of engineering structures with conventional optical fibres which are at least an order of magnitude larger in diameter

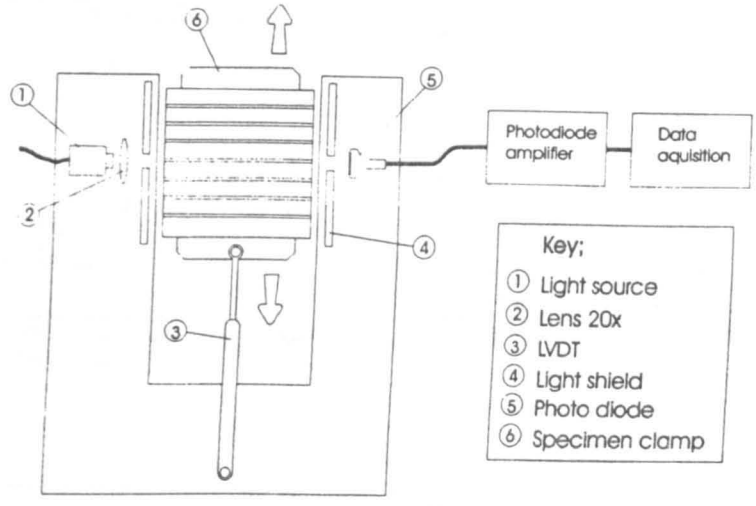

Figure 1. Schematic illustration of the experimental set-up which was used to measure the transmitted light intensity through the conventional optical fibres and the self-sensing fibres before and after impact.

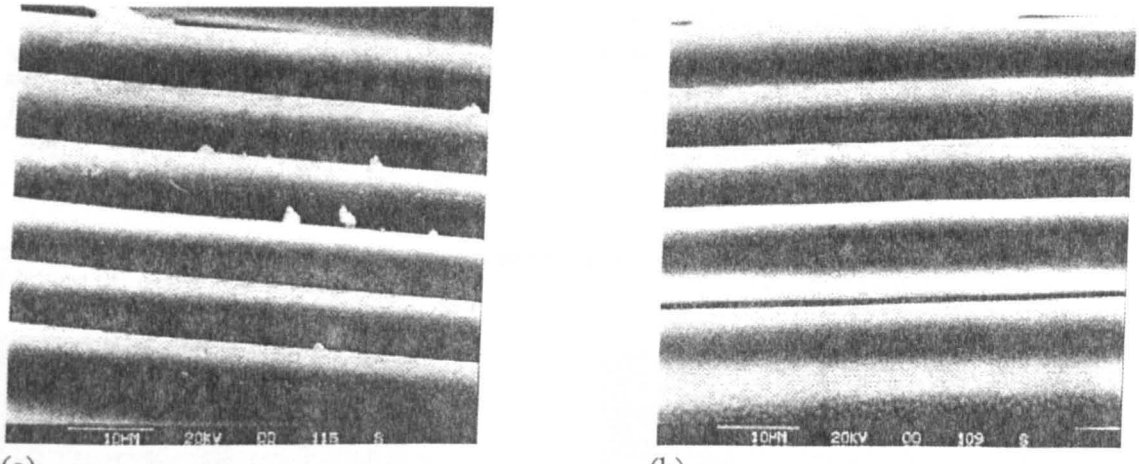

Figure 2. Scanning electron micrograph of the Quartzel fibres: (a) before burn-off and (b) after burn-off.

Table 3. Summary of the XPS results for the Quartzel fibre surface as a function of de-sizing conditions.

Condition	Carbon (at.%)	Oxygen(at.%)	Silicon(at.%)	Nitrogen(at.%)
As-received fibres—run 1	63.87	23.3	9.41	3.43
As-received fibres—run 2	57.93	27.77	10.15	4.15
Acetic acid reflux	31.29	49.56	19.15	—
Fast ramp to 700 °C & hold for 15 min	13.88	59.44	26.68	—
Fast ramp to 700 °C & hold for 1 h	12.65	62.14	25.21	—
Slow ramp to 700 °C & hold for 1 h	9.04	61.0	29.96	—

than the reinforcing fibres. The advantage of using smaller-diameter optical fibres is illustrated in figures 6(b) and (c) which show 50 μm and 30 μm embedded optical fibres respectively. Figure 6(d) shows a micrograph of the embedded silicone-coated Quartzel fibres. The apparent glow in the self-sensing fibres was achieved by illuminating the fibres from the opposite end.

The self-sensing fibres have a number of advantages over conventional optical fibre sensing techniques, including the following.

(i) The sensing fibres will not have any detrimental effect on the properties of the composite because of diameter compatibility and the ability to engineer the interface as required.

(ii) The sensing fibres can be incorporated at pre-determined locations into most composite preforms at the manufacturing stage.

(iii) The instrumentation involved for the source and the detector can be simple, low cost and robust.

(iv) The cladding material can be selected to fulfil other sensing requirements, for example, temperature monitoring.

The self-sensing fibres also have the potential to be

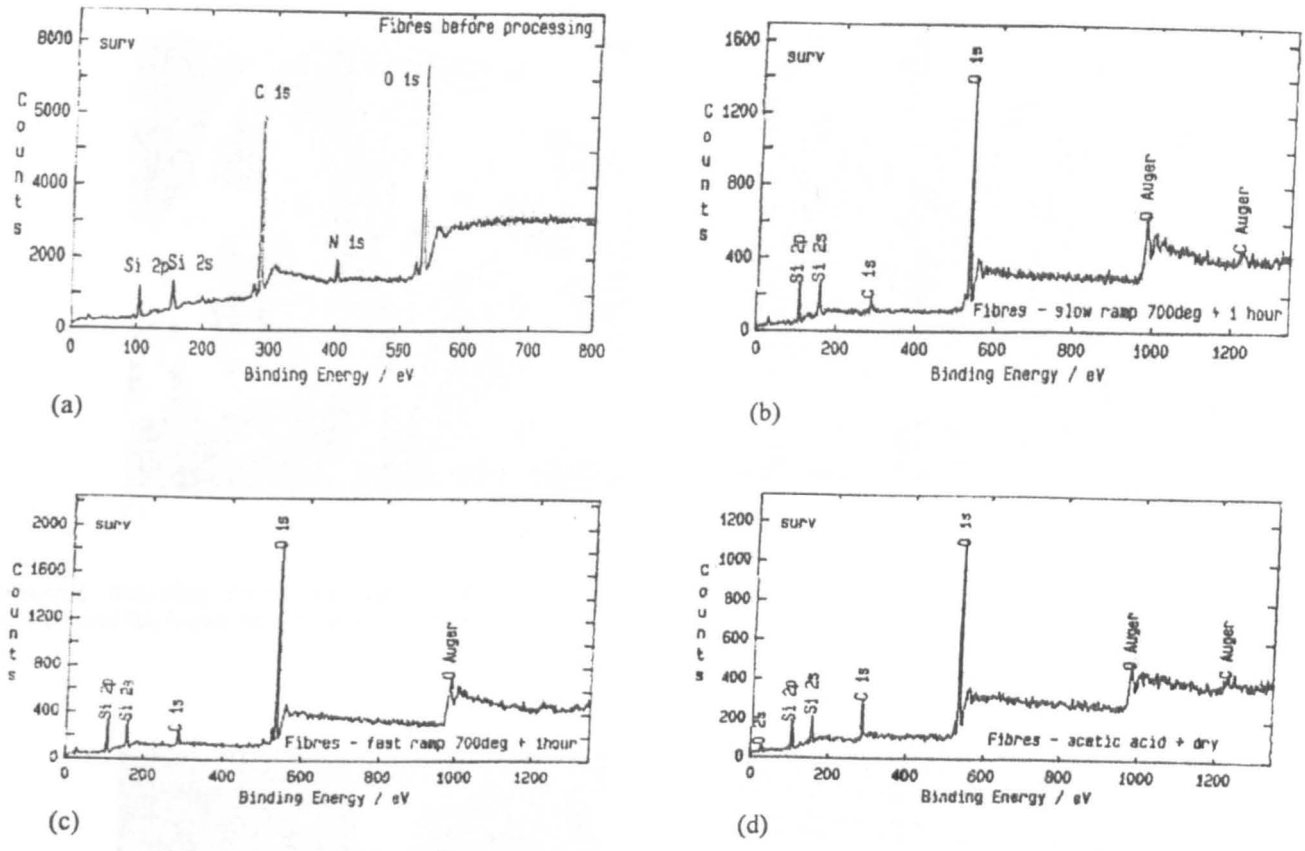

Figure 3. Typical XPS spectra for: (a) the as-received Quartzel fibres; (b) slow ramp to 700 °C held 1 h; (c) fast ramp to 700 °C held 1 h; and (d) acetic acid refluxed.

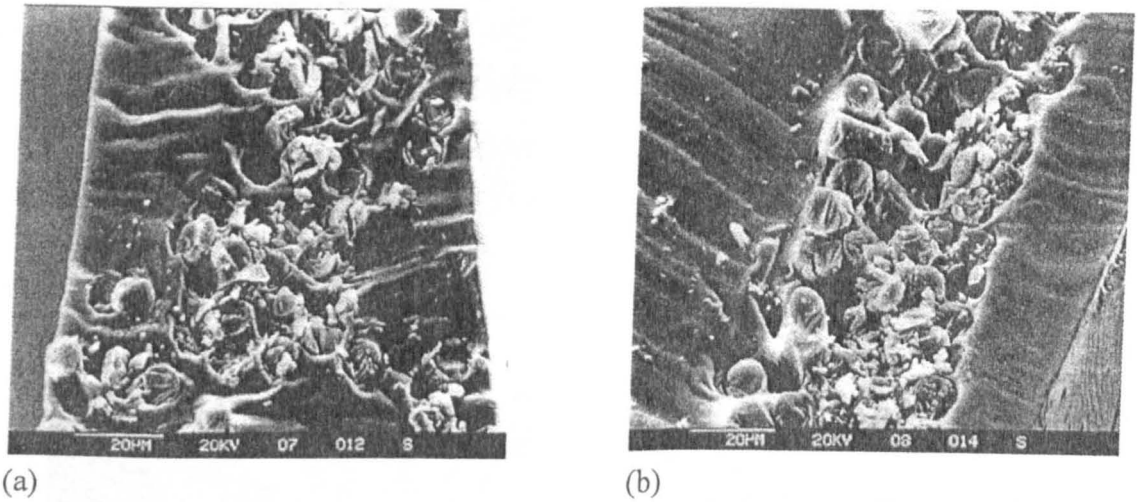

Figure 4. Scanning electron micrographs showing the extent of penetration of the cladding material (silicone) around the fibres: (a) good penetration and (b) poor penetration.

used in many sensor applications in which ordinary optical fibres are used. However, a number of areas still need to be addressed with respect to the self-sensing composite. These include the following.

(i) Control over the distribution of the fibres within the bundle during the coating process.

(ii) Minimizing the void content and the extent of fibre damage during the cladding operation.

(iii) Selection of the cladding material to make it chemically compatible with the epoxy matrix.

(iv) Control over the interfacial bond strength to obtain the required level of sensitivity towards impact damage.

3.2.4. Impact damage detection. The sensing fibres were located between plies 1–2 and 15–16 because damage development in AFRCs shows a characteristic spread from the point of impact on one surface through the thickness of the test specimen. In this paper, only the results from the bottom row of optical and self-sensing fibres are reported. A clear indication of the extent of delamination

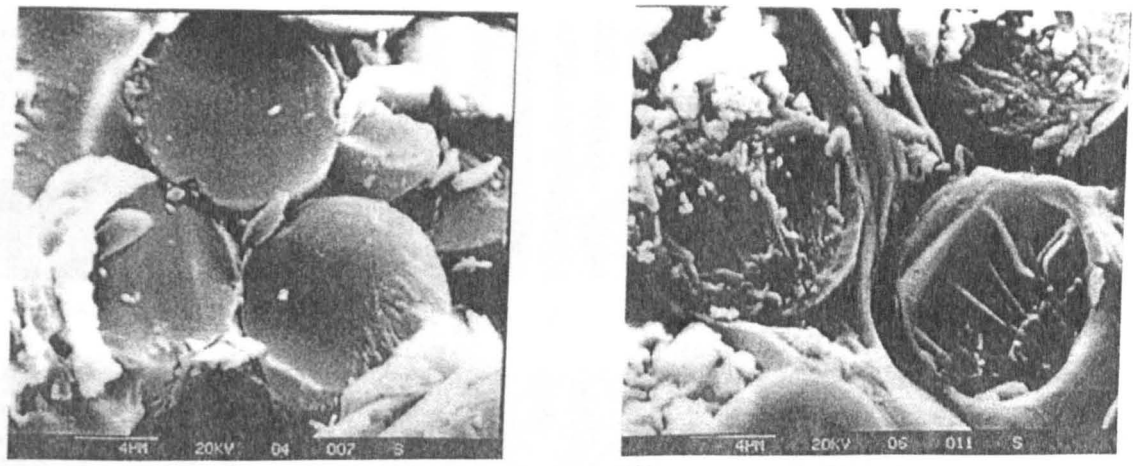

(a) (b)

Figure 5. Scanning electron micrographs showing the effect of tension on the quality of the cleave: (a) fibres cleaved under tension and (b) fibres cleaved in a stress-free state.

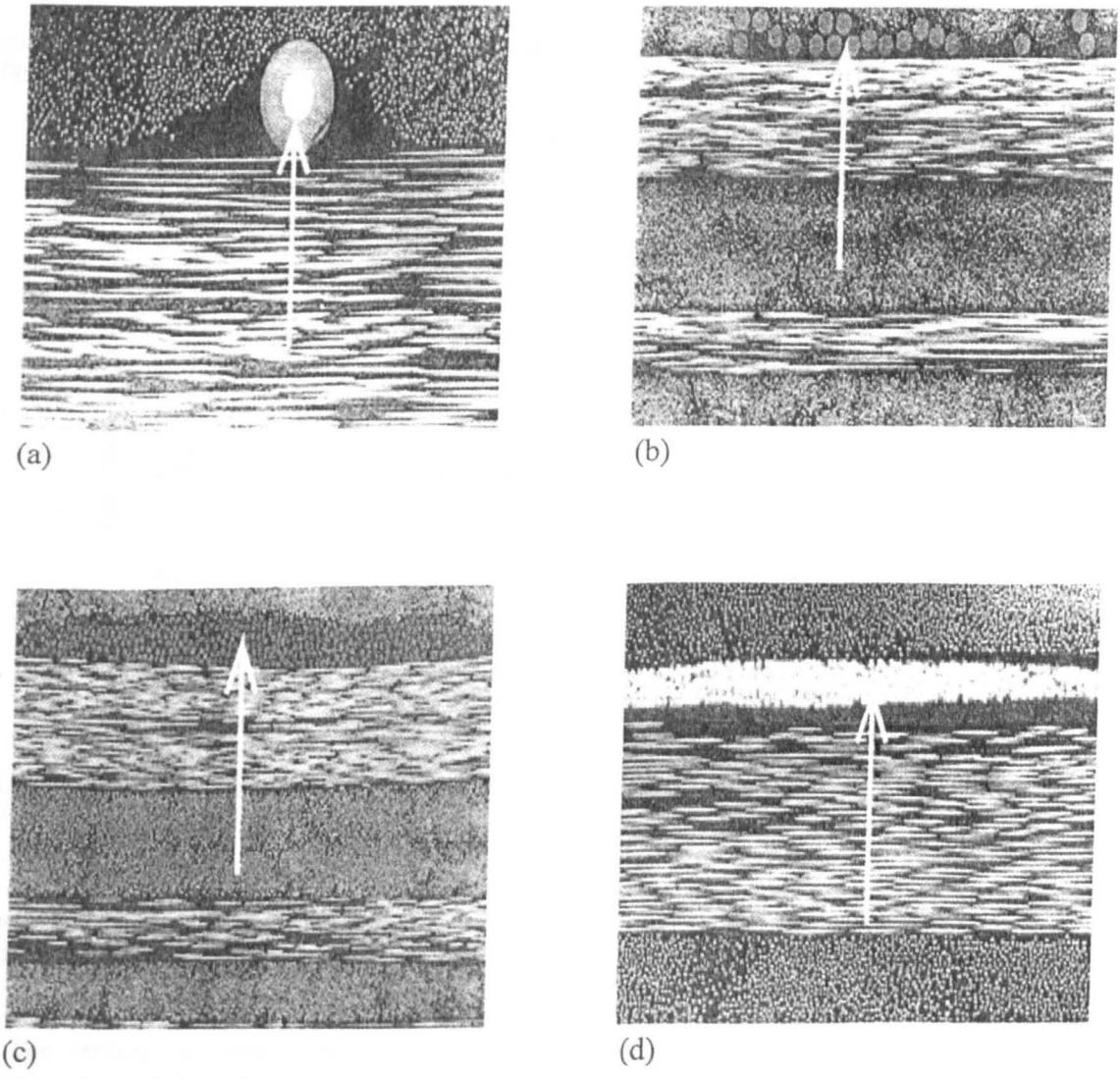

(a) (b)

(c) (d)

Figure 6. Embedded conventional optical fibre sensors and embedded self-sensing fibres within carbon fibre cross-ply composites: (a) 125 μm optical fibre; (b) 50 μm optical fibre bundle; (c) 30 μm optical fibre bundle; (d) self-sensing fibre bundle.

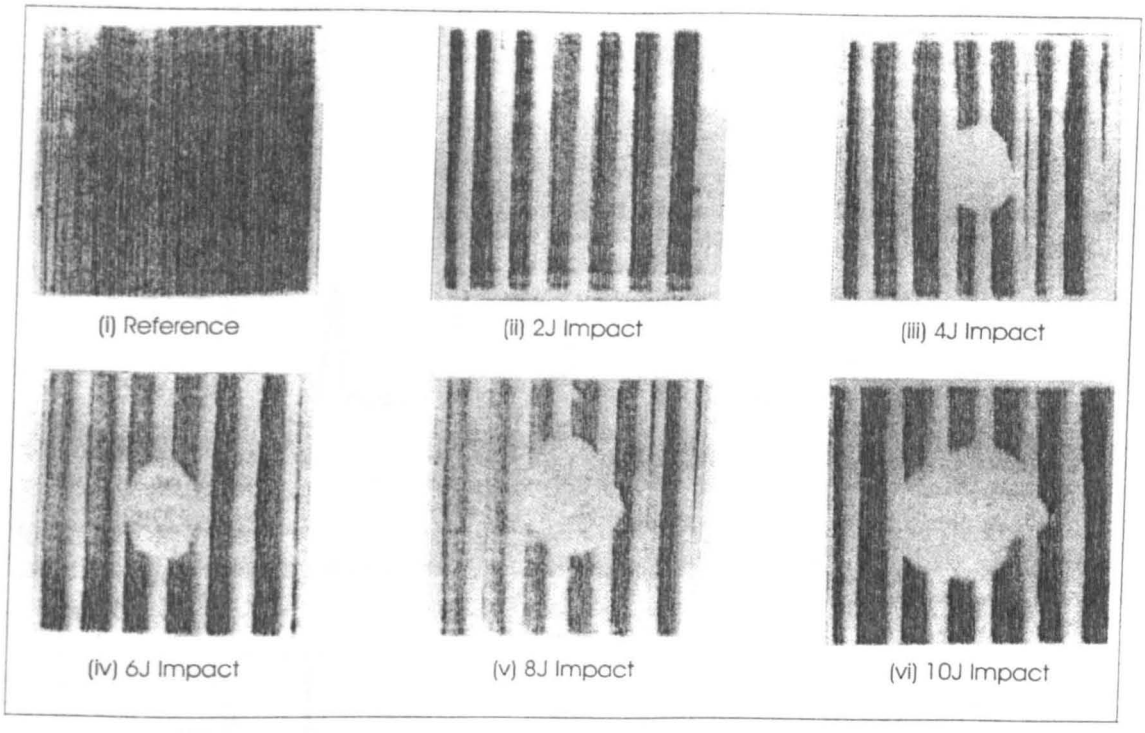

Figure 7. Selection of six typical C-scans for a reference panel (no impact) and five impacted self-sensing composite panels at different impact energies.

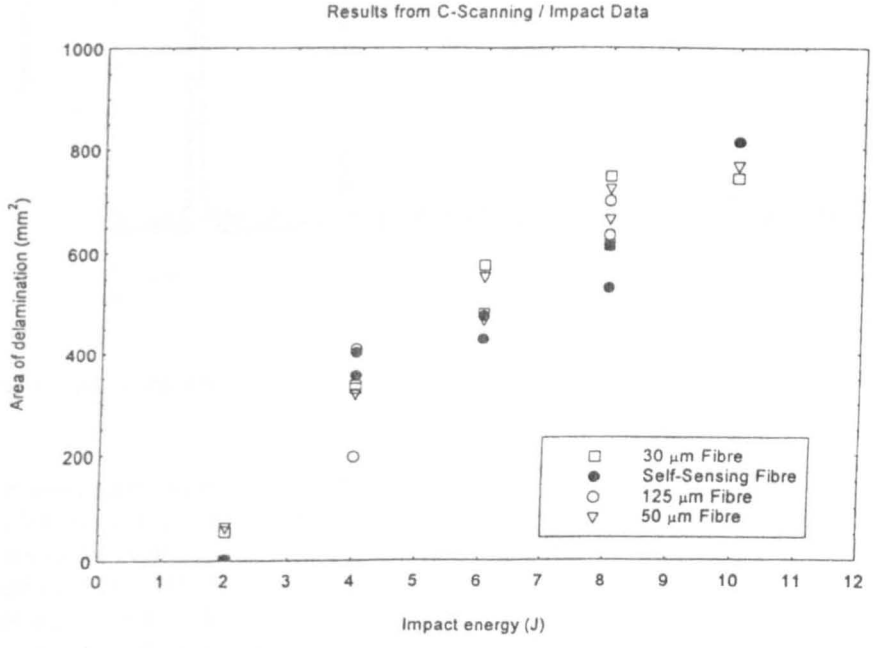

Figure 8. Illustration of the observed relationship between the incident impact energy and the resultant delaminated area as inferred from the C-scans.

as a consequence of the impact event can be inferred from the C-scans presented in figure 7(i)–(vi). In general, delamination damage was readily visible in the C-scans for impact energies above 2 J. However, two test specimens which were impacted at 2 J did show some evidence of delamination. The vertical lines which can be seen in figure 7 show the locations of the coated self-sensing fibres and do not represent voids. The total area of delamination was calculated using image analysis and was found to increase as a function of impact energy as shown in figure 8.

The corresponding data for the 125, 50 and 30 μm fibres are also represented in figure 8. In order to make any quantitative comments on the relative influence of the embedment on the nature of impact damage development, detailed microscopic information is first required. The details of a study on the nature of damage development in these test specimens will be published in due course.

The results from the light intensity measurements of the silicone-coated self-sensing composite before and after impact are presented in figures 9–11. With reference to

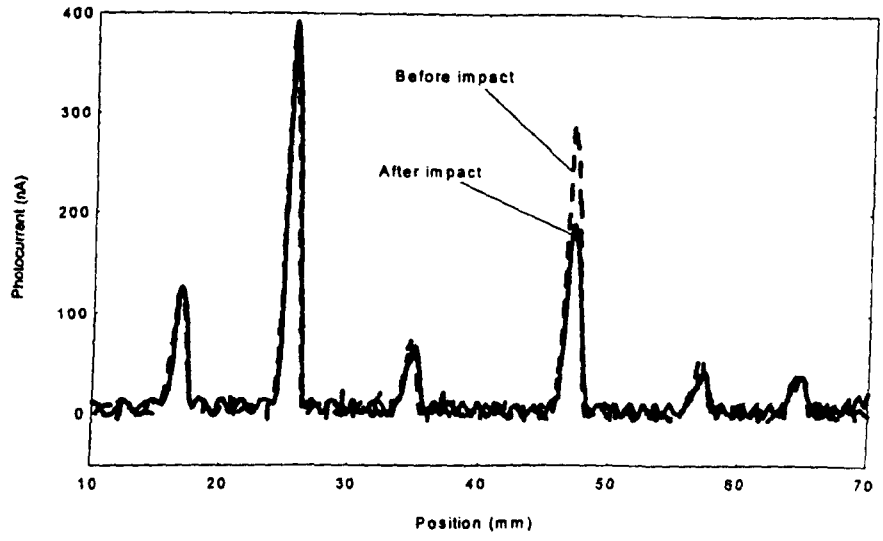

Figure 9. Light transmission characteristics of the self-sensing composite before and after impact at 2 J.

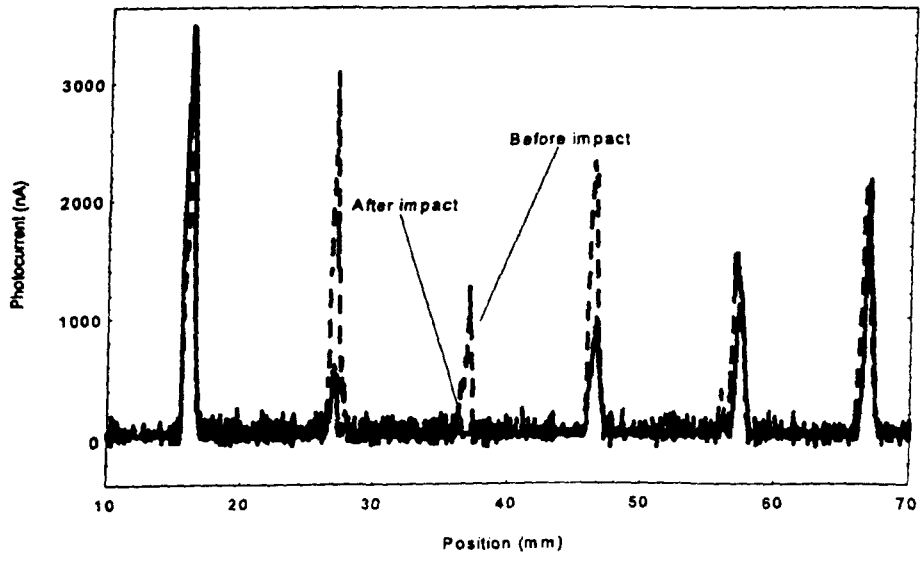

Figure 10. Light transmission characteristics of the composite with embedded 50 μm optical fibres before and after impact at 6 J.

figures 9–11, the X-axes refer to the position of the self-sensing fibres from left to right within the composite panel and the Y-axes represent the measured light intensity before and after impact testing. The self-sensing composite was capable of detecting a 2 J impact whereas the C-scan data suggest that there is no damage at this loading. None of the other embedded fibre types were capable of detecting a 2 J impact load. It is also apparent from figure 9 that the light transmission characteristic of the self-sensing fibres is highly variable. This inconsistency has been attributed to fibre damage caused by the current coating (cladding) process. Other methods of coating the self-sensing fibres, including the feasibility of electrostatic spraying, are being assessed. The self-sensing fibres were capable of detecting impact events at 4, 6, 8 and 10 J.

The effects of 4 J and 6 J impact loading on the 30 and 50 μm embedded optical fibres were similar and hence figure 10 shows only the results from the 6 J impact loading of the 50 μm fibres. The light transmission characteristics of the custom made 30 and 50 μm optical fibres were more consistent when compared with the self-sensing fibres. It is interesting to note that the 50 μm fibres was also capable of detecting the effects of a 4 J impact approximately 10 mm on either side of the impact point. Microscopic examinations revealed the presence of remote matrix cracks in the vicinity of the fractured 50 μm optical fibres. The composite panel with the embedded 50/125 optical fibres was capable of detecting impact damage at 6 J or greater. At impact loadings above 6 J, there was clear visual evidence of impact damage and hence the data for the 8 and 10 J impact tests are not discussed.

4. Conclusions

In summary, the feasibility of using reinforcing fibres as a light guide has been demonstrated. The self-sensing fibres were successfully embedded into carbon fibre prepregs and

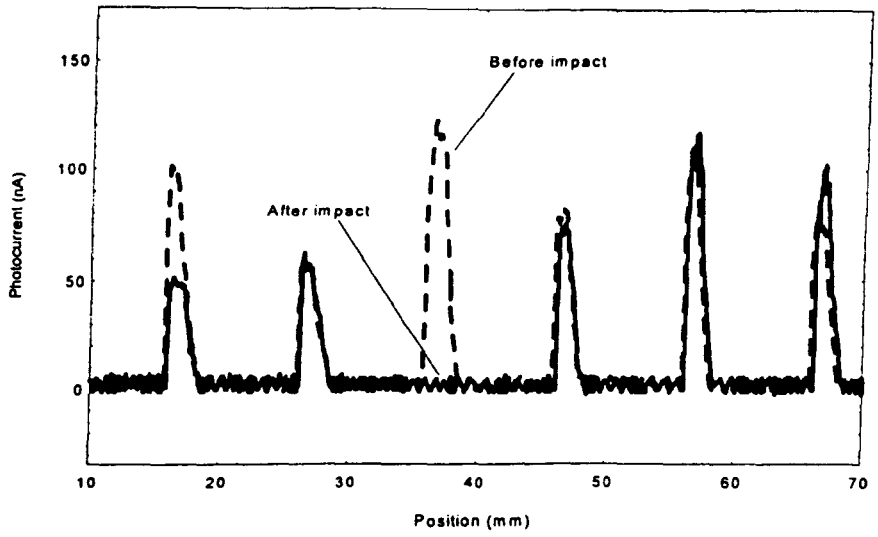

Figure 11. Light transmission characteristics of the composite with embedded 125 μm optical fibres before and after impact at 6 J.

then processed into composite panels. The self-sensing fibres were capable of detecting impacts as low as 2 J when impacted using a 20 mm hemispherical tup. The conventional optical fibres which were used in this study were capable of detecting impacts at and above 4 J. Further work is currently in progress to improve light transmission characteristics of the self-sensing fibres and inter-connection techniques.

Acknowledgments

The authors thank the EPSRC for the award of a ROPA grant and QUOTA and CASE studentships to T Liu, S Hayes and D Brooks respectively. D Brooks also acknowledges the Defence Research Agency (DRA) for a CASE award. The authors would also like to thank Professor P Curtis and Mr R Badcock of the DRA for supporting the research programme. We thank Industrial Silicones and Lubricants Ltd, TSL and Quartz et Silice for the provision of the materials used in this research programme. The authors are also grateful to D Adams, J Coleman, C Doyle, J Felgate and A Martin for assistance given in the course of this research.

References

[1] Xu M G, Archambault J L, Reekie L and Dakin J P 1994 Discrimination between strain and temperature effects using dual-wavelength fibre grating sensors *Electron. Lett.* **30** 1085

[2] Liu T, Fernando G F, Rao Y J, Jackson D A, Zhang L and Bennion I 1996 *In-situ* strain measurements in composites during fatigue testing using optical fibre Bragg gratings and a portable CCD detection system *SPIE Conf. Proc. Photonics (China, 1996)*

[3] Jones M E, Grace J L, Greene J A, Tran T A, Bhatia V, Murphy K A and Claus R O 1995 Multiplexed absolute strain measurements using extrinsic Fabry–Pérot interferometers *Smart Structures and Materials 1995 SPIE Proc.* **2444** 267–75

[4] Badcock R and Fernando G F 1995 Fatigue damage detection in carbon fibre reinforced composites using an intensity based optical fibre sensor *Smart Structures and Materials 1995 SPIE Proc.* **2444** 423–31

[5] Martin A R, Hayes S A, Fernando G and Hale K F 1995 Impact damage detection in filament wound tubes utilising embedded optical fibres *Smart Structures and Materials 1995 SPIE Proc.* **2444** 490–501

Paper 3

Smart Mater. Struct. 7 (1998) 145–158. Printed in the UK PII: S0964-1726(98)90072-6

In-situ process and condition monitoring of advanced fibre-reinforced composite materials using optical fibre sensors

C Doyle, A Martin, T Liu, M Wu, S Hayes, P A Crosby, G R Powell, D Brooks and G F Fernando†

Department of Materials Engineering, Brunel University, Uxbridge, Middlesex UB8 3PH, UK

Received 11 October 1996, accepted for publication 31 July 1997

Abstract. This paper presents a general overview of a number of optical fibre sensor systems which have been developed and used in advanced fibre-reinforced composites for *in-situ* process and condition monitoring. The *in-situ* process monitoring techniques were optical-fibre-based evanescent wave spectroscopy, transmission near-infrared spectroscopy and refractive index monitoring. The optical fibre sensors were successful in tracking the cure reaction. The condition monitoring of advanced fibre-reinforced composites was carried out using two intensity-based optical fibre sensor systems: an extrinsic multi-mode Fabry–Pérot sensor and Bragg gratings. In addition to this, the feasibility of using the reinforcing fibre as a light guide was demonstrated. These sensor systems were evaluated under quasi-static, impact and fatigue loading. The test specimens consisted of prepreg-based carbon-fibre-reinforced epoxy and glass-fibre-reinforced epoxy filament-wound tubes. Excellent correlation was obtained between surface-mounted strain gauges and the embedded optical fibre sensors. The feasibility of using these sensor systems for the detection of impact damage and stiffness reduction in the composite due to fatigue damage was successfully demonstrated.

1. Introduction

Advanced fibre-reinforced composites (AFRC) are used extensively for primary and secondary load-bearing applications. Consequently, there is a growing interest in sensor systems for on-line process monitoring and for evaluating the integrity of these materials in-service. From an AFRC manufacturer's viewpoint, the primary requirement is to establish the chemical state of the resin system and then to optimize the cure schedule to account for the condition of the resin. End-users of AFRCs have a different requirement, namely, a facility to monitor the structural integrity *in situ* or in real-time. Both these requirements can be fulfilled using optical-fibre-based sensing systems.

1.1. *In-situ* cure monitoring

Optical fibre sensors (OFS) offer a number of unique advantages for cure monitoring when compared with other techniques such as measurement of dielectric properties, viscosity, acoustic velocity etc. This is because the optical-fibre-based sensor techniques can give information on the actual chemical concentrations of the constituent chemicals in the resin system, whereas the other techniques can only infer chemical concentration and/or composition. The non-optical techniques mentioned above require a vast database of information in order to establish a correlation between the sensor data and the state of cure. Furthermore, the results from some of these techniques may be influenced by moisture, the relative volume fractions of the fibres, fibre orientation and electrical interference from the processing equipment. OFS are immune to these factors and can give additional information on moisture content and the temperature ramp which is used during the heat-up cycle.

The following points illustrate the need for on-line cure monitoring.

(i) *The extent of cure and the homogeneity of the cure in large AFRC structures.* The mechanical properties of AFRCs are generally dominated by the properties of the reinforcing fibres. However, the matrix-dominated properties, such as compressive strength, impact strength, hygrothermal behaviour, load-transfer efficiency

† To whom correspondence should be addressed. Current address: Department of Engineering Systems, Royal Military College of Science, University of Cranfield, Scrivenham, Swindon SN6 8LA, UK

0964-1726/98/020145+14$19.50

and interlaminar shear strength can be affected by the crosslink density of the resin system used. The crosslink density is in turn influenced by factors such as the chemical state of the resin before cure, moisture content and the processing conditions. The long-term and the overall properties of the composite will also be influenced by the temperature profile and cure schedule.

(ii) *The chemical state of the resin (or prepreg) prior to cure.* This is a quality control issue. A number of AFRC users of prepregs and resins do not have access to equipment to monitor the extent of cure of the prepregs or resins prior to hot-pressing or autoclaving. This means that no processing modifications can be made to the cure schedule to compensate for the variable state of cure of the starting materials.

(iii) *Optimizing cure schedules with specific reference to interleaving technology (hybrid resins).* This point is related to recent advances in interleaving technology in AFRCs to suppress delamination growth and to retard the rate of fatigue damage propagation. Any interleaving material which is used to improve the fatigue and impact resistance should be compatible with the base resin and have a higher G_{1C} value. Any manufacturing method which utilizes hybrid resin technology will need access to cure schedules and models to ensure homogeneous curing. The results gained from this programme should allow existing models to be improved. This will enable components made with different resin systems to be processed in an autoclave simultaneously.

All the above mentioned points could be addressed if a simple technique to monitor, *in situ*, the initial chemical state of the resin and the chemical changes in the resin resulting from curing was available. From a cost-effective viewpoint, the power to the autoclave can be turned off once a specified degree of cure has been achieved. In order to do this with a degree of confidence, a sensor system is required to monitor both the rate of cure and the temperature within the composite.

1.2. *In-situ* condition monitoring

A major concern with AFRCs is the difficulties associated with detecting fatigue and impact damage. This is due to the progressive nature of internal damage development in AFRCs. Conventional non-destructive evaluation (NDE) methods include the following: (i) strain measurements using surface-mounted strain gauges or extensometers [1]; (ii) dye penetrant-enhanced x-ray radiography [2]; (iii) C-scans [3]; (iv) thermography [4]; (v) acoustic emission [5] and (vi) electrical conductivity [6]. Although these techniques have been used widely by industry and in the laboratory, they are unsuitable for on-line monitoring.

The stiffness of an AFRC can provide useful information on its integrity. For example, damage in the form of fibre fractures and delaminations will reduce the overall stiffness of the material. The stiffness can be inferred from strain measurements made by embedded or surface-mounted devices. Examples of optical-fibre-based sensor systems which have been used for strain monitoring in AFRCs [7] include intrinsic and extrinsic

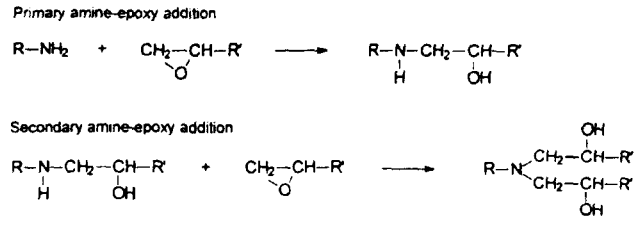

Figure 1. Generalized reaction scheme for an epoxy–amine resin system.

Fabry–Pérot type sensors [8, 9], intensity-based sensors [10], polarization-based sensors [11] and optical-fibre-based Bragg grating sensors [12, 13]. From a materials viewpoint, the optical fibre Bragg sensors are ideally suited for deployment in AFRC structures because of their simple design, small size and ease of integration into composite materials with minimal perturbation to the reinforcing fibres. They have a simpler design than most interferometric sensors, may be multiplexed [14] and are immune to intensity drifts. However, from an industrial point of view, reliability and low cost in installation and maintenance are important criteria to be fulfilled before OFS can compete with conventional sensors such as resistive strain gauges. Intensity-based OFS can be considered as a compromise between high-precision interferometric sensors and low cost.

In this paper we report the practical use of some optical-fibre-based sensor systems for *in-situ* process (cure) and condition monitoring of AFRCs.

2. Optical fibre-based cure sensors

Typical high-performance commercial resin systems use epoxy/amine formulations. Processing of these resin systems involves the conversion of the matrix resin from a low-molecular-weight viscous liquid or semi-solid to a highly cross-linked rigid structure. The processing parameters include pressure, vacuum and heat. Figure 1 shows the generalized epoxy–amine reactions which occur during cure. It can be seen from the reaction scheme that epoxy groups and amine groups are consumed during the cure process. Since vibrations due to C–H, N–H and O–H groups are the most prominent in the near-infrared region, the wavelength range from 1100–2300 nm is ideal for monitoring changes which occur to C–H, N–H and O–H groups during the cure process. The refractive index of the resin system also increases with the extent of cure.

This paper reports on four types of optical fibre sensors which have been developed to monitor the cure of epoxy–amine resin systems. These techniques are based on near-infrared spectroscopy and refractive index measurements during cure.

2.1. Near-infrared spectroscopy-based optical fibre cure sensors

A transmission spectroscopy sensor and an evanescent wave spectroscopy sensor were used to carry out the *in-situ* cure monitoring experiments on a model epoxy/amine resin. A

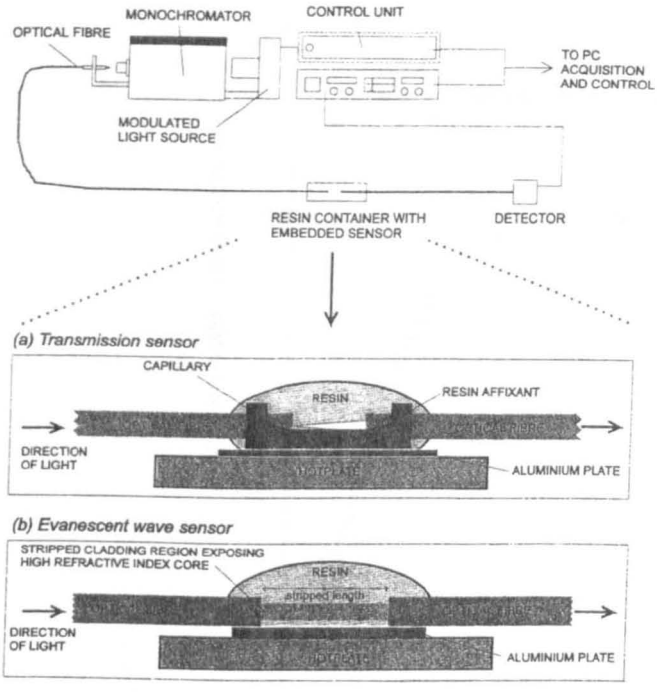

Figure 2. Schematic of transmission and evanescent wave optical fibre cure monitoring set-up.

diagram of the equipment and fibre configurations used for these sensors is shown in figure 2. The equipment used to scan across the spectrum was identical for both types of sensor. This consisted of a modulated quartz–halogen source and diffraction grating monochromator (Bentham Instruments). Light emerging from the monochromator was launched into the fibre using a microscope objective lens. Light received from the sensor was detected using an InGaAs photodiode detector and lock-in amplifier. Data acquired from the detection system and control of the monochromator wavelength were undertaken with PC control.

The transmission sensor was constructed from two 50/125 μm step-index silica optical fibres placed inside a precision bore metal capillary tube (internal diameter = 254 μm) which had one side ground down exposing the inside of the tube. The buffer coating was left on the outside of the fibres (diameter = 240 μm) to allow a close fit inside the capillary. The fibres were aligned with a gap of approximately 1.25 mm between the end-faces. A stoichiometric mixture of Epikote 828 resin (based on a diglycidyl ether of bisphenol-A epoxy resin) and 1,6-hexanediamine was placed over the sensor region so that the resin ran between the two optical fibres of the sensor. The hot-plate temperature was maintained at 40 °C and spectra were collected throughout cure over the range 1450–1700 nm.

Figure 3 shows overlaid spectra obtained from the optical fibre transmission sensor during the cure of Epikote 828 + hexanediamine at 40 °C. The peaks at 1535 nm, 1650 nm and 1670 nm are due to both primary and secondary amine groups, epoxy groups, and aromatic C–H groups, respectively. It can readily be seen that the amine peak at 1535 nm and the epoxy peak at 1650 nm decrease in magnitude during cure whereas the aromatic C–H peak

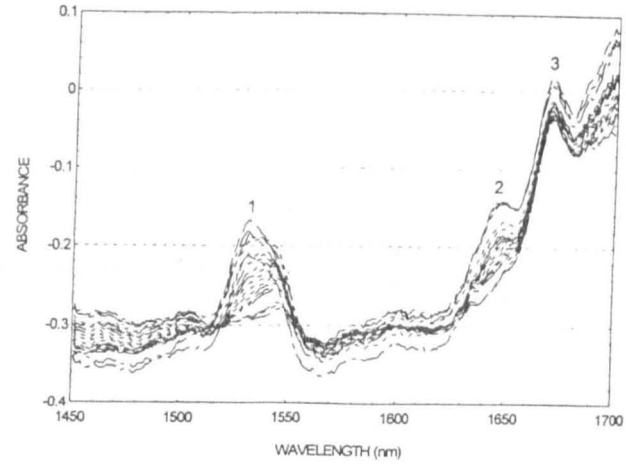

Figure 3. Optical fibre near-infrared transmission spectra of Epikote 828 and hexanediamine at 42 °C; peaks numbered 1, 2 and 3 correspond to amine groups, epoxy groups and aromatic C–H groups, respectively.

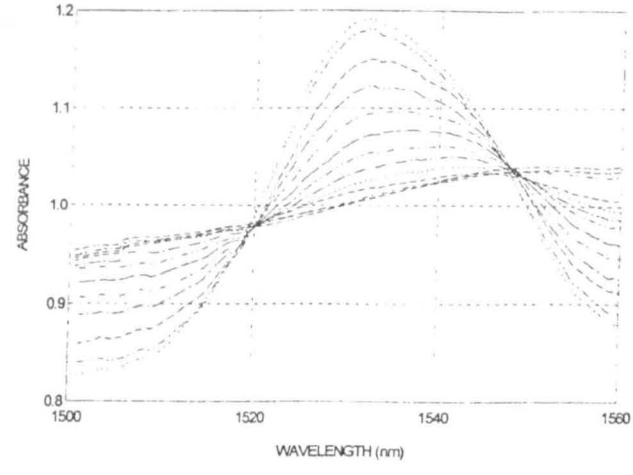

Figure 4. Overlaid optical fibre evanescent wave spectra obtained during cure of Epikote 828 + hexanediamine at 40 °C.

stays approximately the same. Additionally, it can be seen that the overall baseline of each spectrum rises during cure. This is due to an increase in the refractive index of the resin as it cures.

The evanescent optical fibre sensor was constructed from a piece of high-refractive-index core optical fibre (n = 1.65). A 30 cm length of silicone resin cladding material was removed from the fibre to allow the fibre core to be in intimate contact with the resin during cure. Figure 4 shows overlaid spectra obtained using the sensor during the cure of Epikote 828 and hexanediamine at 40 °C. The spectra have been baseline-corrected to compensate for the refractive index baseline shift by dividing each absorbance value by the mean of all values in the curve. Peak areas for the amine absorption peak at 1535 nm were measured for each cure spectrum obtained from the transmission and evanescent sensors. The data were converted to a fractional amine conversion (α) to allow comparisons between the data using the following equation:

$$\alpha = 1 - (\text{Area})_t/(\text{Area})_0$$

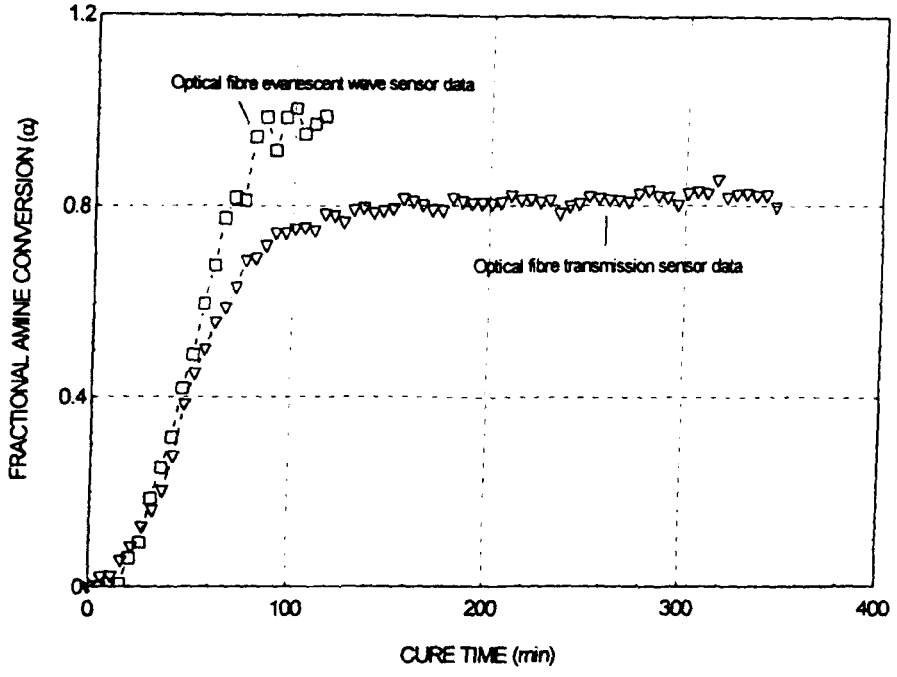

Figure 5. Data obtained during cure of Epikote 828 + hexanediamine at 40 °C from optical fibre evanescent wave and transmission sensors.

where α is the fractional amine conversion and $(\text{Area})_t$ and $(\text{Area})_0$ are the amine peak areas at a time t during cure and at the start of the reaction.

Data obtained for amine fractional conversions from the transmission and evanescent optical fibre sensors during cure are shown in figure 5. It can be seen that the two sensors showed similar profiles up to 50 min cure time. After this point the two methods began to deviate. This was because the evanescent sensor showed the amine absorption peak area to fall to zero towards the end of cure, producing a fractional conversion value of zero. However, the transmission sensor at the same cure time showed some amine still to be present. Results from FTIR spectroscopy experiments confirmed that at 40 °C, there was some amine present at the end of cure with a final fractional conversion of amine of approximately 0.8 being achieved. This compares well with the transmission optical fibre data.

2.2. Refractive-index-based cure sensors

Two single-wavelength optical-fibre-based sensors have been developed to monitor the cure of epoxy resin systems using changes occurring to the refractive index of the resin. The first type of sensor is a modification of the evanescent sensor shown in figure 2. The sensor was constructed from a piece of high-refractive-index optical fibre which has a small portion of its cladding removed (25 mm). Light from a 1310 nm laser diode source was introduced into the fibre and the intensity monitored using an InGaAs detector, photodiode amplifier and PC.

The second type of optical fibre sensor was based on Fresnel reflections from a cleaved fibre end placed in a curing resin sample. A silica fibre 2 × 1 coupler was set up with a 1310 nm laser diode source and an InGaAs photodiode detector at the double end. The single fibre end was cleaved and placed in the resin sample. Changes in the reflection from the optical-fibre–resin boundary were monitored and related to changes in the refractive index during cure. Results obtained from both types of sensor during the cure of Epikote 828 and hexanediamine at 45 °C are shown in figure 6. As the temperature of the resin rises to its set-point, changes occur to both the back-reflection and stripped cladding sensors. After this point, any changes to the intensity of each sensor can be attributed to the increase in the refractive index of the resin during cure. The back-reflection sensor signal was found to be proportional to the refractive index of the curing resin whereas the stripped cladding sensor signal was inversely proportional to the resin refractive index. Both types of sensor showed that the cure reaction was complete after approximately 100 min.

3. Intensity-based optical fibre sensors for crack and impact damage detection

A typical intensity-modulated optical fibre sensor system consists of a light source, a sensing device, within which the intensity of light is altered by the measurand in some way, a detector to measure the intensity of the transmitted signal and optical fibres to carry light between these components. The principal advantage of such a system is that it does not need the complicated instrumentation and signal processing demanded by other classes of OFS, which increase their cost and reduce their applicability.

3.1. Embedded OFS for damage detection in filament wound tubes

Intensity-based systems are susceptible to errors caused by spurious changes in the light intensity received at the

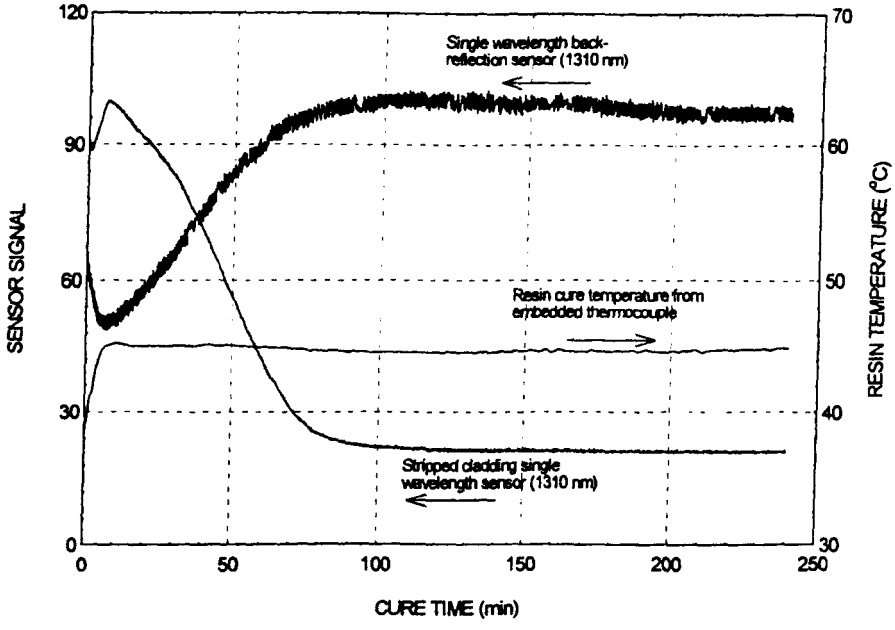

Figure 6. Cure data obtained from single-wavelength back-reflection and stripped cladding optical fibre sensors during cure of Epikote 828 and hexanediamine at 45 °C.

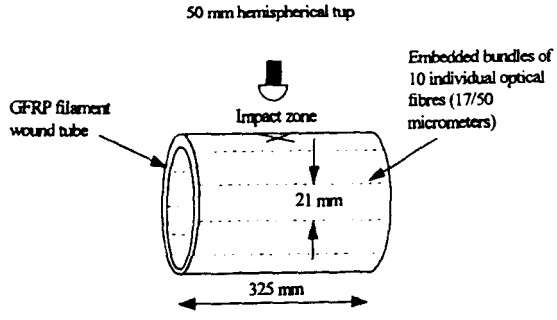

Figure 7. Schematic of the embedded optical fibre locations and the dimensions of the filament-wound tubes.

detector. Power fluctuations of the source, microbending losses in fibres and losses at splices and connectors all impose variations on the sensor signal and lead to errors. Quantitative damage detection demands the generation of a reference signal to compensate for intensity fluctuations. Intensity-based sensor systems without such referencing means are technically simple and low cost but they can only provide qualitative information. However, there is still a strong demand in industry for low-cost systems for detecting fibre fracture and impact damage in composites.

Hale *et al* [15] present one of the earliest and simplest intensity-based optical fibre sensors, for detecting the passage of cracks through a material. Optical fibres were attached to the surface of the material or embedded within it. Fibres fractured when traversed by a crack and the resulting drop in transmitted light gave an indication of the progress of cracks. In the current work, the custom-made 17/50 μm optical fibres were integrated into the filament-wound tubes at the time of manufacture. A schematic of the location of the optical fibres in the filament-wound tube is given in figure 7.

The light transmission through each length of the optical fibres was determined before and after impact with a white light source and a photodetector array. The filament-wound tubes were impacted at 2, 5, 8 and 10 J using a Rosand instrumented impact falling-weight machine fitted with a 50 mm hemispherical tup. The impact point was located between a pair of the embedded optical fibre bundles.

The optical-fibre-based crack detection sensor system was evaluated in two ways. Firstly, the tube was inspected for bleeding light after the impact and secondly, the light transmitted through the optical fibres was determined before and after impact.

Bleeding light. The following paragraph refers exclusively to figure 8. Figure 8(a) illustrates that no bleeding light was detected after subjecting the filament-wound tube to an 2 J impact. Figures (b) and (c) show bleeding light in the vicinity of the impact point after 5 J and 10 J impacts, respectively. The micrographs presented in figures (d)–(f) illustrate the nature of the impact damage at 2, 5 and 10 J respectively. The predominant damage mode at 2 J was matrix cracking. The extent and the number of matrix cracks and delaminations were seen to increase progressively for the 5 J and 10 J impacts. The primary cracks have been enhanced for clarity. However, it has to be appreciated that the observed damage features will be a function of distance and orientation from the impact point.

Figures (g)–(i) are schematics of the observed damage after subjecting the filament-wound tubes to 2, 5 and 10 J impacts respectively. The first signs of reinforcing fibre and optical fibre fractures were seen at impact energies of 5 J and above. Figure 8(i) illustrates the presence of matrix cracks remote from the impact zone. This is a unique feature in impact-damaged glass-fibre-reinforced filament-wound tubes which is caused by the deflection of the tube as a consequence of the impact.

Intensity measurements before and after impact. The light intensities transmitted through the optical fibres were determined before and after impact. Figures 9 and 10 show

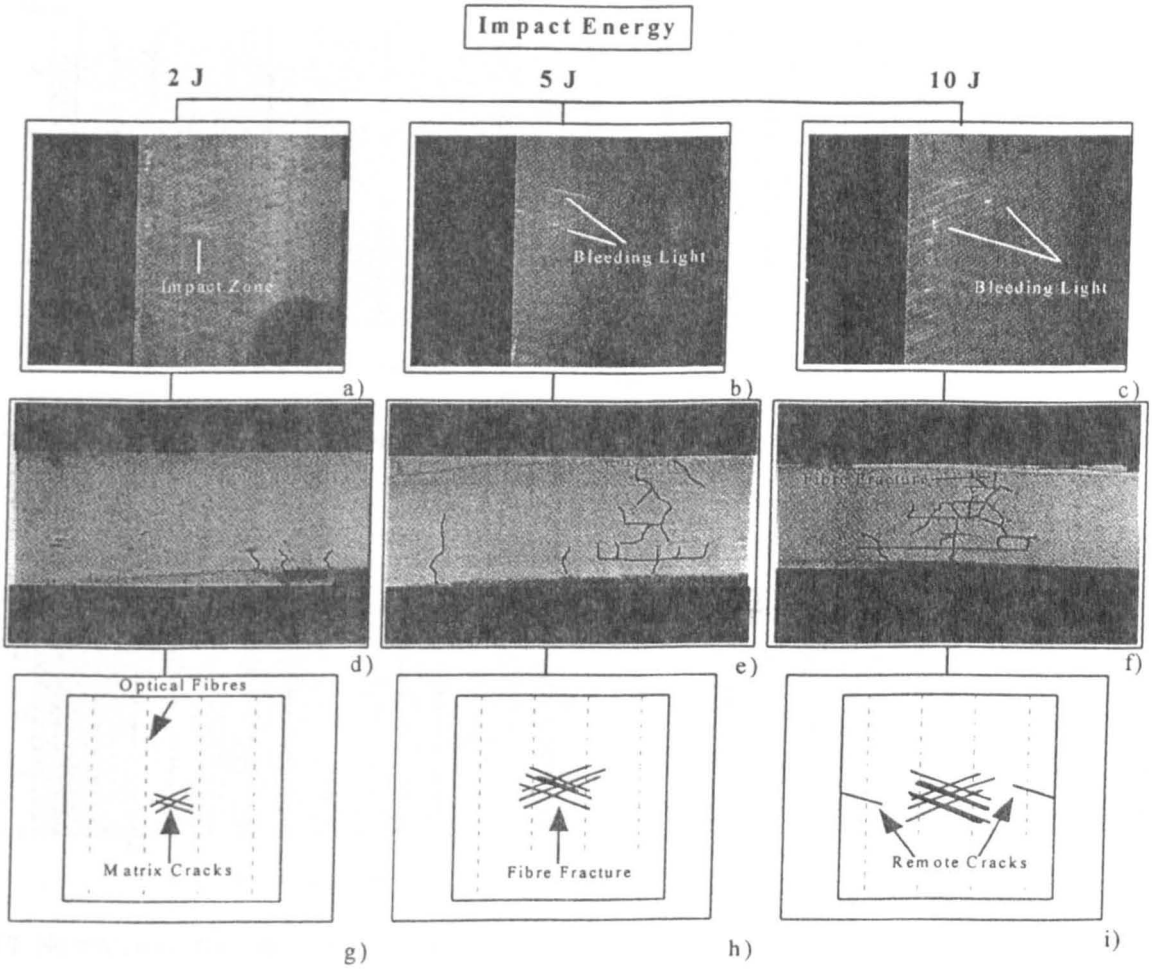

Figure 8. (a)–(c) Bleeding light emanating from the optical fibres after impact. (d)–(f) Micrographs showing the nature of damage sustained by the filament-wound tubes after impacts corresponding to 2, 5 and 10 J, respectively. (g)–(i) Schematic illustration of the damage in the filament-wound tubes for the three incident impact loads.

normalized light transmission through the embedded optical fibres. The normalization was carried out with respect to the average light transmission through the optical fibres for the composite in the undamaged state.

Figure 9(a) shows that the crack detection system used in this study was not capable of detecting a 2 J impact. It is readily apparent from figures 9(b) and 10 that the embedded 17/50 μm optical fibres were capable of detecting impact damage at 5 J and above. Figure 10(b) also demonstrated that this crack detection technique could detect remote cracks in the filament-wound tube which was impacted at 10 J.

Although the optical-fibre-based crack detection technique is simple and economical to implement, its limitations have to be appreciated. The process of damage initiation and propagation in AFRCs is complex and can be influenced by a multitude of factors including the strength, stiffness and failure strain distributions of the reinforcing fibres and the matrix. The interfacial bond strength between the matrix and the fibres plays an important role in determining the observed failure modes. The method of stress application, i.e., fatigue, impact, tensile, compressive or quasi-static loading and the rate of stress application can influence the damage initiation and propagation processes in AFRCs. Other factors which can influence the initiation and propagation of damage include the environmental conditions, void content in the AFRC, relative volume fraction of the reinforcing fibres and their relative orientations, the state of residual stress, and the ply stacking sequence.

3.2. Impact damage detection using intensity-based vibration sensing

The vibrational characteristics of AFRCs can be used to obtain information on their structural integrity. Optical-fibre-based techniques present an alternative to conventional accelerometers. Non-contact vibrometry may be performed by simple intensity-based devices [16], techniques such as optical triangulation [17] or laser interferometry. Employing optical fibre light guides facilitates measurements where it is difficult to focus a beam directly [18]. Intensity-based [19, 20], modal interference [21] and interferometric [22] optical fibre vibration sensors have all been described in the literature. Strain gauges with a sufficiently high bandwidth may be attached to a structure to pick up fluctuations in stress and strain as acoustic waves pass through it. Fabry–Pérot [23] and Mach–Zehnder [24] fibre interferometers and two-mode polarimetric sensors [25] have been demonstrated as vibration sensors.

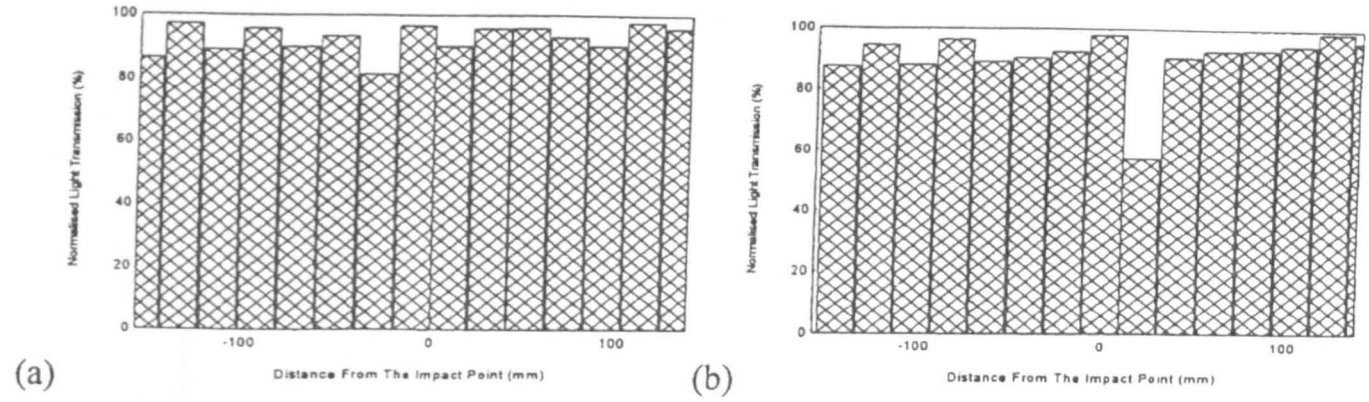

Figure 9. Normalized output light intensity as a function of location from the impact point for (a) 2 J and (b) 5 J impact.

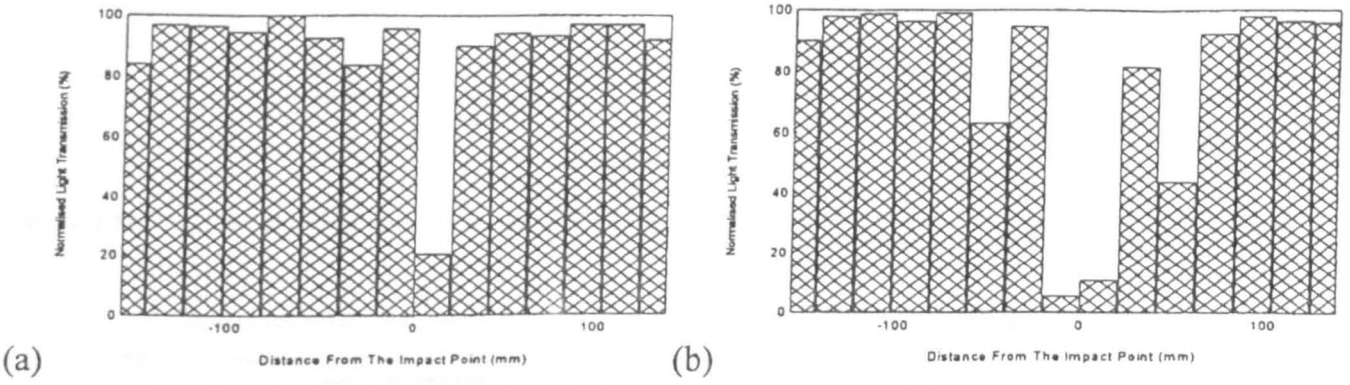

Figure 10. Normalized output light intensity as a function of location from the impact point for a (a) 8 J and (b) 10 J impact.

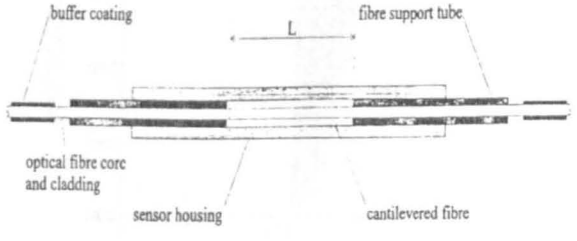

Figure 11. Sectional diagram of the vibration sensor.

Here we describe an intensity-based sensor which offers not only low cost but also an additional function of post-impact damage detection. A schematic of the sensor is presented in figure 11.

The sensor comprises two de-buffered, cleaved, multi-mode optical fibres inserted into 10 mm lengths of silica capillary. The end of one fibre is kept flush with the end of the tube, whilst the other is allowed to protrude a predetermined length L. The two assemblies of fibre and supporting capillary are then fitted into a larger-bore tube, giving the arrangement depicted in figure 11. The tolerances between the fibre and the supporting tubes, and the supporting tubes and the outer tube are of the order of 3–5 μm, ensuring that the optical fibres are well aligned. The sensor is held together with epoxy resin.

The lowest natural frequency, f_1, of a cantilever beam is given by:

$$f_1 = (C_1/2\pi)(EI/\rho AL^4)^{1/2} \qquad (1)$$

where C_1 is a geometrical factor, E is the Young's modulus, I is the 2nd moment of area, A is the cross-sectional area of the beam and L is its length. For 50/125 multi-mode optical fibres the relationship between unsupported fibre length and natural frequency is shown by figure 12.

The relative sensitivity and frequency response of the device may be tailored by altering its geometry. Its resonant frequency may be tuned to a particular wavelength, over a range of a few thousand Hertz, by varying the length of the cantilever. Sensors employing shorter cantilevers are able to respond to higher frequencies, but will tend to be less sensitive than longer ones, giving a smaller change in intensity for a given amplitude of vibration.

In the first instance, the sensor was used to try to detect changes in a CFRP panel's response to an acoustic transient, following the introduction of impact damage in the panel. The material was a 16-ply cross-ply composite having the lay-up sequence $\{0/90_2/0_2/90/0/90\}_s$.

Sensors were bonded to the surface of 70 × 70 mm^2 specimens with cyanoacrylate adhesive. First, the response of the sensor to the impact of a 6.5 mm diameter steel ball from a height of 25 cm was recorded. The panel was then subjected to an 8 J impact in a falling-weight impact machine fitted with a 20 mm diameter hemispherical tup,

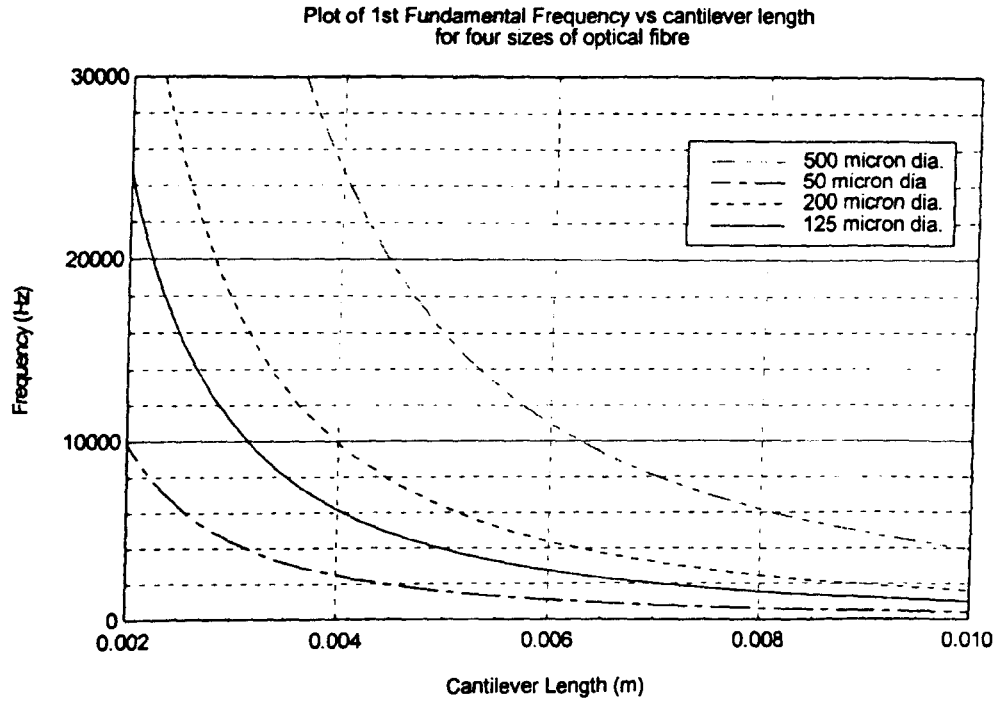

Figure 12. Variation of lowest resonant frequency with cantilever length for four common sizes of silica optical fibre.

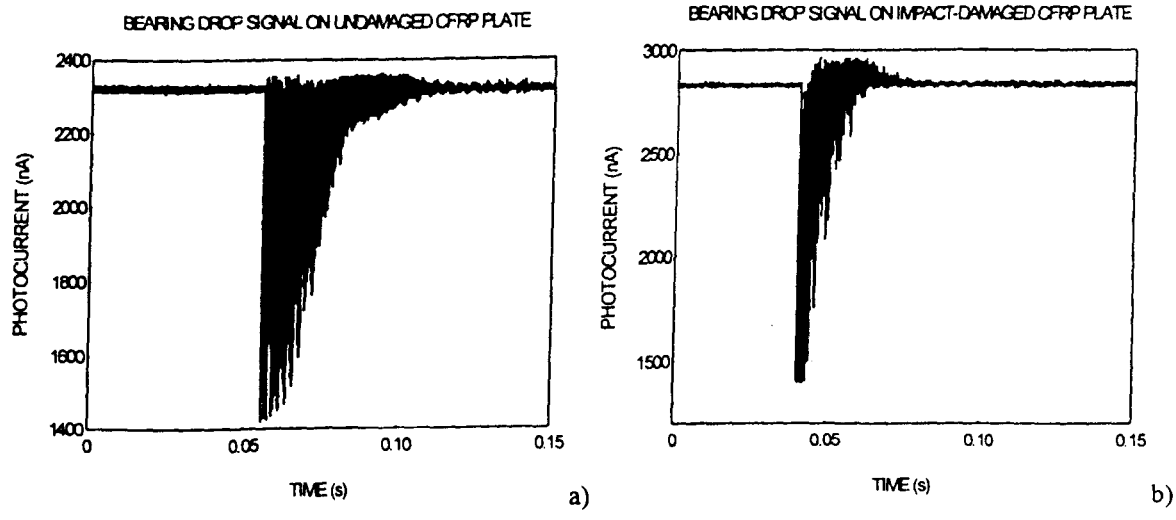

Figure 13. Representative examples of sensor output before (a) and after (b) an 8 J impact on the CFRP plate.

producing delamination and visible cracking on its lower surface. The ball drop tests were repeated and the two sets of results compared.

Figure 13 indicates that the sensor's output changed noticeably after the plate was damaged. The shape of the right-hand trace is different; vibrations were more quickly damped and FFT analysis indicated changes in the resonant frequencies of the panel.

The important information in the sensor's output is contained in the AC component of the signal rather than the DC background. Unavoidable fluctuations in the latter due to losses in the optical train should not, therefore, affect the operation of the sensor unduly, as long as they are of long period relative to the AC signal.

3.3. Impact damage detection based on 'self-sensing' composites

Some of the limitations of the optical-fibre-based crack detection system mentioned above can be overcome if the reinforcing fibres can be made to act as the light guide. The concept of the reinforcing fibre light guide (RFLG) is ideal for impact damage detection and has a number of advantages:

(i) there is minimal induced distortion on the reinforcing fibres when the RFLGs are embedded in the AFRC;

(ii) RFLGs offer the possibility of eliminating resin-rich regions;

(iii) the RFLGs contribute to the reinforcement of the

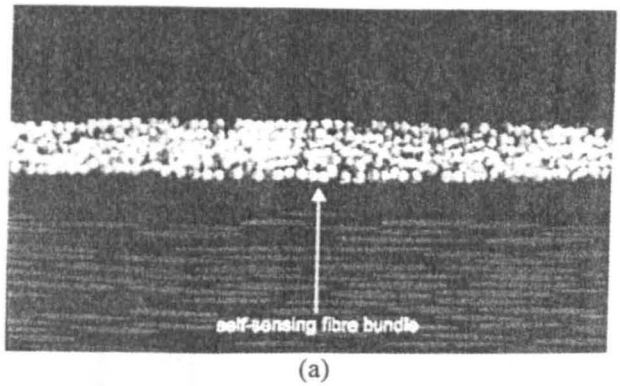

(a)

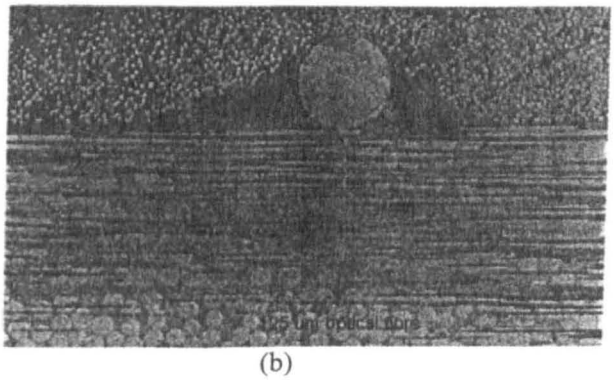

(b)

Figure 14. (a) Micrograph of a self-sensing composite. (b) Micrograph of an embedded 50/125 optical fibre.

composite structure;

(iv) large areas of the composite structure can be covered using the RFLGs. This is a major advantage over conventional optical fibre sensors.

High-purity 'Quartzel' silica-glass fibres (from Quartz et Silice, France) were identified as being suitable for producing the RFLG because of their optical properties. These fibres have a low dielectric constant, offer high heat resistance and a high resistance to thermal shock. As a consequence of this, they are used extensively in the aircraft industry for radomes, electromagnetic windows and thermal insulation applications.

In the current study, a silicone cladding was applied to a Quartzel fibre bundle consisting of approximately 400 individual filaments and cured according to the resin manufacturer's recommended cure schedule. These RFLGs were then placed between the outer two plies of an autoclave-cured 16-layered cross-ply $\{0/90_2/0_2/90/0/90\}_s$ composite fabricated from Ciba–Geigy Fibredux T300/920 prepreg. The fibre bundles were located 10 mm apart. The composite with embedded RFLGs was known as the 'self-sensing' composite. Reference panels without any embedded optical fibres were also made. The cured composite panels were cut into 70 mm squares, C-scanned and then dried in an air circulating oven at 60 °C for three days. The test specimens were stored in a desiccator until required. A micrograph of a polished transverse section through a self-sensing composite is shown in figure 14(a). Figure 14(b) illustrates an embedded, conventional 50/125 optical fibre. The diameter mismatch between the optical fibre and the reinforcing fibre is obvious.

The intensity of light transmitted through each embedded RFLG was measured with an apparatus described in a previous publication [26]. The composite panels were impacted on a Rosand instrumented falling-weight impact testing machine at 2 J, 8 J and 10 J using a 50 mm hemispherical tup. The specimens were C-scanned again and the light transmission intensity through the embedded optical fibres was re-measured after the impact trials.

Figure 15 shows data for a panel, with embedded RFLGs impacted at 2 J. The reduction in transmitted light intensity after the impact indicates that the RFLG is capable of detecting impacts with energies as low as 2 J.

4. Damage detection using an extrinsic Fabry–Pérot interferometric (EFPI) sensor

Fibre Fabry–Pérot (FP) strain sensors can be classified as intrinsic, extrinsic, in-line or Bragg-grating-based cavities. The intrinsic FP sensor design consists of a short length of single-mode fibre whose ends are coated with semi-reflective film and then fusion spliced onto the end of a normal single-mode fibre [27]. This design is relatively compact but suffers from temperature cross-sensitivity and cannot be subjected to tensile strain larger than 4 mε [28]. The extrinsic FP sensors have two single-mode optical fibres, often housed in a capillary tube and are separated by an air gap. The in-line fibre FP sensor design is constructed by fusion splicing a glass capillary tube onto a single-mode fibre of the same outside diameter [29]. The Bragg-grating-based FP sensor is created by using two or more pairs of in-fibre Bragg gratings to form the cavity [28].

4.1. Multi-mode EFPI strain sensor based on a CCD detection system

This section reports on the deployment of a multi-mode EFPI sensor to monitor the structural integrity of carbon-fibre-reinforced epoxy composites (CFRP). A schematic illustration of the multi-mode EFPI sensor design is presented in figure 16(a). The sensor consists of two multi-mode fibres (50/125) which were separated by an air gap and placed into a precision bore silica capillary of 128 μm internal diameter. The fibres were secured in position by fusion splicing them on to the capillary. A resin affixant was also used to secure the optical fibres in the capillary, imparting extra protection to the sensor.

Quasi-static strain measurements are obtained by determining the absolute length of the EFPI cavity. This can be achieved via white light interferometry employing one or two while light sources with a receiving interferometer [30], electronically scanned white light interferometry [31], multiple-wavelength interferometry [32] and channelled spectrum techniques [33].

Since the reflectivity of the glass/air interfaces is very low, the sensor is a low-finesse Fabry–Pérot interferometer, and can be treated as a two-beam interferometer. The interference signal can be described by:

$$I = R(\lambda)P(\lambda)(1 + V\cos(4Bd/\lambda)) \qquad (2)$$

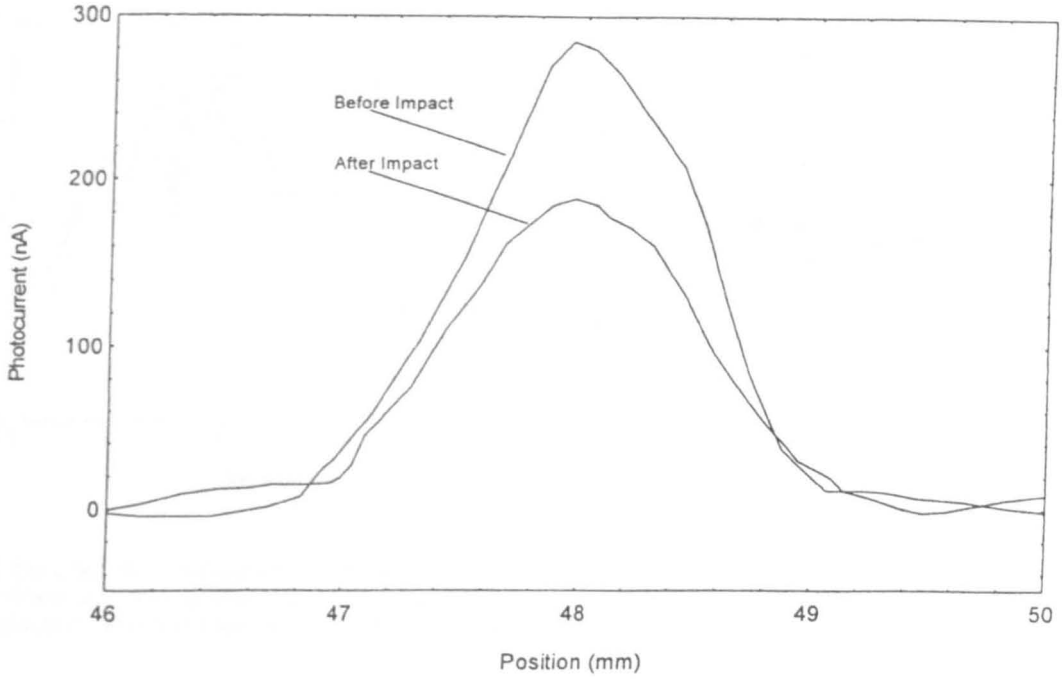

Figure 15. The effect of a 2 J impact on the transmitted light intensity through a RFLG embedded in a CFRP plate.

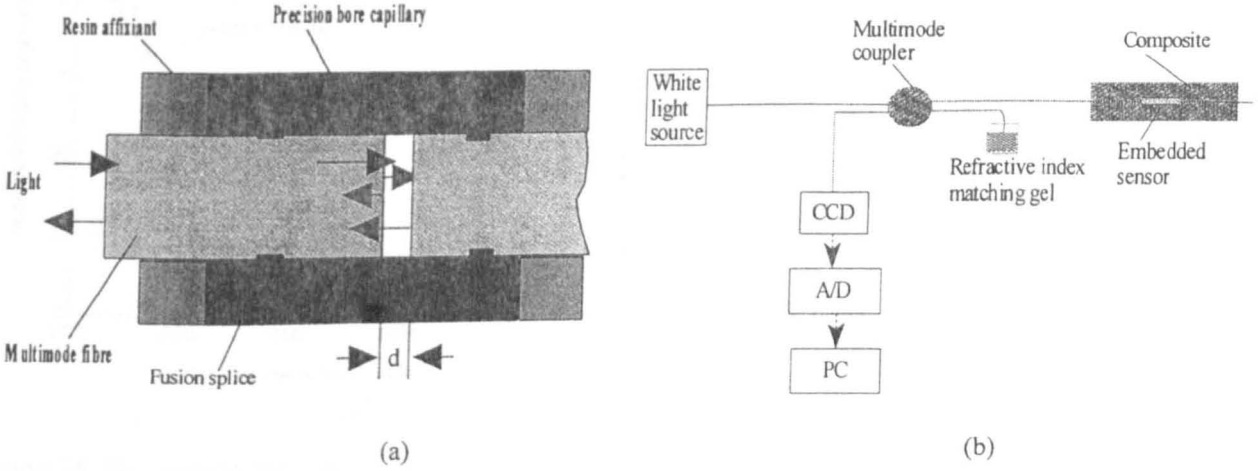

Figure 16. (a) Schematic of the EFPI sensor design; (b) the CCD detection system.

where, λ is the optical wavelength in vacuum, $R(\lambda)$ is the detector responsivity, $P(\lambda)$ is the power density, d is the EFPI cavity length and V is the visibility of the interference fringes. V is a function of the relative intensity of the reflected light at two cleaved fibre end-faces and the cavity length [34].

In this study the signal processing of the interference signal was based on a portable CCD spectrometer (Ocean Optics Limited, Model S1000). A schematic illustration of the experimental set-up is presented in figure 16(b).

Light from a tungsten halogen lamp was launched into a multi-mode coupler to illuminate the EFPI sensor which was embedded in a composite. The reflected light from the sensor was delivered via the multi-mode coupler to a grating element and the refracted light was detected with a CCD array. The output signal from each pixel of the CCD array represents the optical intensity at a specific wavelength. The acquisition time for a spectrum is of the order of 8 ms, which is adequate for the dynamic loading experiments used in this study. The CCD device provided automatic ambient light and dark current compensation, and hence a low noise level. A PC was used for data analysis and for calculating the cavity length and hence the strain as a function of applied load on the composite.

The absolute cavity length can be measured by a fringe counting technique [9] or by measuring the fringe visibility [35]. This section demonstrates the feasibility of strain measurement based on fringe visibility modulation. This approach offers higher signal processing speed when compared with fringe counting.

The signal processing for visibility measurement involved three steps:

(i) Normalizing the reflection spectrum to its mean value, in order to compensate for the intensity drifts due to

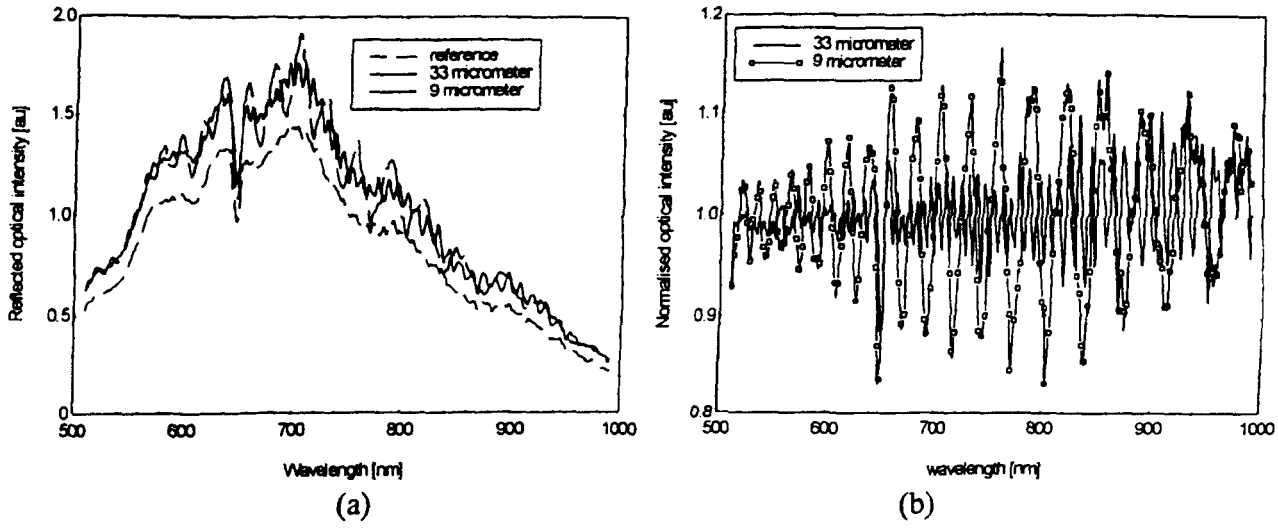

Figure 17. (a) Intensity-compensated spectra obtained from multi-mode EFPI sensors with cavity lengths of 9 and 33 μm, and a smoothed light source spectrum. The reference spectrum is displaced downward slightly for clarity. (b) Normalized reflection spectrum which is intensity and light source spectrum compensated.

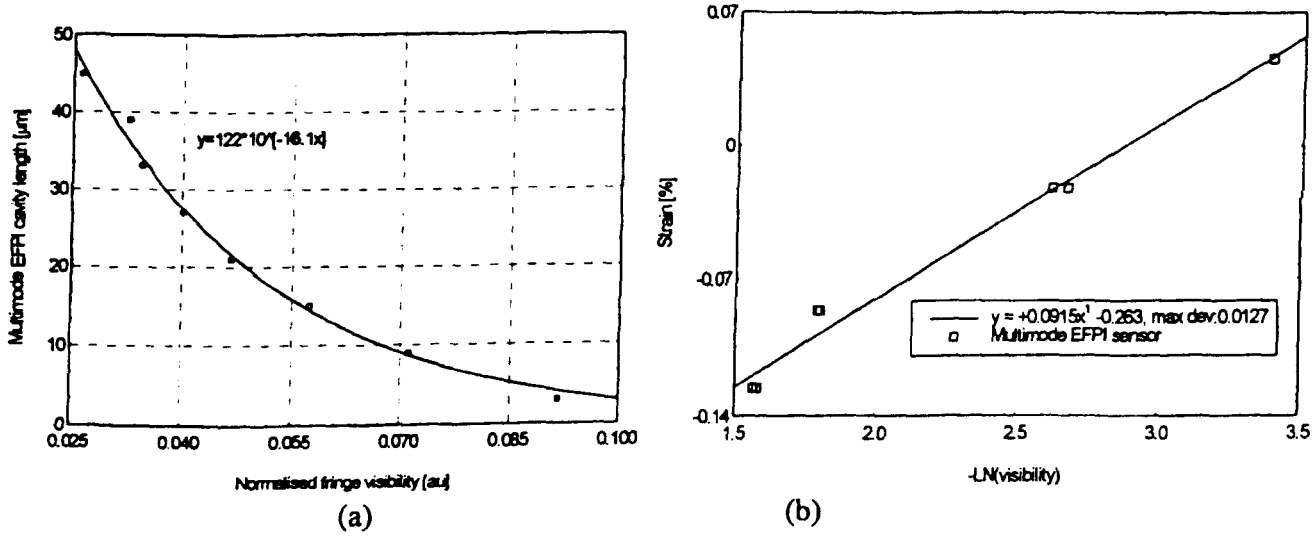

Figure 18. (a) Cavity length versus visibility index obtained using the normalization methods; (b) *in-situ* strain versus [− ln(visibility)] obtained with a multi-mode fibre EFPI sensor.

fibre leads and the light source. Since the effect of bending loss on the optical fibre leads and light source intensity drifts are similar at all the wavelengths, normalizing the spectrum with respect to the average signal level will give aa intensity-dependent spectrum. This approach will overcome the problem of intensity drift normally associated with intensity-based strain measurements. Figure 17(a) shows the intensity-compensated reflection spectra from multi-mode EFPI sensors of two different cavity lengths along with a smoothed light source spectrum which will be used for subsequent referencing purposes.

(ii) Normalizing the spectrum obtained after step 1, with respect to a smoothed light source spectrum. This step removes the effect of the light source spectrum while retaining the features of the interference signal. The normalized spectra are shown in figure 17(b).

(iii) Calculation of the visibility of the normalized interference fringes, and relating to the cavity length and hence strain. Instead of using the conventional definition of fringe visibility, the standard deviation of the normalized reflection spectra shown in figure 17(b) is defined as an index of the fringe visibility. It was found that such an index is an absolute measure of the low-finesse multi-mode EFPI cavity and thus can be used to deduce cavity length and strain. A typical relationship between the cavity length and the visibility index is shown in figure 18(a).

In-situ strain measurement from a sensor embedded in a carbon fibre composite specimen has been made using this principle. The results are shown in figure 18(b). The fabrication of the composite specimen was described elsewhere [34]. The visibility was first transformed using a logarithmic function (− ln(visibility)) to provide a linear function with strain. The fringe visibility was found to be affected by the quality of the cleaves and the alignment of the fibres.

This visibility modulation scheme only involves normalization and simple statistical calculations, thus it is better suited to automation of the signal processing than other interferometric demodulation methods, such as fringe counting.

4.2. Damage detection using in-fibre Bragg grating sensors and a CCD detection system

A variety of methods can be used for interrogating FBG sensors, including interferometric wavelength shift detection [36], Fabry–Pérot wavelength filter detection [37], acousto-optic tuning filter techniques [38], edge filter ratiometric methods [39] and a conventional polychromator. Interferometric methods have the highest resolution and are suitable for high-precision strain measurements. The ratiometric technique offers technical simplicity and fast signal recovery. The cyclic frequencies typically used in the fatigue testing of composites are between 2–10 Hz with a strain range of -1% and $+1\%$. The techniques mentioned above have only been demonstrated for use in the laboratory, further development is needed before they can be used for strain monitoring during fatigue testing. Interrogation of the FBG with a polychromator is not suitable for real-time strain measurements in composites due to the slow scanning speed of the instrumentation. Furthermore, the bulkiness of the instrumentation also makes it unsuitable for on-site applications.

The same fibre-optic-based CCD spectrometer as described in the previous section was employed in this study. This instrument operates in the spectral range 500–1000 nm with a resolution of 0.42 nm per pixel and response time of 8 ms per spectrum. Since the Bragg grating wavelength shift with strain is fairly small, it was necessary to improve the spectral resolution. The FBG sensor reflective spectrum was clearly defined and the application of a spline fitting routine to the spectrum is justified. This curve fitting procedure enabled the spectral resolution to be improved to better than 0.05 nm, corresponding to a strain sensitivity of approximately 80 $\mu\varepsilon$. This fulfils the requirement of the fatigue test programme undertaken in this study. This CCD-based approach offers access to the whole FBG reflection spectrum rather than just using the peak reflection wavelength.

The principle of operation of the fibre Bragg grating has been described extensively [40]. The FBG sensors were made from a standard single-mode fibre which was sensitized by exposing it to a high-pressure hydrogen atmosphere. The nominal Bragg grating wavelength was 827 nm with a bandwidth of 0.2 nm and a reflectivity of 90%.

A schematic illustration of the experimental set-up which was used for the calibration of the CCD spectrometer and the characterization of the SLD light source is shown in figure 19. A laser light and a broad-band super-luminescent diode (SLD) were used to illuminate the single-mode couplers. The reflected light from the coupler was detected using the CCD spectrometer. The ends of fibre (A) from coupler number 1 and the Bragg grating were

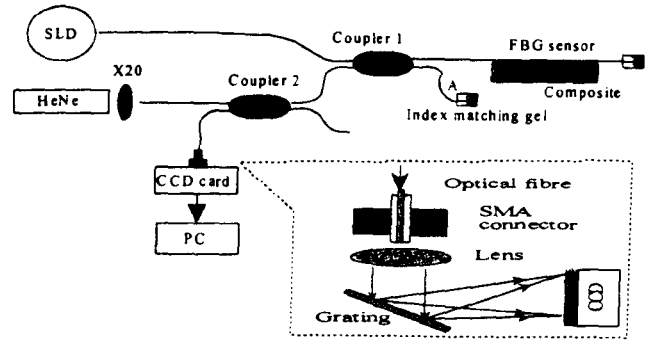

Figure 19. Schematic of the experimental set-up for the FBG strain measurement experiments.

immersed in an index matching gel to eliminate reflected light from the end-faces. The nominal central wavelength of the SLD was 840 nm with a bandwidth of approximately 10 nm. The output power coupled into the single-mode fibre was approximately 100 μW. The accuracy of the fibre-optic CCD spectrometer was found to be dependent on the position of the fibre tip which was housed in the SMA connector, as shown in the insert in figure 19. It was found from the reflection spectrum that the position of the fibre end within the SMA connector can introduce a wavelength offset up to ± 3 nm. However, once the instrument is calibrated this offset can be corrected and does not affect the strain measurement.

The fibre Bragg grating sensor was bonded to the surface of a CFRP specimen. Prior to this, the bonding-area was first lightly abraded and degreased using conventional procedures. Static tensile tests were carried out on an Instron 4206 testing machine. The computed relationship between applied strain and the Bragg reflection is 0.65 nm per milli-strain. This correlates with the results obtained using the extensometer for both tensile and compressive loading as seen in figure 20(a). The strain range for these experiments was restricted to between -0.2% and 0.3%. The influence of temperature was not considered in this study because the tests were made at a constant ambient temperature of 23 °C.

Figure 20(b) demonstrates the stiffness reduction in the composite as a function of fatigue cycling. These tests were carried out on an Instron 8501 servo-hydraulic dynamic testing machine at loading frequencies from 0.1 Hz to a maximum of 6 Hz at a stress ratio of -0.5. Both the extensometer and the FBG sensors showed a similar trend of stiffness reduction but the stiffness obtained from the FBG was higher than that from the surface-mounted extensometer. This discrepancy between extensometer and FBG data may be attributed to debonding of the FBG from the composite.

5. Conclusions

On-line process monitoring of composites: we have successfully deployed (a) two refractive-index-based optical fibre sensors; (ii) an evanescent wave spectroscopy optical fibre sensor and (iii) an optical-fibre-based transmission infrared spectroscopy sensor to monitor the cure kinetics of

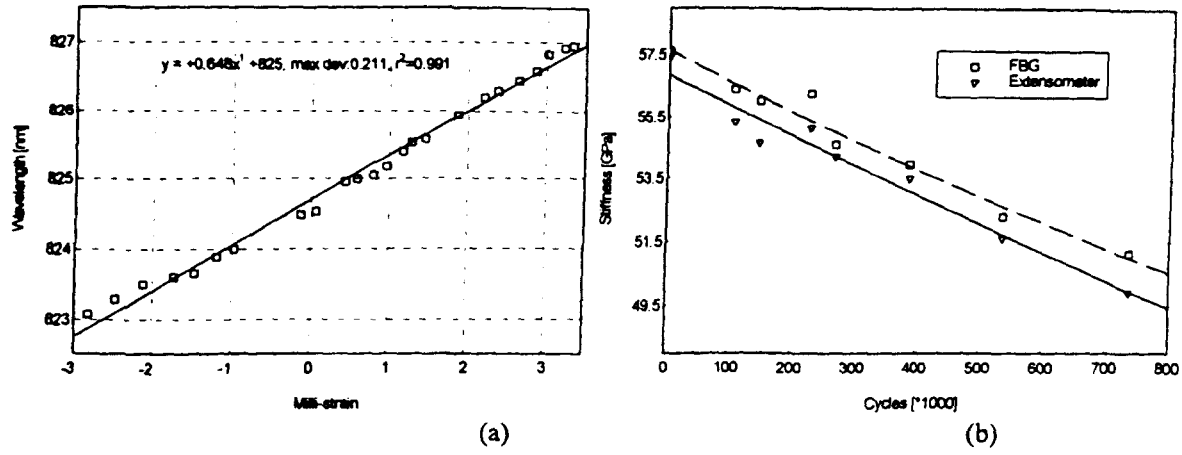

Figure 20. (a) Optical wavelength versus milli-strain for the surface-mounted FBG sensor; (b) stiffness-decay data using a surface-mounted extensometer and a FBG sensor. The composite was under fatigue testing using a peak stress of 210 MPa, a frequency of 6 Hz and a stress ratio of −0.5.

epoxy-based resin systems in real-time. A discrepancy was found in the cure characteristics of hexanediamine/Epikote 828 resin using the various cure monitoring techniques. It is proposed that the observed discrepancy could be due to: (a) specific interaction between the resin system and the optical glass fibre surface; (b) lack of accurate data on the relationship between the extent of crosslinking, development of morphology in the resin and the associated change in the refractive index and (c) the sensitivity of the evanescent sensor to localized variations in the cure chemistry and/or temperature.

The concept of using reinforcing fibres as light guides was proven. The RFLG was shown to be capable of detecting 2 J impacts. This technique offers the potential for large-area coverage of impact damage detection in engineering structures.

A simple design of fibre-optic vibration sensor has been shown to be sufficiently sensitive to indicate impact damage in CFRP. It has the possibility to operate satisfactorily without requiring a referencing system, is completely enclosed, and well suited to embedment within a structure or skin.

Fatigue tests on carbon-fibre-reinforced composites with Fabry–Pérot and Bragg grating sensors demonstrated that OFS can be used for both tensile and compressive strain under quasi-static and dynamic loading conditions. A demodulation technique for an existing multi-mode interferometric strain sensor is proposed.

Acknowledgments

The authors thank the EPSRC and DRA for CASE studentships for D Brooks, C Doyle, S Hayes and A Martin, and the award of a ROPA grant to T Liu. G Fernando acknowledges the receipt of a Royal Society equipment grant for the development of the sensor. The authors would like to thank Professors P Curtis, B Ralph and Drs S Hitchen, M Kemp, D Pullen and R Badcock, J Coleman and J Curtis and A Howard of the DRA, Mr Bill Ridoutt of Cape Durasteel and J Harry of Quartz et Silice for supporting the research programme. The assistance given by Professor J Stonham and Dr K Hale is duly acknowledged. The authors also wish to thank Professor D Jackson and Y J Rao (University of Kent) and L Zhang and Professor I Bennion (Aston University) for supplying and assisting with the Bragg gratings.

References

[1] O'Brien T K and Reifsnider K L 1981 Fatigue damage evaluation through stiffness measurements in boron-epoxy laminates *J. Composite Mater.* **15** 55–70

[2] Jamison R D, Reifsnider K L, Schulte K and Stinchcombe W W 1984 *ASTM STP* **836** 36

[3] Kaczmarek H 1995 Ultrasonic detection of damage in CFRP's *J. Composite Mater.* **29**

[4] Vikstroem M, Buckland J and Olsson K 1989 Non-destructive testing of sandwich construction using thermography *Composite Struct.* **13**

[5] Salleh R, Day R and Taylor R 1995 Correlation between the acoustic emission and damage modes during splitting of carbon fibre reinforced poly-ether-ether-ketone composite *J. Mater. Sci. Lett.* **14** 390

[6] Wang X and Chang D D 1996 Self-monitoring carbon-fibre polymer matrix composites *SPIE Int. Soc. Opt. Eng.* **2716** 259–66

[7] Measures R M 1991 The detection of damage and the measurement of strain within composites by means of embedded optical fibre sensors *Rev. Prog. Quantitative Non-Destructive Evaluation* B **10** 1247–57

[8] Hogg H, Mason B, Valis T and Measures R M 1992 Development of a fibre Fabry–Pérot (FFP) strain gauge system *Active Materials and Adaptive Structures* ed G J Knowles (Bristol: Institute of Physics) pp 667–72

[9] Claus R O, Gunther M S, Wang A B, Murphy K A and Sun D 1993 Extrinsic Fabry–Pérot sensors for structural evaluation *Applications of Fibre Optic Sensors in Engineering Mechanics* ed F Ansari pp 60–70

[10] Badcock R and Fernando G F 1995 An intensity based optical fibre sensor for fatigue damage detection in advanced fibre-reinforced composites *Smart Mater. Struct.* 4 223–30

[11] Jones B D and Spooncer R A 1983 Photoelastic pressure sensor with optical fibre links using wavelength characterisation *Proc. 1st Int. Conf. on Optical Fibre Sensors (London)* p 173

[12] Hill K O 1996 Fibre Bragg gratings: properties and sensing applications *Conf. Proc. OFS-11 (Hokkaido, 1996)* pp 92–4

[13] Simonsen H D and Paetsch R 1992 Fibre Bragg grating sensor demonstration in a glass-fibre reinforced polyester composite *1st Eur. Conf. on Smart Structures and Materials (Glasgow)* pp 73–6

[14] Rao Y J, Lobo Ribeiro A B, Jackson D A, Zhang L and Bennion I 1995 Combined spatial- and time-division-multiplexing scheme for fibre grating sensors with drift-compensated phase-sensitive detection *Opt. Lett.* **20** 2149–51

[15] Hale K F, Hockenhull B S and Christodolou G 1980 The application of optical fibres as witness devices for the detection of plastic strain and cracking *Strain* October 150

[16] Udd E 1992 *Fiber Integrated Opt.* **11** 319–36

[17] Tanwar L S, Gupta B S and Bansal S C 1994 *Opt. Eng.* **33** 1950

[18] Nokes M A, Hill B C and Barelli A E 1978 *Rev. Sci. Instrum.* **46** 722–8

[19] Liang D and Culshaw B 1993 *Electron. Lett.* **29** 529

[20] Conforti G, Brenci M, Mencaglia A and Mignani A 1989 Fiber optic vibration sensor for remote monitoring in high-power electric machines *Appl. Opt.* **28** 5158

[21] Fuhr P L 1983 Simultaneous single-fiber active vibration sensing and impact detection for large space structures *SPIE* **1918** 145

[22] Gerges A S, Newson T P and Jackson D A 1989 *Opt. Lett.* **14** 1155

[23] Kersey A D, Jackson D A and Corke M 1983 *Opt. Commun.* **45** 71–4

[24] Martinelli M 1982 *IEEE J. Quantum Electron.* **QE-18** 666

[25] Murphy K A, Fogg B R and Vengsarkar A M 1992 Spatially weighted vibration sensors using tapered two-mode optical fibres *J. Lightwave Tech.* **10** 1680–7

[26] Hayes S, Brooks D, Liu T, Vickers S and Fernando G F 1996 In-situ self-sensing fibre reinforced composites *Smart Materials and Structures (San Diego, CA, 1996)*

[27] MacPherson W N, Kidd S R, Barton J S and Jones J D C 1996 Phase demodulation in optical fibre Fabry–Pérot sensors with inexact phase steps *Proc. Appl. Opt. Divisional Conf. Inst. Phys. (Reading)* ed K T V Grattan pp 110–5

[28] Kaddu S C, Booth D J, Garchev D D and Collins S F 1996 A multiple-wavelength fibre Fabry–Pérot sensor using a single source and co-located Bragg gratings *Proc. Appl. Opt. Divisional Conf. Inst. Phys. (Reading)* ed K T V Grattan Post dead-line papers

[29] Sirkis J S, Brennan D D, Putman M A, Berkoff T A, Kersey A D and Friebele E J 1993 In-line fibre etalon for strain measurement *Opt. Lett.* **18** 1973–5

[30] Rao Y J and Jackson D A 1996 Recent progress in fibre optic low-coherence interferometry *Meas. Sci. Technol.* **7** 981–99

[31] Marshall R H, Ning Y N, Palmer A W and Grattan K T V 1996 A novel implementation of a bulk optical Mach–Zehnder interferometer for enhanced stability in a fibre-optic electronically scanned white light interferometric system *Conf. Proc. OFS-11 (Japan)* pp 336–9

[32] Ezbiri A and Tatam R P 1996 A fibre Fabry–Pérot temperature sensor using multiple wavelength interrogation *Conf. Proc. OFS-11 (Japan)* p 192–5

[33] Taplin S R, Podoleanu A G, Webb D J and Jackson D A 1995 White light interferometer using linear CCD array with signal processing *Trends in Optical Fibre Metrology and Standards* ed D D Soares (Dordrecht: Kluwer) pp 831–2

[34] Liu T, Brooks D, Martin A, Badcock R and Fernando G F 1996 Design, fabrication and evaluation of an optical fibre strain sensor for tensile and compressive strain measurements via the use of white light interferometry *Smart Mater. Struct. (San Diego, CA, 1996)*

[35] Doyle C, Martin A, Wu M, Badcock R A, Khan N, Liu T, Hayes S, Brooks D and Fernando G F 1996 Intensity based optical fibre sensors for condition monitoring of engineering materials *Conf. Proc. Photonics (Beijing, 1996)*

[36] Kersey A D, Berkoff T A and Morey W W 1992 High resolution fibre-grating based strain sensor with interferometric wavelength-shift detection *Electron. Lett.* **28** 236–8

[37] Kersey A D, Berkoff T A and Morey W W 1993 Multiplexed fibre Bragg grating strain sensor system with a fibre Fabry–Pérot wavelength filter *Opt. Lett.* **18** 1370–2

[38] Xu M G, Geiger H, Archambault J L, Reekie L and Dakin J P 1993 Novel interrogation system for fibre Bragg grating sensors using an acousto-optic tunable filter *Electron. Lett.* **29** 1510–1

[39] Measures R M, Melle S and Liu K 1992 Wavelength demodulation Bragg grating fibre optic sensing systems for addressing smart structure critical issues *Smart Mater. Struct.* **1** 36–44

[40] Morey W W, Meltz G and Glenn W H 1989 Fibre optic Bragg grating sensors *SPIE Fiber Optic and Laser Sensors VII* **1169** 98–107